

Water dynamics in cement paste: insights from lattice Boltzmann modelling

THÈSE N° 6292 (2014)

PRÉSENTÉE LE 24 JUILLET 2014

À LA FACULTÉ DES SCIENCES ET TECHNIQUES DE L'INGÉNIEUR
LABORATOIRE DES MATÉRIAUX DE CONSTRUCTION
PROGRAMME DOCTORAL EN SCIENCE ET GÉNIE DES MATÉRIAUX

ÉCOLE POLYTECHNIQUE FÉDÉRALE DE LAUSANNE

POUR L'OBTENTION DU GRADE DE DOCTEUR ÈS SCIENCES

PAR

Mohamad ZALZALE

acceptée sur proposition du jury:

Prof. H. Hofmann, président du jury
Prof. K. Scrivener, Prof. P. J. McDonald, directeurs de thèse
Prof. S. Churakov, rapporteur
Prof. C. Hall, rapporteur
Prof. H. Stang, rapporteur



ÉCOLE POLYTECHNIQUE
FÉDÉRALE DE LAUSANNE

Suisse
2014

All that I am, or hope to be,
I owe to my angel mother.
— Abraham Lincoln

Per ardua ad astra ...

إِلَى أُمِّي وَأَبِي

Acknowledgements

First and foremost, I would like to thank Marie* for the generous funding without which this thesis, but more importantly many splendid memories, would not exist. I would also like to express my deepest gratitude to Karen and Peter for their support and guidance. The results of this thesis are mostly due to their flexibility towards my ideas which would not have blossomed without their multi-disciplinary vision.

I am indebted to all the LMC staff who guaranteed THE perfect ~~play~~ work atmosphere. LMC would not be LMC without the numerous apéros, BBQs, Leysin seminars and lab hikes so thanks for all who organized (and allowed organizing) these events. I was lucky to be in the best office at EPFL so I must thank Berta and Julien for making it such an animated and lively place. Also, running during work times was strangely satisfying (still not 100% clear if the satisfaction comes from running or simply from stopping work) so huge thanks for Anne-Sandra, Maude and Lionel.

Visiting European cities and mountains was an integral part of my stay in Switzerland. Thanks for Elise, Pawel and Julien for the city breaks. Thanks for all those who *invested* their time in teaching me how to ski and for those who *dragged* me to the summits of few of the most beautiful and picturesque mountains on Earth.

Writing down all the names and acknowledgements on one single page *is* the hardest task of an EPFL thesis. I just would like to finish by thanking all my friends and colleagues for making my Ph.D. a pleasurable experience. *If all the labs lead to a doctorate, then it is how you get there that matters...*

Lausanne, June 27th 2014

Mohamad Zalzale

*This project is part of a Marie Curie ITN funded by the European Union Seventh Framework Programme (FP7 / 2007–2013) under grant agreement n°264448.

Abstract

Transport properties are often used as indicators of durability because water underpins most of the degradation mechanisms of concrete structures. The objective of this thesis is to understand the link between the microstructure and the permeability of cement paste, the binder phase of concrete. To achieve this goal, the lattice Boltzmann method is used to simulate the flow through three-dimensional model cement paste microstructures generated with the hydration modelling platform μic .

First, it is confirmed that standard lattice Boltzmann (LB) models fail to predict the permeability and the water isotherms of cement paste. This is because the calcium silicate hydrate (C-S-H) has a complex and uncertain structure and is usually, out of computational necessity, treated as an impermeable solid. The LB model is consequently extended with an effective media approach to incorporate the flow through the nano-porous C-S-H.

Accordingly, to calculate the permeability of cement paste, the C-S-H is assigned an intrinsic permeability. It is found that when the capillary porosity is completely saturated with a fluid (either water or gas), the calculated intrinsic permeability is in good agreement with measurements of gas permeability on dried samples ($10^{-17} - 10^{-16} \text{ m}^2$). However, as the water saturation is reduced, the calculated apparent water permeability decreases and spans the full range of experimentally measured values ($10^{-16} - 10^{-22} \text{ m}^2$). Thus, the degree of saturation of the capillary porosity is likely the major cause for variation in the measurements of the permeability of cement paste. Further, it is found that the role of the weakly-permeable C-S-H, omitted in earlier modelling studies, has a non-linear effect on the permeability of cement paste and is critical at a low capillary porosity and / or low capillary saturation.

Finally, to calculate the water isotherms of cement paste, the LB model is extended from isothermal to non-ideal fluids as described by an equation of state. Using a novel method, the C-S-H is assigned an intrinsic permeability and effective wetting properties. It is found that, in agreement with experiments, the calculated water isotherms show two main steps, the first corresponding to the capillary pores and the second to the smaller gel pores.

Key words: Cement paste; Modelling; Transport properties; Permeability; Desorption; Isotherms; Lattice Boltzmann; Effective media; Calcium silicate hydrate; Model microstructures; Porous media;

Résumé

Les propriétés de transport sont souvent utilisées comme indicateurs de la durabilité des structures en béton car l'eau joue un rôle essentiel dans la plupart des mécanismes de dégradation du béton. L'objectif de cette thèse est une meilleure compréhension du lien entre la microstructure et la perméabilité de la pâte de ciment, phase liante du béton. A cette fin, la méthode *lattice Boltzmann* est utilisée pour simuler l'écoulement dans des microstructures tridimensionnelles de pâtes de ciment générées avec la plateforme d'hydratation μic .

Les modèles standards de lattice Boltzmann (LB) ne reproduisent pas correctement la perméabilité ni les isothermes d'adsorption et de désorption d'eau de la pâte de ciment. En effet, la complexité et la variabilité de la structure du silicate de calcium hydraté (C-S-H) est souvent simplifiée en un solide imperméable pour le calcul. Pour palier ces limitations, un nouveau modèle LB basé sur des propriétés homogènes a été développé qui inclut le transport à travers les nano-pores du C-S-H.

Dans ce modèle, une perméabilité intrinsèque a été attribuée au C-S-H pour calculer celle de la pâte de ciment. Les simulations montrent que lorsque la porosité capillaire est complètement saturée par un fluide (eau ou gaz), la perméabilité intrinsèque calculée est en bon accord avec les mesures expérimentales de perméabilité aux gaz effectuées sur échantillons secs ($10^{-17} - 10^{-16} \text{ m}^2$). Cependant, en réduisant la saturation en eau, la perméabilité à l'eau apparente diminue et couvre la même gamme que les valeurs mesurées expérimentalement ($10^{-16} - 10^{-22} \text{ m}^2$). Ainsi, les résultats des simulations suggèrent que le degré de saturation capillaire est la principale cause de variation dans les mesures expérimentales. En outre, le flux à travers C-S-H, omis dans les études antérieures, a un effet non linéaire sur la perméabilité. Ce flux est indispensable pour calculer la perméabilité à faible porosité ou saturation capillaire.

Finalement, pour calculer les isothermes d'eau de la pâte de ciment, le modèle LB a été modifié pour inclure des fluides non-idéaux décrits par une équation d'état. Dans cette nouvelle méthode, le C-S-H est caractérisé par des propriétés intrinsèques de mouillage et de perméabilité. Les isothermes d'eau simulés présentent deux régimes principaux: le premier correspond aux pores capillaires et le second aux pores du C-S-H, en accord avec les expériences.

Mots clés: Pâte de ciment; Modélisation; Propriétés de transport; Perméabilité; Désorption; Isothermes; Lattice Boltzmann; Propriétés homogènes; Silicate de calcium hydraté; Microstructures modèles; Milieux poreux;

Contents

Abstracts	vii
Abstract	vii
Résumé	ix
Contents	xiii
List of Figures	xvii
List of Tables	xix
Nomenclature	xxi
1 Introduction	1
1.1 Concrete	1
1.2 From concrete to cement paste	1
1.3 Indicators of durability	3
1.4 Statement of the problem	4
2 Permeability of Cement Paste: State-of-the-art	7
2.1 Darcy's law	7
2.2 Experimental techniques	8
2.3 Modelling techniques	10
2.3.1 Empirical models	10
2.3.2 Numerical models	11
2.4 Experiments and models: a mismatch ?	15
3 Lattice Boltzmann Methods for Isothermal Fluids	17
3.1 Standard methods	17
3.1.1 Overview	17
3.1.2 Collision operators and equilibrium functions	20
3.1.3 Boundary conditions	21
3.1.4 Definition of a lattice Boltzmann algorithm	23
3.1.5 Implementation	23
3.1.6 Methods for calculating permeability	24
3.1.7 Validation	24
	xi

Contents

3.2	Effective media methods for the transport properties	27
3.2.1	Overview	27
3.2.2	Theory	29
3.2.3	Implementation	31
3.2.4	Methods for calculating permeability	32
3.2.5	Validation	32
4	Lattice Boltzmann Methods for non-Ideal Fluids	43
4.1	Standard methods	43
4.1.1	Overview	43
4.1.2	Free energy approach for non-ideal fluids	44
4.1.3	Wetting dynamics	46
4.1.4	Implementation	47
4.1.5	Methods for modelling adsorption and desorption	48
4.1.6	Validation	48
4.2	Effective media methods for the transport and wetting properties	60
4.2.1	Overview	60
4.2.2	Free energy approach for effective wetting properties	60
4.2.3	Implementation	61
4.2.4	Methods for modelling adsorption and desorption	61
4.2.5	Validation	61
4.2.6	Application to a 2D characteristic microstructure	65
4.2.7	Conclusions	69
5	Permeability of Cement Paste	71
5.1	Saturated permeability of cement paste	71
5.1.1	Cement paste model microstructures	71
5.1.2	Reproducibility of the permeability	72
5.1.3	Permeability of cement paste model microstructures	73
5.1.4	Lattice magnification and microstructural resolution	75
5.1.5	Diagonal leaks	77
5.1.6	Comparison of μ_{ic} and CEMHYD3D	78
5.1.7	Comparison of μ_{ic} and HYMOSTRUC3D	78
5.1.8	Conclusions	79
5.2	Unsaturated permeability of cement paste	80
5.2.1	Cement paste model microstructures	80
5.2.2	Model microstructures at reduced degrees of water saturation	81
5.2.3	Permeating fluid: accessible pore network and permeability of the C-S-H	82
5.2.4	Apparent permeability of cement paste model microstructures	83
5.2.5	Discussion	85
5.2.6	Conclusions	86

6	Water Isotherms of Cement Paste	89
6.1	Water isotherms of cement paste	89
6.2	Model water isotherms of the capillary pores	90
6.2.1	Previous work	90
6.2.2	Reproduction of previous work	91
6.3	Model water isotherms of the capillary and C-S-H gel pores	93
6.4	Discussion: Kelvin's equation, a critical limitation in the model isotherms . . .	98
6.5	Conclusions	99
7	Conclusions	101
7.1	Main findings	101
7.2	Outlook	102
7.2.1	Water isotherms of cement paste	103
7.2.2	Experimental validation	103
7.2.3	Microstructural resolution	104
7.2.4	Downscaling	104
7.2.5	Upscaling	104
A	MRT Collision Operator	107
B	Pressure Boundary Conditions	111
C	Effective permeability	113
D	Mathematical Operators	115
	Bibliography	127
	List of Publications	129
	Curriculum Vitae	131

List of Figures

1.1	Back-scattered and transmission electron microscopies of cement paste	2
1.2	Volume composition of cement paste.	3
1.3	Dimensional range of pores in hydrated cement paste.	3
2.1	Schematic illustration of Darcy's law.	8
2.2	Pore size distribution as obtained with MIP.	12
2.3	Model microstructures of cement paste.	12
2.4	Elements in μic with examples of customizable properties and plugins	13
3.1	Illustration of the streaming step in lattice Boltzmann methods	18
3.2	$D3Q19$ vector base	19
3.3	Permeability of a 3D square pipe	25
3.4	Illustration of an array of overlapping spheres	25
3.5	Permeability of an array of overlapping spheres with 20% porosity.	26
3.6	Permeability of an array of overlapping spheres of size $L^3 = 21^3$	26
3.7	Effect of the viscosity on the permeability	27
3.8	Illustration of the effective media model	29
3.9	Illustration of the setup used for setting the pressure boundary conditions	32
3.10	Permeability of a 3D square pipe	33
3.11	Permeability of a 3D square pipe: comparison of two algorithms.	34
3.12	Permeability of an array of overlapping spheres with 20% porosity.	34
3.13	Permeability of an array of overlapping spheres: comparison of two algorithms.	35
3.14	Permeability of homogeneous media	35
3.15	Permeability of homogeneous media: comparison with literature	36
3.16	Pressure drop across homogeneous media	36
3.17	Permeability of an array of permeable spheres	37
3.18	Clips of the velocity in an array of permeable spheres	38
3.19	Illustration of parallel and series layered media	39
3.20	Illustration of a heterogenous medium	40
3.21	Pressure drop in a heterogeneous medium	40
3.22	Illustration of the simulation setup test case 3	41
3.23	Velocity profile for test case 3 as reported in literature	41
3.24	Velocity profile for test case 3 as calculated in this work	42

List of Figures

4.1	Schematic illustration of the phase diagram $P - V$ of a van der Waals fluid. . . .	45
4.2	Contact angle Θ <i>vs.</i> the surface-normal fluid density gradient.	48
4.3	Pressure drop across the liquid – vapour interface of a droplet	49
4.4	Capillary rise <i>vs.</i> the square root of time.	49
4.5	Pendular rings formed between packed spheres.	50
4.6	Effect of the simulation temperature on the fluid distribution	50
4.7	Fluid distribution for a liquid droplet in vapour	52
4.8	Pressure drop across the liquid – vapour interface of a droplet.	52
4.9	Pressure drop across the liquid – vapour interface of a droplet: effect of the interface width.	53
4.10	Spinodal decomposition	53
4.11	Solid-bound spinodal decomposition	54
4.12	Equilibrium contact angles on solid surfaces	55
4.13	Illustration of a convex pore	56
4.14	Kelvin's equation	56
4.15	Illustration of three serially connected pores	57
4.16	Inkbottle effect: equilibrium fluid distribution during desorption	57
4.17	Inkbottle effect: non-equilibrium fluid distribution during desorption	58
4.18	Inkbottle effect: equilibrium fluid distribution during adsorption	59
4.19	Inkbottle effect: non-equilibrium fluid distribution during adsorption	59
4.20	Grey-bound spinodal decomposition	62
4.21	Equilibrium contact angles on grey surfaces	64
4.22	Isotherms of grey nodes: effect of internal wetting	64
4.23	Isotherms of grey nodes: effect of permeability and size	65
4.24	Pseudo-random systems	66
4.25	Pseudo-random systems: water isotherms	66
4.26	Pseudo-random systems: water isotherms	67
4.27	Pseudo-random systems: water isotherms	67
4.28	Pseudo-random systems: equilibrium fluid distribution during desorption and adsorption	68
4.29	Pseudo-random systems: equilibrium fluid distribution during desorption and adsorption	68
5.1	Model cement paste microstructure generated with μic	73
5.2	Solid and pore volumes in a μic model cement paste	73
5.3	Calculated permeability <i>vs.</i> the degree of hydration for different water-to-cement ratios.	74
5.4	Calculated permeability <i>vs.</i> the porosity for different water-to-cement ratios.	74
5.5	Illustration of lattice magnification	75
5.6	Illustration of microstructural resolution	76
5.7	Illustration of diagonal leaks	77
5.8	Model cement paste microstructures generated with μic and CEMHYD3D. . . .	79

5.9	Partially-saturated model cement paste microstructures	82
5.10	Permeability <i>vs.</i> degree of capillary water saturation	83
5.11	Permeability <i>vs.</i> degree of capillary water saturation: effect of the C-S-H	84
6.1	Experimental water isotherms of cement paste.	90
6.2	Model water isotherm of a μic model cement paste.	91
6.3	Model water isotherm of a μic model cement paste: comparison of two methods	92
6.4	Model water isotherm of a μic model cement paste: effect of χ	92
6.5	Model cement paste microstructure generated with μic	93
6.6	Model water isotherms of the capillary and gel pores of cement paste.	94
6.7	Model water isotherms of the capillary and gel pores of cement paste.	94
6.8	Effect of the internal wetting potential of the C-S-H on the model isotherms of cement paste.	95
6.9	Equilibrium fluid distribution during desorption in a μic microstructure	96
6.10	Equilibrium fluid distribution during adsorption in a μic microstructure	97

List of Tables

2.1	Experimental measurements of permeability	9
3.1	Relative error in permeability for structures built from layers of different effective media parameter.	39
4.1	Simulated equilibrium contact angles between liquid and solid.	55
4.2	Simulated equilibrium contact angles between liquid and grey nodes.	63
5.1	Densities of the reactants and hydrates used for the simulation of the cement paste model microstructures.	72
5.2	Effect of the lattice magnification and microstructural resolution on the permeability	77
5.3	Permeability to water and gas of the different cement paste phases.	82
6.1	Effect of the simulation temperature on the emptying RH of a pore	98

Nomenclature

Abbreviation

Permeability	Intrinsic permeability
w/c	Water-to-cement ratio by mass
RH	Relative humidity
NMR	Nuclear magnetic resonance
C-S-H	Calcium silicate hydrate
MIP	Mercury intrusion porosimetry
ITZ	Interfacial transition zone
REV	Representative elementary volume
RHS	Right-hand-side
LHS	Left-hand-side
N.A.	Not applicable
CFD	Computational fluid dynamics
LB	Lattice Boltzmann
BGK	Bhatnagar-Gross-Krook
SRT	Single-relaxation-time
TRT	Two-relaxation-time
MRT	Multi-relaxation-time
Lattice magnification	See figure 5.5
Microstructural resolution	Minimum feature size, see figure 5.6

Description

Symbol

A	Cross section of a sample of length L_0
L_0	Length of a sample of cross section A
L	Side length of a cubic sample
(L_x, L_y, L_z)	Dimensions of a sample
$\mathbf{r} = (l_x, l_y, l_z)$	Coordinates of a lattice node
h	Width and height of an infinitely long sample
r	Radius of a sphere or circle
Q	Number of directions in the lattice Boltzmann method
\mathbf{e}_i	Velocity vectors
w_i	Lattice weights

Description

Nomenclature

Δx	Lattice spacing
Δt	Time step
$\Delta \rho$	Density unit
c	Speed unit ($\Delta x / \Delta t$)
c_s	Speed of sound
f_i	Distribution functions
f_i^{eq}	Equilibrium distribution functions
\mathbf{F}	External force
\mathbf{g}	Body-force
\mathbf{S}	Diagonal relaxation matrix
s_i	Relaxation times of the diagonal relaxation matrix \mathbf{S}
τ	Main relaxation time
\mathbf{M}	Transformation matrix
\mathbf{m}	Hydraulic moments
ρ	Macroscopic density
ρ^*	Microscopic density
ρ_0	Average density in the system
\mathbf{u}	Macroscopic velocity
\mathbf{u}^*	Microscopic velocity
\mathbf{j}	Macroscopic moment
δ_{ij}	Kronecker delta
N_y^x, N_z^x	Transverse momentum corrections for the pressure boundary conditions
J	Fluid flow
μ	Dynamics viscosity
ν	Kinematic viscosity
ΔP	Pressure drop
κ	Intrinsic permeability
β	Brinkman's effective viscosity
ε	Fractional error
C_D	Drag force coefficient
σ	Effective media parameter
n_s	Solid fraction (equivalent to the effective media parameter σ)
γ	Surface tension
M^*	Molar mass
R	Universal gas constant
T	Temperature
T_c	Critical temperature
V	Volume
P	Pressure
$P_{\alpha,\beta}$	Pressure tensor
ξ	Pressure scaling factor
p_0	Bulk pressure

θ	Reduced temperature
θ_c	Reduced critical temperature
χ	Parameter related to the surface tension
ρ_c	Reduced critical density
ρ_{liquid}	Reduced liquid density
ρ_{gas}	Reduced gas density
ω	Width of the liquid - vapour interface
λ	Parameter related to the Galilean invariance
$\omega^{p,t,\alpha\alpha,\alpha\beta}$	Adjustable constants
Ψ	Free energy functional
ψ	Free energy density
Φ	Surface free energy density
ϕ	Wetting potential between fluid and solid
Ω	Dimension-less wetting potential between fluid and solid
Θ	Contact angle between liquid fluid and solid
$\phi_{\alpha,\beta}$	Wetting potential between α and β
$\Theta_{\alpha,\beta}$	Contact angle between liquid in α and surface of β
ϕ_{grey}	Internal wetting potential of grey nodes
S_ζ	Surface ζ
V_{grey}	Volume of grey nodes

1 Introduction

Contents

1.1 Concrete	1
1.2 From concrete to cement paste	1
1.3 Indicators of durability	3
1.4 Statement of the problem	4

1.1 Concrete

Concrete is the most widely used material on Earth. The current yearly production exceeds 10^{10} m^3 and is enough to build a 5 m^2 beam that stretches from Earth to the Moon*. This huge ever-increasing volume means that, although concrete is a material with intrinsically low CO_2 emissions, it is responsible for some 5 to 8% of global man-made emissions [1]. Consequently, it is of great environmental interest to design new concretes with lower CO_2 footprints. Nonetheless, the *challenge* is that they must have comparable or improved, and predictable properties, notably in terms of resistance to degradation and durability.

Water transport underpins most physical and chemical degradation mechanisms. Water is transported through porous materials by advection, diffusion, and absorption. In concrete structures, the transport of water strongly impacts durability both directly, *e.g.* freeze-thaw action, and indirectly by permitting the ingress of *aggressive* ions.

1.2 From concrete to cement paste

Concrete is made by mixing aggregates, cement and water. The water reacts with cement to form cement paste, the glue that binds the aggregates together to form a rock-solid mass. Concrete is often regarded as a composite material composed of aggregates, cement paste

* Unfortunately, gravity prevents us from doing so.

Chapter 1. Introduction

and an interfacial transition zone (ITZ) between them. The ITZ is the region of the paste that surrounds the aggregates and is perturbed their presence. This perturbation leads to a local increase in porosity [2]. The properties of concrete are dependent on the individual properties of its components but are mainly determined by the quality of the cement paste. Therefore, the introduction of any new concrete must be preceded by a quantitative understanding of the microstructure, properties and durability of cement paste.

Cement paste is made by mixing cement and water. The chemical reactions between the anhydrous cement and water lead to the formation of hydrates (figure 1.1). As the degree of hydration increases with time, the total porosity of cement paste, *i.e.* the fraction that is not solid, decreases. The main hydrate phase, calcium silicate hydrate (C-S-H), is a nano-porous material that fills about 50% of the volume of the paste (figure 1.1). It comprises inter-layer spaces (~ 1 nm) and gel pores ($\sim 3 - 5$ nm) [3]. The space not filled by hydrates is referred to as capillary porosity (or inter-hydrate porosity) and has a characteristic size that ranges from 10 to 100 nm. Figure 1.2 shows the evolution of the volume composition of a white cement paste with a water-to-cement (w/c) ratio of 0.4.

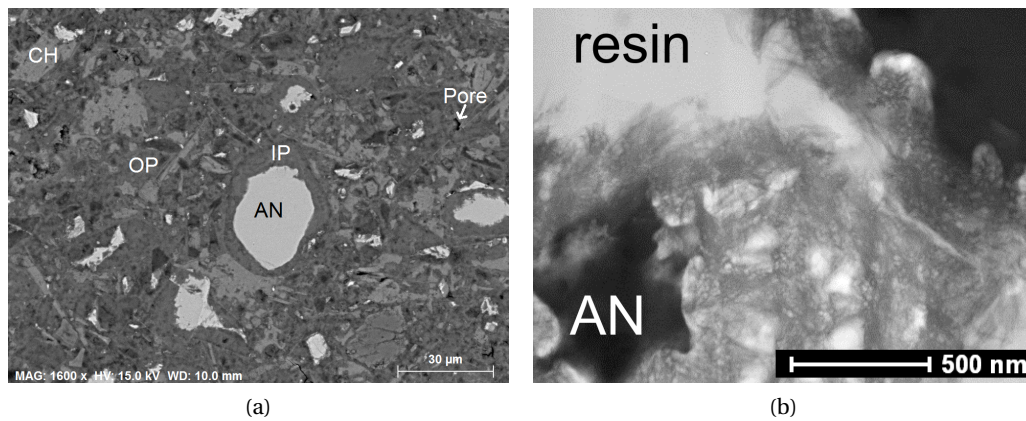


Figure 1.1: (a) Back-scattered electron microscopy for a 28 days old cement paste. Image by Elise Berodier. (b) Transmission electron microscopy of a 1 day old cement paste. Image by Amelie Bazzoni. AN: Anhydrous cement; IP: Inner product (C-S-H); OP: Outer product (C-S-H); CH: Portlandite.

The absolute volume of the solid plus liquid part of the cement paste decreases with time because the volume of the hydrates is smaller than the combined volumes of the reactants (anhydrous cement and water). This is called chemical shrinkage. Initially this decrease is accommodated by overall changes in the volume of the paste. However, from initial setting, the paste starts to resist deformation which causes the formation of micron-sized voids within the capillary porosity. Without an external source of liquid water, these pores remain empty. Unreacted water occupies other capillary pores with sizes ranging up to a few microns [3]. The total capillary porosity (water-filled and void) of a mature cement paste with a water-to-cement ratio of 0.4 is of the order of 7 – 11%. Figure 1.3 recaps the dimensional range of pores in hydrated cement paste.

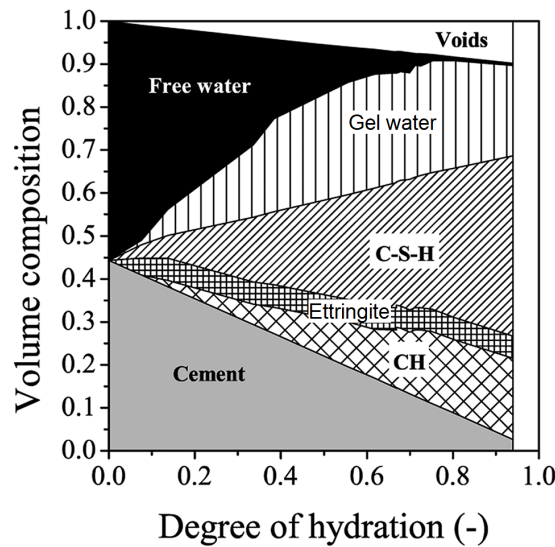


Figure 1.2: Volume composition of a white cement paste with a water-to-cement ratio of 0.4. Adapted from [3].

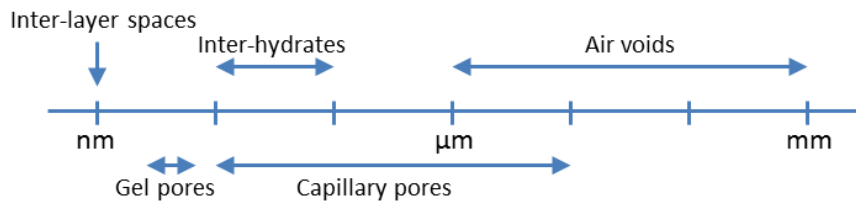


Figure 1.3: Dimensional range of pores in hydrated cement paste.

1.3 Indicators of durability

In practice, the deterioration of cementitious structures is rarely due to a single cause. It is generally the result of decades of coupled physical and chemical reactions. Nonetheless, there are several measurable quantities that are used as *indicators* of the durability of cementitious materials. Some of the most widely used indicators are briefly described below.

The porosity is often used as a *stand-alone* indicator of durability. Analysis range from simple measurements of the total porosity to more complex mercury intrusion experiments which additionally reveal the pore break-through diameter of the material. Simple porosity measurements, such as those that estimate the porosity from the difference in weight between the water-saturated and oven-dried samples, are attractive. However, the problem is that the measured porosity includes the chemically and physically bound water molecules that do not necessarily contribute to the transport properties. Hence, the transport properties, such as permeability, sorptivity and diffusivity correlate better with the durability of structures. Moreover, these transport properties correlate relatively well between them although permeability is more sensitive to the presence of micro-cracks and changes in total porosity, compared with

diffusivity or sorptivity [4].

The intrinsic permeability characterizes a medium from the perspective of pressure-induced fluid flow through the *fully* saturated porosity. It quantifies the ability of a material to resist fluid penetration and consequently correlates well with durability. It is related to macroscopic observables through Darcy's law [5]. For cement paste with water-to-cement ratios ≤ 0.5 , it is very low and difficult to measure reliably. Hence, there is a paucity of experimental data and a considerable variability.

With the exception of the near-surface, concrete structures are rarely saturated with water. In partially-saturated materials, suction leads to the uptake of water. This is called absorption and can be described by the extended Darcy equation. Moreover, the partially saturated structures can be exposed to variations in the ambient relative humidity (RH). These changes lead to the egress (desorption) and ingress (adsorption) of liquid water and vapour. The adsorption and desorption isotherms, also known as the water isotherms, describe the equilibrated systems below full saturation and quantify the liquid - vapour - solid interactions.

The diffusion of water vapour and ions affect the durability of cementitious structures. In practice, ions, such as chloride and sulfates, diffuse in the liquid-saturated part of the structures. The former causes extensive cracking and the latter leads to the corrosion of the steel rebars. Other degradation mechanisms that are based on diffusion include carbonation where the CO_2 diffuses through the empty porosity and reacts with the portlandite. Although the mechanisms that govern the water vapour and gas diffusion are dissimilar, the latter is often used as a durability indicator because it is easier to measure.

1.4 Statement of the problem

The measurement of transport properties is necessary to control the quality and predict the durability of cement paste. However, the experiments are often time-consuming and in some cases, *e.g.* permeation of water, show a large unexplained scatter and anomalous behaviour (see chapter 2).

Computer models can help address these problems. More importantly, they can help to understand the link between the microstructure and the performance of the material. They also make it possible to isolate the effects of various parameters which is very difficult to do in experiments. These advantages are critical en route to develop better, more predictable materials.

Computational fluid dynamics models have been successfully used to understand water transport in a wide range of porous media including sandstones [6], carbonates [7] and fuel cells [8]. However, their application to cement paste remains rather limited [9, 10, 11, 12, 13]. Numerical models have been restricted to either molecular dynamics simulations at the nano-scale [14, 15] or to rather simplified models of flow through the micron-sized capillary pores

[9, 16, 17, 18, 10, 11, 12]. The general consensus is that the macroscopic properties of cement paste are governed by transport through the capillary pores. However, the models which are limited to the capillary pores fail to reproduce experimental measurements [9, 16, 18, 10, 11, 12]. Moreover, in aggressive environments where structures are exposed to sea-water, high performance concretes are often used. The cement pastes of these concretes have a smaller and finer porosity and the measurement of their transport properties is consequently more laborious and more time-consuming. These factors make it crucial to develop novel models that can predict the water dynamics and interactions in *both* capillary and C-S-H gel pores.

The objective of this thesis is to develop a numerical model that calculates the permeability of cement paste based on its microstructure. The layout of the thesis is as follows.

Chapter 2 reviews the experimental and numerical methods that are used to measure and model the permeability of cement paste. Emphasis is put on the large scatter in experimental data and on the limitations of the current numerical models.

Chapter 3 presents two lattice Boltzmann models for isothermal fluids. The first method is a relatively standard flow model that is limited to the capillary pores. The second additionally accounts for the flow through the C-S-H gel pores via an effective media approach. These two methods are used to simulate the permeability of model cement pastes in chapter 5 where it is shown that the degree of water saturation and the flow through the C-S-H are critical to correctly match the experimental permeability measurements.

In chapter 4, the lattice Boltzmann permeability model is extended to non-ideal fluids described with an equation of state. This modification is necessary to model the desorption and adsorption of liquid water and vapour in the capillary pores. The model is further extended to include the transport and isotherms in the C-S-H gel pores. This is achieved with a novel effective media approach implemented within a free energy framework. The method is demonstrated in section 4.2.6 on *pseudo*-random cement-like systems. It is shown that the novel LB model can reproduce a two-step isotherm where the first corresponds to the capillary pores and the second to the smaller gel pores. It is also shown that the model can reproduce the *ink-bottle* effect. The model is used to simulate the desorption and adsorption in model cement pastes in chapter 6 where it is shown that it is critical to take into account the C-S-H gel pores in order to match the experimental water isotherms.

Finally, chapter 7 summarizes the *insights* discovered during this thesis and provides an outlook for possible future work.

2 Permeability of Cement Paste: State-of-the-art

Contents

2.1 Darcy's law	7
2.2 Experimental techniques	8
2.3 Modelling techniques	10
2.3.1 Empirical models	10
2.3.2 Numerical models	11
2.4 Experiments and models: a mismatch ?	15

This chapter reviews the techniques that are used to calculate the permeability of cement paste. First, section 2.1 introduces Darcy's law. Then, sections 2.2 and 2.3 discuss the experimental and numerical techniques that are used to measure and model permeability, respectively. Finally, section 2.4 discusses the reasons behind the mismatch between the experiments and models.

2.1 Darcy's law

The intrinsic* permeability κ characterizes a medium from the perspective of pressure-induced fluid flow through the *fully* saturated porosity. For incompressible liquids and viscous flows, it is related to macroscopic observables through Darcy's law [5] which may be written under the form:

$$\kappa = \frac{L_0}{A} \frac{\mu J}{\Delta P} \quad (2.1)$$

for a sample of length L_0 and cross-sectional area A through which a fluid flow J is driven by an applied pressure gradient ΔP (figure 2.1). The dynamic fluid viscosity is $\mu = \rho \nu$ where ρ is

*The non-intrinsic permeability, also called hydraulic conductivity, is fluid dependent and is expressed in m.s^{-1} . The ratio of intrinsic permeability to hydraulic conductivity is given by $\mu/\rho g$ where g is the acceleration due to gravity. For water at 20° , $\mu/\rho g \approx 10^{-7}$ m.s.

the density and ν is the kinematic viscosity. The intrinsic permeability is expressed in units of $[L]^2$ and is usually expressed in m^2 or mD^\dagger .

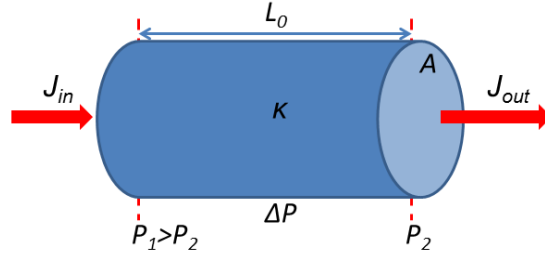


Figure 2.1: Schematic illustration of Darcy's law.

The intrinsic permeability can be measured using various techniques. A standard methodology consists of applying a pressure gradient in one spatial direction, measuring the fluid inflow and / or outflow, and calculating the permeability using Darcy's law (equation 2.1).

2.2 Experimental techniques

The water permeability of cement paste is challenging to measure with standard methods because it is difficult to force a measurable liquid flow through the paste. Measurement of gas permeability is easier but requires prior drying of the sample to a well-defined state of saturation which may take more than one year and could induce micro-cracks. Nonetheless, standard permeability techniques have been used to measure the permeability of cement paste by many authors [19, 20, 21, 22, 4]. For a material with low porosity and / or high tortuosity, the required time to reach steady-state is very long. Hence, indirect measurement methods such as beam-bending [23] have also been employed.

Table 2.1 shows a selection of measured permeabilities for mature cement pastes with water-to-cement ratios around 0.4. There is a large unexplained scatter. Measured values range from 10^{-22} to $10^{-16} m^2$. In theory, the intrinsic permeability is a property of the medium and is independent of the penetrating fluid or applied pressure. However, contrary to expectations, the reported values suggest that the intrinsic permeability of cement paste is strongly dependent on the penetrating fluid. Measurements with oxygen [4] as the permeating fluid are 3 to 5 orders of magnitude greater than typical values obtained using water [20, 21]. A similar discrepancy is observed for other cementitious materials [27, 28]. Moreover, for the same fluid (water), the permeability measurements span 2 to 3 orders of magnitude [24, 21]. Even for nominally similar pastes with comparable cement composition, water-to-cement ratio and hydration age, the measured permeability values differ by a factor of four.

Several hypotheses have been advanced to try and explain these anomalies including: gas slippage on the surface of the pores [27]; microcracks induced by sample drying prior to

[†]One Darcy is equivalent to $9.87 \times 10^{-13} m^2$.

2.2. Experimental techniques

Table 2.1: Experimental permeability measurements for mature cement paste with water-to-cement mass ratios (w/c) ranging from 0.35 to 0.47.

	Method	Fluid	Conditioning	w/c	Age (days)	Intrinsic permeability (m^2)
Nyame & Illston 1981 [20]	Standard permeability cell	Water	Cured underwater (no information about the delay before placing underwater)	0.47	600	5×10^{-22}
Banthia & Mindess 1989 [21]	Tri-axial permeability cell	Water	Sealed for 24h then cured underwater	0.35	28	8.9×10^{-20}
Ai <i>et al.</i> 2001 [24]	Thermo-permeatry	Water	Sealed and moist cured for 24h then cured underwater	0.4	548	10^{-22}
Vichit-Vadakan & Scherer 2002 [25, 26]	Beam-bending	Water	Sealed for 48h then cured underwater	0.4	14	5×10^{-22} -10^{-21}
Vichit-Vadakan & Scherer 2003 [23]	Beam-bending	Water	Sealed for 18h then cured underwater	0.45	3	6×10^{-22}
Ye 2005 [22]	Three parallel permeability cells	Water	Sealed. Vacuum saturated with water for 4-8h prior to measurement	0.4	28	9×10^{-21}
Grasley & Scherer 2007 [26]	Dynamic pressurization	Water	Sealed for 12-18h then cured underwater	0.4	14	2×10^{-21}
Wong <i>et al.</i> 2009 [4]	Standard permeability cell	Oxygen	Sealed. Dried prior to measurement	0.45	90	6.5×10^{-17}

gas permeability measurements [4]; delayed cement hydration [28, 29]; swelling of cement hydrates in contact with water [29] and dissolution and migration of fine elements [21, 28, 29, 30]. However, an examination of the results shows that none of the hypotheses discussed above is sufficient to explain fully the wide variation of results.

A plausible hypothesis is the variation in the degree of water saturation, defined as the fraction of the porosity that is filled with water. Abbas *et al.* [31], Baroghel-Bouny *et al.* [32] and Wong *et al.* [33] showed a strong dependency of the intrinsic gas permeability on the degree of water saturation for concretes, mortars and other cement-based materials. At the start of this work, the author was not aware of any similar study on cement paste using water as the permeating fluid. Only very recently, Zamani *et al.* [34] measured the water permeability of cement paste as a function of the internal relative humidity (RH) using a combination of ^1H nuclear magnetic resonance (NMR) analysis and empirical modelling. In general, although experimentalists try to ensure water saturation before measuring water permeability, total saturation might be difficult to establish and maintain. The analysis of the procedures leading to the results reported in table 2.1 suggests that none of the measurements of water permeability to date has actually been carried out on a *fully* saturated material.

The differences in water saturation of the capillary porosity primarily originate from the conditioning of the samples after mixing. In systems which are cured sealed, the chemical shrinkage voids are necessarily devoid of liquid water. In underwater cured systems, it is often assumed that water is drawn into the voids as they form. However, this depends on the size of the paste and the delay in exposing it to additional water. Water cannot permeate across more than millimetre-sized samples on the timescale of the curing due to the rapidly decreasing permeability of the paste and the relatively small pressure head. Hence for large samples, such as might be used for permeability tests, and / or for water exposure delays of more than a few hours, a significant fraction of the chemical shrinkage porosity may remain devoid of liquid water. This is confirmed by recent ^1H NMR experiments, which have also shown that it is difficult, if not impossible, to subsequently saturate the shrinkage voids even when using vacuum saturation on small samples [35]. This argument will be further developed in sections 5.2.2 and 5.2.5 of chapter 5.

2.3 Modelling techniques

Models of water transport can be divided into two main categories. In the first category, simple experimental measurements are combined with empirical equations in order to predict the transport properties. In the second category, the flow is simulated through the explicitly resolved porosity by solving or approximating the equations of flow. In this case, the pore structure can be obtained by imaging techniques or simulated with a microstructural model.

2.3.1 Empirical models

Empirical equations can be combined with experimental measurements such as mercury intrusion porosimetry (MIP) and electrical conductivity to calculate the water permeability. For example, Katz and Thompson [36] proposed an empirical relation that describes the permeability of rocks saturated with a single liquid phase with $\kappa = c l_c^2 \frac{\sigma}{\sigma_c}$. Here, l_c is the characteristic pore size, σ is the conductivity of the rock saturated with a brine solution

of conductivity σ_0 , and c is a constant on the order of $1/226$. They reported an excellent relationship between the calculated and measured permeabilities for various sandstones [36, 37]. El-Dieb and Hooton [38] and Christensen *et al.* [39] used the Katz and Thompson model to calculate the permeability of cement paste. They both reported a poor linear relationship between the measured and calculated permeabilities. There are several reasons that can explain the discrepancy. First, the Katz and Thompson equation was developed for fully saturated rocks. As discussed in section 2.2, it appears that the cement paste samples that are used for permeability experiments may not be fully saturated. Second, the Katz and Thompson equation was tested on various sandstones. These rocks have a relatively coarse porosity. Cement paste has a finer porosity and a wider pore size distribution with multiple characteristic pore sizes (mainly capillary and gel pores). Third, it is unclear how pore sizes determined with MIP on dried samples can be used to estimate the permeability of virgin samples [38, 40].

Along these lines, Cui and Cahyadi [41] included the contribution of the C-S-H gel pores in the permeability calculation by using an analytical expression derived from the general effective media theory [42] for the calculation of the conductivity of bi-composite materials. The pore structure characteristics were determined by MIP and the volume of hydrates with Power's model. They reported permeability coefficients in good agreement with measurements for different w/c ratios and degrees of hydration. However, the model requires input quantities that are practically impossible to measure such as the critical volume fraction of C-S-H. Moreover, similarly to the application of the Katz and Thompson model to cement paste, it is unclear how pore sizes determined with MIP on dried samples can be used to estimate the permeability of virgin samples [38, 40].

2.3.2 Numerical models

Pore structure of cement paste

Imaging techniques The pore structure of cement paste can be reconstructed using microtomographic images obtained with, for example, scanning electron microscopes or focused ion beam. Although the obtained structures are realistic, there are several limitations. For instance, the resolution is often limited to $\sim 0.1 - 1 \mu\text{m}$ which means that the inter-hydrates and fine capillary pores cannot be resolved. Additionally, the resolution is larger than the break through diameter obtained from mercury intrusion experiments. For example, figure 2.2 shows the pore size distribution for a 28 days old cement paste with a water-to-cement ratio of 0.4 as obtained from a mercury intrusion experiment. The pore break-through radius is of the order of 7 - 20 nm. This is smaller than the minimum feature that can be resolved with traditional imaging techniques. Moreover, most imaging techniques require drying of the sample which might damage the microstructure.

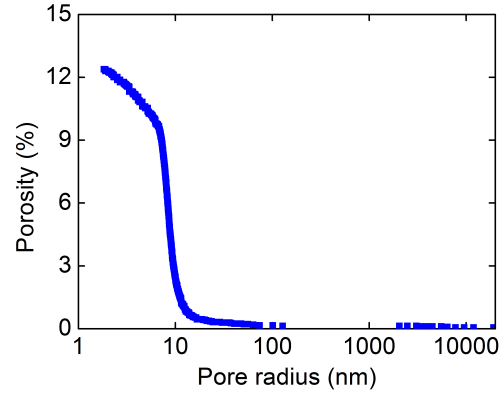


Figure 2.2: Pore size distribution of a 28 days old cement paste with a w/c ratio of 0.4 as obtained with mercury intrusion porosimetry. Data from Elise Berodier.

Microstructural models Microstructural models of cement paste have been developed for the purpose of understanding cement hydration and kinetics. Some of these models account for a range of properties derived from the chemistry and thermodynamics of cement such as phase composition, assemblage and interactions during the hydration processes. HYMOSTRUC3D [43], CEMHYD3D [44] and μic [45] are amongst the leading models.

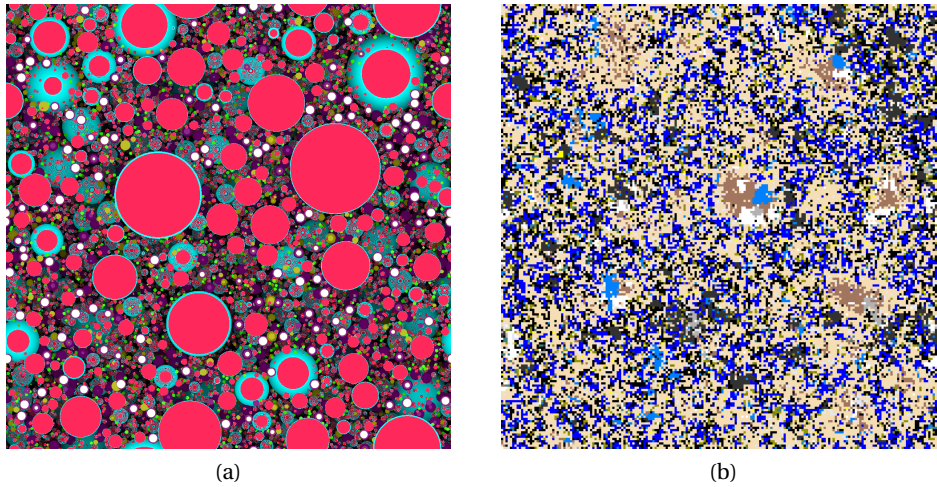


Figure 2.3: 2D images of cement model microstructures as obtained with (a) μic and (b) CEMHYD3D. The microstructures are $(100 \mu m)^3$ in size. In (a) The model is of a white cement paste with a w/c ratio of 0.4 and after 17 hours of hydration. The main phases are alite (red), monosulfate (purple), ettringite (pale green), aluminate (white), C-S-H (cyan), portlandite (green) and pores (black). In (a), (b) the model is of a CEM I cement paste with a w/c ratio of 0.5 and after 28 days of hydration. The main phases are: alite (light brown), belite (blue), aluminate (grey), aluminoferrite (white), C-S-H (beige), portlandite (dark blue) and pores (black).

HYMOSTRUC3D uses the vector approach to generate resolution-free microstructures. How-

ever, it is severely limited in so much as it combines all the hydration products and grows the microstructure as expanded spheres based on the original cement particle distribution without taking into account interactions with neighbours. In so doing, it is unable to fully capture the microstructural complexity of cement paste.

CEMHYD3D is lattice based and consequently more complex particle shapes may be modelled than in HYMOSTRUC3D. However, practical computer and imaging resources limit the minimum particle sizes to around 1 to 0.25 μm . Consequently, the pore network of the microstructures tends to depercolate at relatively high porosities.

The microstructural model μic uses the vector approach and is hence inherently resolution-free. However, in contrast with CEMHYD3D and HYMOSTRUC3D, μic is offered as a platform where the user can define the physical and chemical properties as illustrated in figure 2.4. The

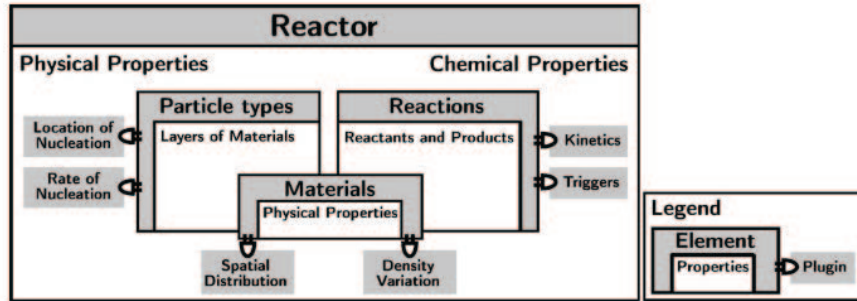


Figure 2.4: Elements in μic with examples of customizable properties and plugins. Figure adapted from [45].

core of the model serves as a stand-alone module that provides the user with means to input the properties of the cement and the rules of hydration. Afterwards, μic calculates the reactions and outputs the vector microstructures. In contrast with HYMOSTRUC3D, the platform allows the hydrates to nucleate in the pore space and explicitly accounts for impingement between neighbouring grains. Moreover, μic employs efficient implementations of data-structure algorithms that allow the simulation of the hydration of cements with realistic particle size distributions. Furthermore, the user can also create plugins to describe, for example, the morphology of the hydration products (*e.g.* C-S-H).

Simulation of flow through the pore structure

The porosity of cement paste is complex and heterogeneous. It is consequently impossible to find analytical solutions for the equations of flow. Nonetheless, the flow can be solved with two different approaches.

Network models In the first approach, the pore network is divided into a series of nodes representing pores that are linked together by cylinders. The lengths and radii of the cylinders

are determined by the pore separation and throat size. Then, the equations of *laminar* flow within this network of cylinders, essentially a large set of simultaneous equations, are solved.

Most previous attempts to simulate the water permeability of cement paste are based on such *network* models [16, 18, 17]. Pignat *et al.* [16] reported intrinsic permeability values of the order of 10^{-13} to 10^{-15} m² depending on the porosity and the cement particle size distribution using the microstructural model IKPM, a precursor of μic , for a w/c ratio of 0.42. Using microstructures simulated with HYMOSTRUC3D, Ye *et al.* [18] reported permeabilities varying from 10^{-16} to 10^{-20} m² depending on the porosity for a paste with a w/c ratio of 0.4. Related to these studies, Koster *et al.* [17] derived a network model from 1 μm resolution 3D micro-tomographic images of cement pastes and calculated a *single* permeability value of 9.3×10^{-20} m² for a sample with a w/c ratio of 0.45 and a degree of hydration of 0.67.

The large difference in the values reported by Pignat *et al.* [16] and Ye *et al.* [18] is rather surprising since they both approximate the flow using network models in microstructures essentially composed of overlapping spheres. At similar porosities, $\sim 20\%$, Pignat *et al.* report a permeability of $\sim 3 \times 10^{-15}$ m² while Ye *et al.* report a permeability of $\sim 10^{-19}$ m². This difference outlines the degrees of *freedom* that are available in network models due to the different possible means to *choose* the number, radius and connectivity of the nodes.

Discrete models To avoid *inadvertent* change of the pore structure, the second approach consists of solving - not approximating - the equations of flow using numerical methods such as finite element or lattice Boltzmann. This approach removes the requirement to reduce the highly complex pore structure into a series of cylinders and was previously used by Garboczi and Bentz [9] and Zhang *et al.* [12].

Garboczi and Bentz [9] used a lattice Boltzmann model to calculate the permeability of CEMHYD3D cement paste microstructures as a function of the capillary porosity and microstructure resolution (minimum particle size). They reported that the calculated permeability was very sensitive to the resolution of the microstructure and at the highest resolution studied (0.25 μm), the permeability was circa 10^{-17} m² at a capillary porosity of 12%. Most recently, Zhang *et al.* [12] used the LB method to calculate the permeability of HYMOSTRUC3D cement paste microstructures. They reported a permeability of approximately 2×10^{-18} m² for a w/c ratio of 0.4, a hydration age of 50 days and a microstructure resolution of 0.5 μm .

In general, the water permeabilities obtained with discrete numerical models are of the order $10^{-17} - 10^{-18}$ m², several orders of magnitude larger than the lowest water permeability measurement and closer to the gas result (table 2.1).

2.4 Experiments and models: a mismatch ?

The measured permeabilities show a considerable scatter. For mature cement pastes with w/c ratios around 0.4, the permeabilities range from 10^{-22} to 10^{-16} m² (table 2.1). For reasons outlined in section 2.2, it appears that most measurements have been done on non-saturated samples. In this case, the measurements are no longer of intrinsic permeability.

The values obtained using computer models are scattered as well and range from 10^{-20} to 10^{-15} m². Here, there are several problems that need to be addressed. First, previous simulations only addressed fully saturated porosity. Hence, they cannot be compared to the reported experiments without matching the conditioning of the samples in the experiments with the degree of water saturation in the models. Second, at high degrees of hydration and low degrees of water saturation, the *water-filled* capillary porosity depercolates and the nano-porosity of the C-S-H becomes crucial to maintain the percolation of the water-filled pore network. Previous simulations only addressed the capillary porosity and ignored the nano-scale porosity. With the exception of the analytical work of Cui and Cahyadi [41], all the simulations discussed above treated the C-S-H phase as an impermeable solid with no inherent porosity. This makes the percolation of the pore network, and thus the permeability, critically dependent on the resolution of the microstructures. These factors lead to an overestimation of the permeability at large porosity and cause it to fall catastrophically to zero below the percolation threshold of the capillary porosity.

Consequently, what is required to clear up the *mismatch* is a numerical model that can account for the degree of water saturation and solve the flow in *both* the capillary and gel pores. Discrete methods, such as finite element and lattice Boltzmann, can do so. Additionally, they offer the advantage of solving the flow without the need to reduce the pore structure into a series of cylinders. Furthermore, they can help develop more pathways for testing the microstructural models of cement paste against experimental data.

In this context, the lattice Boltzmann method was selected for solving the equations of flow. It was previously used by Garobczi and Bentz [9] to calculate the permeability of cement paste and by Svec *et al.* [46] to study the flow of fibre reinforced self-compacting concrete during a slump test. Besides the advantages discussed in the last paragraph, it offers the ability to deal implicitly with arbitrarily shaped geometries which is critical for complex porous media like cement paste. Moreover, the computer code that would be initially developed for permeability could be extended to model a wide range of transport phenomena including diffusion and desorption. In the latter case, lattice Boltzmann methods give a significant advantage over other discrete methods because they offer an implicit tracking of the liquid - vapour interfaces.

3 Lattice Boltzmann Methods for Isothermal Fluids

Contents

3.1 Standard methods	17
3.1.1 Overview	17
3.1.2 Collision operators and equilibrium functions	20
3.1.3 Boundary conditions	21
3.1.4 Definition of a lattice Boltzmann algorithm	23
3.1.5 Implementation	23
3.1.6 Methods for calculating permeability	24
3.1.7 Validation	24
3.2 Effective media methods for the transport properties	27
3.2.1 Overview	27
3.2.2 Theory	29
3.2.3 Implementation	31
3.2.4 Methods for calculating permeability	32
3.2.5 Validation	32

3.1 Standard methods

3.1.1 Overview

Over the past 25 years, a new class of computational fluid dynamics solver, the lattice Boltzmann (LB) method, has emerged [47, 48, 49, 50, 51, 52, 53, 54]. A large amount of research effort has resulted in a large inventory of lattice Boltzmann algorithms suitable for a wide range of applications including the simulation of multi-component [55] and multi-phase non-ideal fluids [56], chemical reactions [7], turbulence [57], magneto hydrodynamics [58], relativistic hydrodynamics [59], heat transfer [60] and free surface flows [61]. The successful development of LB methods is due to several factors. First, in its most basic form, an LB

algorithm is easier to implement than other computational fluid dynamics solvers based on the direct discretization of the Navier-Stokes equations. Second, the LB methods are based on a mesoscopic description of fictitious fluid particles. This makes it easy to incorporate several types of interactions between the fluid particles, and to describe interactions between the fluid and solid boundaries. This includes the ability to describe complex boundaries by means of very simple arithmetical operations. Moreover, due to the local nature of the interactions, most LB algorithms are highly amenable to parallelization and can take advantage of the recent growth in computing power.

Historically, the lattice Boltzmann approach developed from the lattice gas method [48, 49] but it can also be directly derived from the Boltzmann equation [62] which describes the statistical behaviour of a system that is not in thermodynamic equilibrium. Under appropriate conditions, the LB equations are formally equivalent to the Navier-Stokes equations discretized in space and time [51]. The Navier-Stokes equations emerge from applying the second law of Newton to fluid motion and assuming that the stress in the fluid is the sum of a pressure term and a diffusing viscous term. They are of paramount importance in physics as they successfully describe, amongst other things, water flows, oceans currents and air turbulence.

In LB methods, at each node of a discrete lattice mesh, the fluid is represented by a density distribution of Q fluid elements each with a defined lattice velocity performing consecutive propagation and collision steps as illustrated in figure 3.1

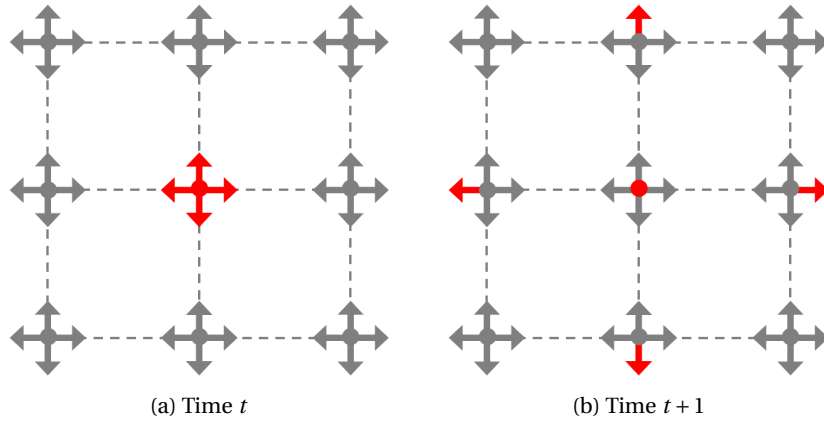


Figure 3.1: 2D illustration of the distribution functions (a) before and (b) after a streaming step in the lattice Boltzmann method.

The lattices grids must fulfil certain symmetry conditions in order to recover hydrodynamics behaviour with full rotational symmetry of space. The most widely used lattice is the $D3Q19$ where $D3$ denotes a three-dimensional lattice and $Q19$ stands for 19 discrete velocities (figure 3.2).

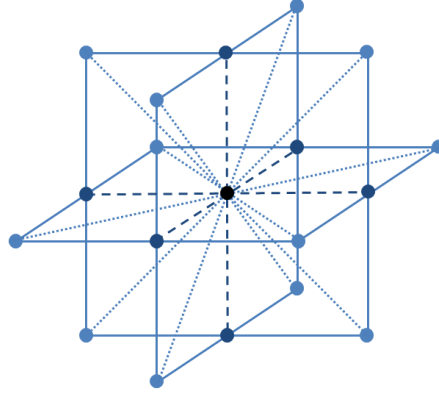


Figure 3.2: $D3Q19$ lattice with three sub-lattices and 19 discrete velocities: rest position (black), six velocities towards face centres (dark blue) and 12 velocities towards the edge centres of the cube (light blue).

In this case, the velocity vectors \mathbf{e}_i are given by:

$$\mathbf{e}_i = \begin{cases} (0, 0, 0) & \text{for } i = 1 \\ (\pm 1, 0, 0), (0, \pm 1, 0), (0, 0, \pm 1) & \text{for } i = 2 - 7 \\ (\pm 1, \pm 1, 0), (\pm 1, 0, \pm 1), (0, \pm 1, \pm 1) & \text{for } i = 8 - 19 \end{cases} \quad (3.1)$$

where $i = 1 \dots 19$ represent a stationary velocity, six velocities towards face centres and 12 velocities towards the edge centres of a cube.

The standard LB method can be encapsulated in:

$$f_i(\mathbf{r} + \mathbf{e}_i \Delta t, t + \Delta t) - f_i(\mathbf{r}, t) = \Delta t \sum_{j=1}^Q S_{ij} \left(f_j(\mathbf{r}, t) - f_j^{eq}(\mathbf{r}, t) \right) + \mathbf{F}. \quad (3.2)$$

Here \mathbf{r} is a lattice node and Δt is the simulation time step. The functions f_i represent the density of fluid at position \mathbf{r} and time t moving with velocity \mathbf{e}_i . The first term on the RHS of equation 3.2 is the collision operator in which S_{ij} is the collision matrix that serves to relax the fluid towards an equilibrium distribution $f_j^{eq}(\mathbf{r}, t)$ that encapsulates the physics of the problem. Lastly, \mathbf{F} is the external forcing that describes, for example, gravity or interfacial tension.

In the absence of external forces, the macroscopic density $\rho(\mathbf{r}, t)$ and momentum $\rho(\mathbf{r}, t)\mathbf{u}(\mathbf{r}, t)$ are calculated from the distribution functions as:

$$\rho(\mathbf{r}, t) = \sum_{i=1}^Q f_i(\mathbf{r}, t) \quad (3.3)$$

and

$$\rho(\mathbf{r}, t) \mathbf{u}(\mathbf{r}, t) = \sum_{i=1}^Q f_i(\mathbf{r}, t) \mathbf{e}_i \quad (3.4)$$

where $\mathbf{u}(\mathbf{r}, t)$ is the macroscopic velocity.

3.1.2 Collision operators and equilibrium functions

The collision operator serves to relax the fluid towards the equilibrium functions. A very widely used approximation of the collision operator is the Bhatnagar-Gross-Krook (BGK) model [51], also known as the single-relaxation-time (SRT) model. This model reduces the collision operator to

$$S_{ij} = -\frac{1}{\tau} \delta_{ij} \quad (3.5)$$

where τ is the relaxation time and $\delta_{ij} = \begin{cases} 0 & \text{if } i \neq j \\ 1 & \text{if } i = j \end{cases}$ is the Kronecker delta. The first term of the RHS of equation 3.2 becomes:

$$\sum_{j=1}^Q S_{ij} (f_j(\mathbf{r}, t) - f_j^{eq}(\mathbf{r}, t)) = -\frac{1}{\tau} (f_i(\mathbf{r}, t) - f_i^{eq}(\mathbf{r}, t)). \quad (3.6)$$

The relaxation time τ is related to the kinematic fluid viscosity ν through

$$\nu = c_s^2 \left(\tau - \frac{\Delta t}{2} \right) \quad (3.7)$$

where $c_s^2 = \frac{c^2}{3}$ is the lattice speed of sound with $c = \frac{\Delta x}{\Delta t}$ the lattice speed and Δx the lattice spacing.

Under certain conditions, the SRT collision operator yields unphysical behaviour such as viscosity-dependent permeability [63, 64, 65]. To overcome this problem, the multi-relaxation-time (MRT) scheme [63] was developed. In this version, the linearized collision operator is implemented in the hydraulic modes of the problem instead of the space of discrete velocities. The hydraulic modes include hydrodynamic conserved quantities such as the density and momentum and other non-conserved quantities. The first term of the RHS of equation 3.2 becomes:

$$\sum_{j=1}^Q S_{ij} (f_j(\mathbf{r}, t) - f_j^{eq}(\mathbf{r}, t)) = -\mathbf{M}^{-1} \cdot \mathbf{S} (\mathbf{m}(\mathbf{r}, t) - \mathbf{m}^{eq}(\mathbf{r}, t)) \quad (3.8)$$

where \mathbf{S} is a diagonal relaxation matrix and \mathbf{M} is a 19×19 transformation matrix that links the

hydraulic modes \mathbf{m} with the distribution functions \mathbf{f} by:

$$\mathbf{m} = \mathbf{M} \cdot \mathbf{f} \quad (3.9)$$

$$\mathbf{f} = \mathbf{M}^{-1} \cdot \mathbf{m}. \quad (3.10)$$

For the $D3Q19$ lattice, out of the 19 moments, only the density ρ and momentum (j_x, j_y, j_z) are conserved and measurable quantities. The other moments can be used to improve the numerical stability [63] by adjusting their corresponding relaxation times. The MRT model can be regarded as the more general collision operator, and can be simplified to recovered the SRT model or a two-relaxation-time (TRT) model as proposed in [64, 65]. More information about the MRT collision operator can be found in appendix A.

Regardless of the collision operator, the underlying physics of the problem is defined by the equilibrium distribution functions f_j^{eq} . For incompressible isothermal fluids, the equilibrium distribution functions are [51]:

$$f_i^{eq}(\mathbf{r}, t) = \omega_i \rho \left(1 + \frac{\mathbf{u}^* \cdot \mathbf{e}_i}{c_s^2} + \frac{(\mathbf{u}^* \cdot \mathbf{e}_i)^2}{2c_s^4} - \frac{\mathbf{u}^* \cdot \mathbf{u}^*}{2c_s^2} \right), \quad (3.11)$$

where \mathbf{u}^* is the equilibrium velocity and is equal to the macroscopic velocity in absence of external forcing. The lattice weights ω_i are specific to the chosen lattice and are calculated in order to correct the lattice with respect to isotropy. For the $D3Q19$ lattice, they are:

$$\omega_i = \begin{cases} \frac{1}{3} & \text{for } \mathbf{e}_i = 0 \quad (i = 1) \\ \frac{1}{18} & \text{for } \mathbf{e}_i = 1 \quad (i = 2 - 7) \\ \frac{1}{36} & \text{for } \mathbf{e}_i = \sqrt{2} \quad (i = 8 - 19) \end{cases} \quad (3.12)$$

3.1.3 Boundary conditions

Fluid – solid boundaries

In computational fluid dynamics (CFD) models, the collision of the fluid with solid boundaries is usually accounted for by implementing a no-slip boundary condition. In lattice Boltzmann methods, the no-slip boundary condition is often approximated with the bounce-back rule [66]: if a fluid element hits a solid boundary following the propagation step, its momentum is reversed so that:

$$f_i(\mathbf{r} + \mathbf{e}_i, t + 1) = \tilde{f}_{\tilde{i}}(\mathbf{r}, t) \quad (3.13)$$

where \tilde{i} is the direction opposite to i : $\mathbf{e}_{\tilde{i}} = -\mathbf{e}_i$. This ability to handle highly irregular boundaries by means of simple arithmetical operations is one of the most appealing advantages of LB methods. The bounce-back rule is the most widely used fluid – solid boundary condition as it provides a very good compromise between ease of implementation, numerical performance and accuracy. The main draw-back of the bounce-back rule is that spherical structures

must be approximated with stair-case geometries (zig-zag type). Consequently, if the lattice resolution is coarse, the bounce-back rule introduces an artificial rugosity which might reduce the accuracy of the near-wall flow fields [53].

Open-flow boundaries

Unlike fluid – solid boundaries, open flow boundaries are not *physical* interfaces. In many CFD applications, the pressure or the velocity is fixed on a boundary in order to replicate an experimental condition (*e.g.* pressure head or wind speed). The former is referred to as Dirichlet boundary condition and the latter as Neumann boundary condition. In LB methods, the Dirichlet boundary condition can be replicated by applying a *body-force* [67] or by controlling the pressures at the inlet and outlet of the sample [68].

Body-force There are several ways to implement a body-force in lattice Boltzmann algorithms. Most commonly, an external force acting on all the fluid nodes is implemented by adding a term, *i.e.* \mathbf{F} , to the RHS of equation 3.2 and then modifying the macroscopic and equilibrium velocities accordingly [67, 68, 69]. Several mathematically derived variants exist. One variant consists of adding the term [67]

$$F_i = 3\omega_i \mathbf{e}_i \cdot \mathbf{g} \quad (3.14)$$

to the RHS of equation 3.2 where \mathbf{g} is the acceleration due to the external forces. The velocities become:

$$\mathbf{u}(\mathbf{r}, t) = \mathbf{u}^*(\mathbf{r}, t) = \frac{\sum_{i=1}^Q f_i(\mathbf{r}, t) \mathbf{e}_i}{\sum_{i=1}^Q f_i(\mathbf{r}, t)} + \frac{\mathbf{g}}{2} \quad (3.15)$$

where it is assumed that $\Delta t = 1$ and that the average density in the system is $\rho_0 = 1$.

Pressure boundary conditions An alternative way to control the flow takes advantage of the equation of state that links the pressure P to the density ρ by:

$$P = c_s^2 \rho. \quad (3.16)$$

Accordingly, it is possible to define regions with a certain pressure by setting the corresponding densities in a hydro-dynamically consistent way. Zou and He [68] first proposed how to implement pressure boundary conditions for the $D2Q9$ lattice and explained how to derive them for the $D3Q15$ lattice. Kutay *et al.* [70] extended the pressure boundary conditions to include the $D3Q19$ lattice. Most recently, Hecht and Harting [71] generalized the condition to include inflow with arbitrary velocity direction on $D3Q19$ lattices. The pressure boundary conditions are derived for LB algorithms by using the density and momentum equations. Due to the continuity relation, it is possible to specify three of the four variables (ρ, u_x, u_y, u_z) and

then solve for the fourth. Since the density must be fixed in order to control the pressure, it is possible to fix two out of the three components of the velocity. For example, in the most simple case, a pressure can be imposed by setting $\rho = \rho_0$, $u_y = u_z = 0$ and then solving for u_x . All of this is done by calculating and setting the appropriate values of the distribution functions. More information about pressure boundary conditions can be found in appendix B.

3.1.4 Definition of a lattice Boltzmann algorithm

A lattice Boltzmann algorithm consists of a combination of:

1. A set of equilibrium distribution functions that defines the *physics* of the problem (*e.g.* isothermal or non-ideal fluids).
2. A fluid – fluid collision operator that relaxes the system towards the equilibrium distribution functions.
3. A fluid – solid boundary condition that describes the interactions between the fluid and the solid (*e.g.* no-slip, wetting).
4. An open-flow boundary condition that replicates the experimental conditions (*e.g.* pressure head, gravity, wind speed, ambient relative humidity).

Finally, the algorithm is implemented in a computer program with an implementation language.

3.1.5 Implementation

As part of this work, a lattice Boltzmann algorithm was implemented to simulate the permeation of isothermal fluids in saturated porous media. The equilibrium distribution functions were defined with equation 3.11 to model an incompressible isothermal fluid. A multi-relaxation-time collision operator was implemented as developed by D’Humières *et al.* [63] and described in appendix A. The relaxation rates were chosen following the two-relaxation-time model [64, 65] so that:

$$\begin{aligned} s_1 &= s_4 = s_6 = s_8 = 0, \\ s_2 &= s_3 = s_{10} = s_{11} = s_{12} = s_{13} = s_{14} = s_{15} = s_{16} = 1/\tau, \\ s_5 &= s_7 = s_9 = s_{17} = s_{18} = s_{19} = 8(2 - s_2) / (8 - s_2). \end{aligned} \tag{3.17}$$

The main relaxation time was set to $\tau = 0.6$ following the work of Ref. [69] on the permeability of Fontainebleau sandstones. The no-slip fluid-solid boundary condition was simulated by applying the standard bounce-back rule. The pressure gradient driving the fluid was simulated with an external force acting on all fluid nodes. The acceleration in equation 3.14 was set to $\mathbf{g} = g\mathbf{e}_x$ where the acceleration value, g , was set to 10^{-5} . Periodic boundary conditions were

used in the three spatial directions in order to minimize boundary effects. The algorithm was implemented in MATLAB and parallelized using Jacket [72] GPU engines. The algorithm is capable of running on any computer equipped with a CUDA-enabled GPU. The system that was used to run the simulations comprised an NVIDIA GeForce GTX 460M with 192 CUDA cores running at 1.36 GHz and 1.5 GB of memory. Using Jacket, a speedup of ~ 16 was achieved for typical systems with one million nodes (execution time on CPU without Jacket / execution time on GPU with Jacket).

3.1.6 Methods for calculating permeability

The intrinsic permeability is related to macroscopic observables through Darcy's law [5] as previously shown in equation 2.1. In the lattice Boltzmann simulations, when a constant body-force is applied throughout the sample, it is not necessary to calculate the pressure gradient as its value is simply given by g [73]. Consequently, the intrinsic permeability can be calculated with:

$$\kappa = \frac{\langle u_x \rangle \mu}{g} \quad (3.18)$$

and is expressed in units of Δx^2 . In the simulations, the intrinsic permeability was calculated when the simulations were considered to be converged, that is, when the mean velocity change per voxel per time step averaged over 100 time steps was smaller than 10^{-8} .

3.1.7 Validation

Analytical solutions exist for flows in a number of relatively simple geometries. In these few cases, the accuracy of the implemented model can be tested by comparing the simulation results with analytical solutions. Accordingly, the relative error in permeability is defined as the relative error between the simulated and the analytical value:

$$\varepsilon = \frac{\kappa^{LB} - \kappa^{analytical}}{\kappa^{analytical}}. \quad (3.19)$$

Flow in square pipes

To validate the implemented LB model, the flow was computed in an infinitely long 3D square pipe of side length h . The permeability of the square pipe can be calculated analytically by assuming a laminar flow and is given by [74]:

$$\kappa^{analytical} = \frac{h^2}{4} \left[\frac{1}{3} - \frac{64}{\pi^5} \sum_{i=0}^{\infty} \frac{\tanh\left((2i+1)\frac{\pi}{2}\right)}{(2i+1)^5} \right] \approx 0.03514h^2. \quad (3.20)$$

Figure 3.3 shows that the relative error in permeability decreases from 36% for $h = 1$, to 1.4% for $h = 10$ and to less than 0.1% for $h = 40$.

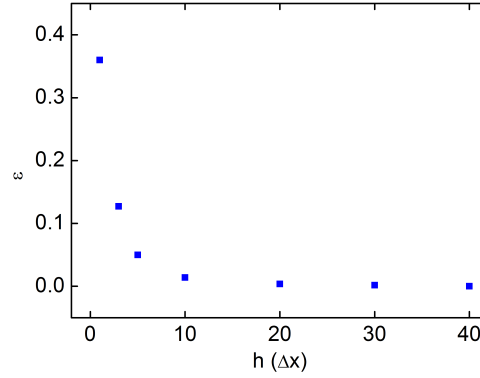


Figure 3.3: Relative error in permeability ε vs. the side length h of a 3D infinitely long square pipe.

Flow through a cubic array of overlapping spheres

The accuracy of the model in a more complicated geometry was tested by computing the flow through a cubic array of overlapping impermeable spheres of radius r and centre-to-centre spacing L . Figure 3.4 shows an illustration of a single simulation unit cell and of the overall resulting medium when periodic boundary conditions are used.

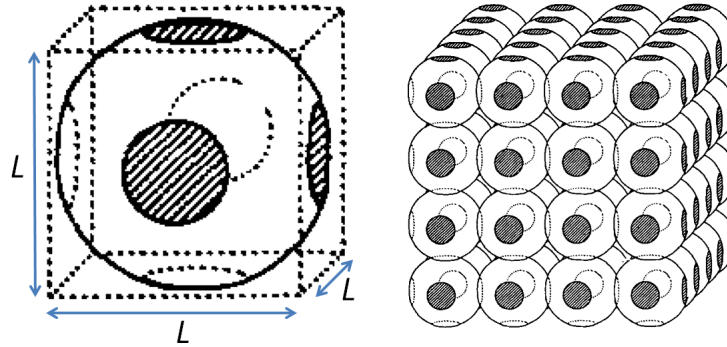


Figure 3.4: (left) Schematic illustration of a simulation unit cell consisting of a sphere centred in a cubic lattice of side length L . (right) The resulting medium when periodic boundary conditions are used and the spheres are allowed to overlap. Figures are adapted from [75].

The analytical permeability is given by:

$$\kappa^{analytical} = \frac{1}{6\pi C_D} \frac{L^3}{r} \quad (3.21)$$

where C_D is the porosity dependent drag force coefficient as described in [75].

First, the size of the system L (*i.e.* number of pixels used to discretize the side length of the cube) was varied while keeping the porosity constant at circa 20%. The analytical and

numerical permeabilities and the relative error in permeability are shown in figure 3.5. Second, the radius of the sphere, and consequently the porosity, were varied while keeping the size of the system constant at a relatively coarse resolution of $L^3 = 21^3$. The relative error in permeability is shown in figure 3.6.

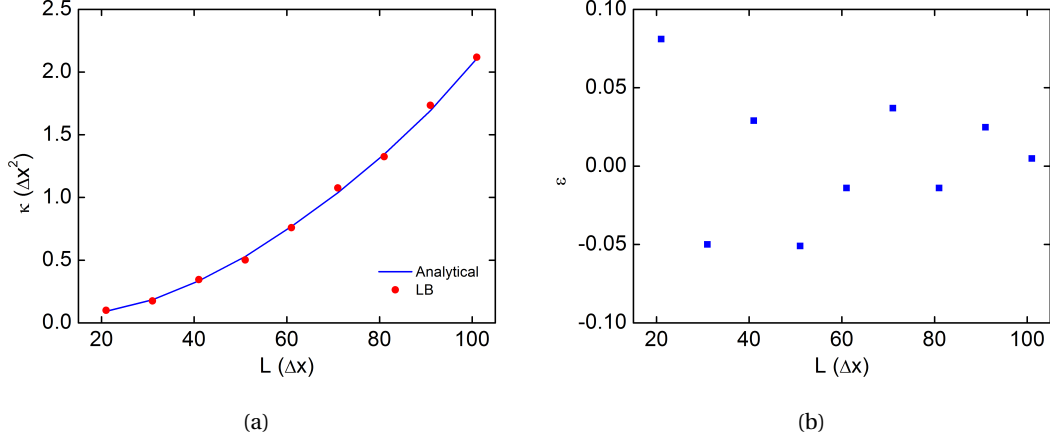


Figure 3.5: (a) Analytical and numerical permeabilities κ and (b) relative error in permeability ε vs. the size L of a system of overlapping spheres with 20% porosity.

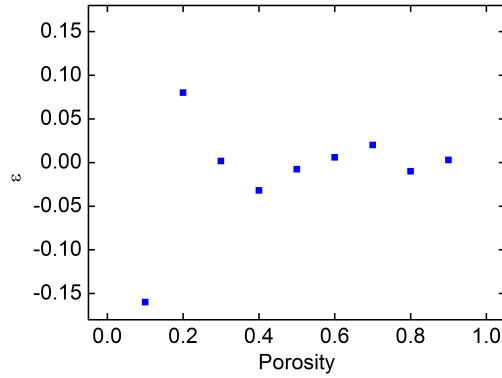


Figure 3.6: Relative error in permeability ε vs. the porosity of a system of overlapping spheres of size $L^3 = 21^3$.

With increasing resolution (figure 3.5) or increasing porosity (figure 3.6), the relative error in permeability ε decreases and the simulated permeability converges to the analytical prediction. However, in both cases, the error does not decrease monotonically, presumably due to the discretization of the spheres as has been previously observed by Manwart *et al.* [76].

Additionally, the permeability of the system of overlapping spheres was computed for several values of the kinematic fluid viscosity. This was achieved by varying the relaxation time τ between 0.6 and 2.0. The permeability shows a negligible dependence on the viscosity, a

clear advantage of the multi-relaxation-time collision operator [64] when compared to the single-relaxation-time collision operator (figure 3.7).

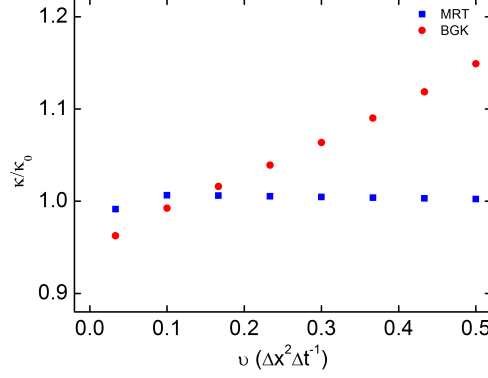


Figure 3.7: Normalized permeability κ/κ_0 for a system of overlapping spheres *vs.* the kinematic viscosity ν obtained using a multi- and a single- relaxation times collision operators. The size of the system is $L^3 = 32^3$ and the porosity is 85.1%.

In all the validation tests described above, a very good agreement was observed between numerical and analytical results. This suggests that the implemented algorithm can be trusted to compute the flow in more complex geometries where analytical solutions cannot be found.

3.2 Effective media methods for the transport properties

3.2.1 Overview

In general, in *effective* media approaches, a multi-scale problem is addressed by assigning effective macro-scale properties (*e.g.* permeability) to appropriate numerical nodes. A good example is the Brinkman equation [77] which is an extension of Darcy's law that accounts for fluid flow through porous solids:

$$\beta \nabla^2 J + J = \frac{A}{L_0} \kappa \Delta P \quad (3.22)$$

where β is an effective viscosity term. Effective media approaches are capable of extending the use of standard numerical methods to include larger media or media with partly unknown geometries (*e.g.* C-S-H). There are two main classes of lattice Boltzmann solvers that incorporate effective media: force-adjusted and partial bounce-back methods.

Force-adjusted methods

Originally, Spaid and Phelan [78] proposed a two-dimensional model to recover the Brinkman equation by modifying the velocity term in the LB equilibrium functions to reduce the magni-

tude of the momentum. The idea behind this approach is to use the Stokes equation to model the flow in open regions, and the Brinkman equation to model the flow through porous structures by treating them as an effective medium of known permeability. The main drawback of this approach is its inability to model objects with very low permeability. Freed [79] improved the method by allowing it to recover flow through a resistance field with a higher momentum sink. Martys [80] extended the validity of the LB Stokes-Brinkman approach over a larger range of forcing and “porous media effective viscosity” by incorporating the dissipative forcing into a linear body-force. Martys and Hagedorn [81] applied this model to study the effect of the permeability of sand grains on the bulk permeability of a Fontainebleau sandstone. Unsurprisingly, they found that the bulk permeability increases with the sand grain permeability at low porosities, and that, at high porosities, the bulk permeability is insensitive to the sand grain permeability. They pointed out that their algorithm was unstable when the sand permeability was low, less than order* $\sim 0.1\Delta x^2$. Kang *et al.* [7] combined the Stokes-Brinkman LB model with a non-uniform mesh to study the effect of simplified 2D fractures on the permeability of rocks. They reported that the importance of the flow in the porous matrix depends on the ratio of the permeability of the porous matrix to that of the fracture.

Partial bounce-back methods

In a different approach based on earlier work done by Balasubramanian *et al.* [82] and Gao and Sharma [83] on lattice gases, Dardis and McCloskey [84, 85] proposed a lattice Boltzmann method where momentum loss is due to the “presence of solid obstacles”. The “solid scatterer density”, or more simply the “solid fraction”, is related to the permeability of the porous medium that they represent. They reported a behaviour consistent with a Kozeny-Carman [86, 87] type relationship between the solid fraction and the permeability for low to intermediate solid fractions. They noted that at intermediate to high solid fractions, the rapid decrease in permeability is consistent with a percolation process giving a power-law relationship between the solid fraction and the permeability. However, their use of a two-dimensional hexagonal lattice made it impossible to calculate the permeability of porous media with high solid fractions and thus low permeabilities. Thorne and Sukop [88, 89] developed an algorithm where the additional “porous media step” takes place after the traditional collision step and used it on a $D2Q9$ lattice to model the Elder problem where the fluid flow is initiated by density variations. Chen and Zhu [90] analysed the Gao and Sharma [83], Dardis and McCloskey [84] and Thorne and Sukop [88] models. They showed that only the Thorne and Sukop model is valid for the whole range of solid fractions (zero to one). They also showed that these models yielded velocity profiles in good agreement with Brinkman’s predictions. Walsh *et al.* [91] proposed a new “pre-collision” partial bounce-back algorithm and derived an analytical expression that links the permeability to the “solid fraction”. They showed that their model [91] and the models of Dardis and McCloskey [84] and Thorne and Sukop [88] produce equivalent results although their own has significant advantages in terms of mass conservation in heterogeneous media and suitability for parallel computing. Recently, Zhu

* In general, Δx is on the order of 10^{-7} to 10^{-5} m in porous media.

and Ma [92] proposed a new partial bounce-back algorithm and showed how both their model and the Walsh *et al.* [91] model recover similar forms of the Brinkman equation.

3.2.2 Theory

For simplicity and without loss of generality, the Walsh *et al.* model [91] is demonstrated on the single-relaxation-time collision operator with $\Delta x, \Delta t$ and τ set to unity. In this case, and in the absence of external forces, equation 3.2 is reduced to:

$$f_i(\mathbf{r} + \mathbf{e}_i, t + 1) = f_i^{eq}(\mathbf{r}, t). \quad (3.23)$$

In the partial bounce-back method, the fluid – fluid collision and the bounce-back rules are combined to reflect local material properties (figure 3.8). To control the partial bounce-back

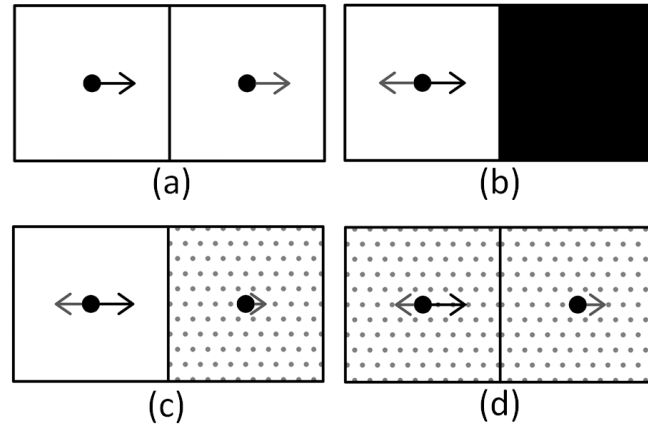


Figure 3.8: A 1D schematic showing one distribution function for (a) propagation between fluid nodes, (b) full bounce-back at a fluid-solid interface, (c) propagation and partial bounce-back between a fluid and a weakly-permeable grey node and (d) propagation and partial bounce-back between two weakly-permeable grey nodes. Pores are shown in white, solids in black and weakly-permeable grey nodes in dotted grey. Black arrows stand for the distribution function at time t and grey arrows for the distribution function at time $t+1$.

step, an effective media parameter $\sigma(\mathbf{r})$ is introduced [91] which combines equation 3.23 with the bounce-back step as described in equation 3.13. The master equation of the algorithm becomes:

$$f_i(\mathbf{r} + \mathbf{e}_i, t + 1) = [1 - \sigma(\mathbf{r})] f_i^{eq}(\mathbf{r}, t) + \sigma(\mathbf{r}) f_{\bar{i}}(\mathbf{r}, t). \quad (3.24)$$

Equation 3.24 recovers equation 3.23 in pores ($\sigma(\mathbf{r}) = 0$) and equation 3.13 in the case of solid boundaries ($\sigma(\mathbf{r}) = 1$). The “effective media parameter” $\sigma(\mathbf{r})$ is equivalent to the “density of solid scatterers” or “solid fraction” previously used by other authors [84, 88, 91, 92]. The term “effective media parameter” is preferred in this work in order to avoid unnecessary confusion with the intrinsic porosity or density. Hence, a weakly-permeable node with defined effective

media properties is labelled a grey node. Accordingly, the following classes of nodes are defined:

$$\begin{aligned}\sigma(\mathbf{r}) = 0 &: && \text{pores} \\ 0 < \sigma(\mathbf{r}) < 1 &: && \text{grey nodes} \\ \sigma(\mathbf{r}) = 1 &: && \text{solids}\end{aligned}\tag{3.25}$$

The microscopic and macroscopic density and momentum are given by:

$$\rho^*(\mathbf{r}, t) = \sum_{i=1}^Q f_i(\mathbf{r}, t)\tag{3.26}$$

$$\rho(\mathbf{r}, t) = [1 - \sigma(\mathbf{r})] \sum_{i=1}^Q f_i(\mathbf{r}, t)\tag{3.27}$$

$$\rho^*(\mathbf{r}, t) \mathbf{u}^*(\mathbf{r}, t) = \sum_{i=1}^Q f_i(\mathbf{r}, t) \mathbf{e}_i\tag{3.28}$$

$$\rho(\mathbf{r}, t) \mathbf{u}(\mathbf{r}, t) = [1 - \sigma(\mathbf{r})] \sum_{i=1}^Q f_i(\mathbf{r}, t) \mathbf{e}_i\tag{3.29}$$

where the asterix signifies a microscopic variable used for the calculation of the equilibrium functions. For $\sigma(\mathbf{r}) = 0$, equations 3.27 and 3.29 recover equations 3.26 and 3.28, respectively while for $\sigma(\mathbf{r}) = 1$ they are both equal to zero.

At the start of each simulation, the nodes are initialized to a microscopic density according to:

$$\rho^*(\mathbf{r}, t = 0) = \begin{cases} 0 & \text{for solids} \\ 1 & \text{for grey nodes,} \\ 1 & \text{for pores} \end{cases}\tag{3.30}$$

zero microscopic velocity:

$$\mathbf{u}^*(\mathbf{r}, t = 0) = 0,\tag{3.31}$$

and the macroscopic moments are calculated with equations 3.27 and 3.29.

Walsh *et al.* [91] derived the intrinsic permeability of grey nodes (partially-permeable homogeneous media for which $\sigma(\mathbf{r}) = \sigma \forall \mathbf{r}$) as a function of the fluid kinematic viscosity and the effective media parameter as:

$$\kappa(\mathbf{r}) = \frac{1 - \sigma(\mathbf{r})}{2\sigma(\mathbf{r})} v.\tag{3.32}$$

Equation 3.32 was derived by projecting the $D3Q19$ lattice onto a $D1Q3$ lattice and assuming a stationary fluid as shown in Appendix C. For low values of the effective media parameter σ , a similar equation, $\kappa = v/2\sigma$, was obtained by Balasubramanian *et al.* [82] by introducing a damping term proportional to the velocity in the Navier-Stokes equation.

3.2.3 Implementation

The model as described above in equation 3.24 was first proposed and implemented by Walsh *et al.* in 2D [91]. What follows is believed to be the first 3D implementation. A three-dimensional version is necessary for porous media because the percolation is critically dependent on the number of spatial dimensions. This implementation will highlight some ambiguities within [91], demonstrate the ability of the model in a number of relatively complex geometries, and compare the numerical results with analytical predictions whenever possible.

Walsh *et al.* use the term “solid fraction”. In this work, the term “effective media parameter” is preferred in order to avoid any unnecessary confusion with the inherent porosity or density of the grey nodes.

Walsh *et al.* tested the model on homogeneous materials composed of grey nodes only. Although Walsh and Saar [93] subsequently studied the 2D speleogenesis of carbonate aquifers with a wide range of permeabilities, it was an application and not a validation and hence it did not clarify the implementation method. The setups used by Walsh *et al.* [91] are insufficient to reveal errors or inconsistencies in the definition of the hydrodynamic moments. This became clear as soon as inhomogeneous materials with pores, grey nodes and solids were tested.

This is the reason why Zhu and Ma [92] recently claimed that, in the Walsh *et al.* model, the velocity appears to be “discontinuous” at the interfaces between grey nodes with different permeabilities. However, equations 3.24 - 3.31 show, clearly, how to implement the model and initialize the variables. Section 3.2.5 demonstrates the accuracy of the model in a wide range of test setups. Additionally, section 3.2.5 shows that the “discontinuities” reported by Zhu and Ma are not a property or a limitation of the Walsh *et al.* model. Rather, they are most probably due to an inconsistency in the implementation of the Walsh *et al.* model by Zhu and Ma.

As part of this work, an effective media lattice Boltzmann model was implemented to simulate the permeation of isothermal fluids in saturated porous media. The equilibrium distribution functions were defined with equation 3.11 to model an incompressible isothermal fluid. The single-relaxation-time was preferred to the multi-relaxation-time collision operator to minimize the number of parameters while developing the model. For numerical efficiency, the relaxation time was set to $\tau = 1$. The no-slip fluid-solid boundary condition was taken into account in an implicit way in equation 3.24 on solid boundaries marked with $\sigma(\mathbf{r}) = 1$. The pressure gradient driving the fluid was simulated with pressure boundary conditions acting inside injection chambers as further discussed below. Periodic boundary conditions were used in the two remaining spatial directions in order to minimize boundary effects. Finally, the effective media algorithm was written in C and parallelized using the OpenMP library.

3.2.4 Methods for calculating permeability

The calculation of the intrinsic permeability was previously described in section 3.1 when a constant body-force was applied throughout the sample. However, when pressure boundary conditions are used, several additional parameters need to be defined. The critical ones are described in this section.

The simulations were carried out on samples of size $L_x \times L_y \times L_z$. The pressure boundary conditions were setup in the x direction. Accordingly, five-node-wide inlet and outlet chambers were added on the left and right hand sides of the sample. Therefore, the total system, composed of inlet, sample and outlet, has nodes located at $(l_x, l_y, l_z) = (1, 1, 1) \dots (L_x + 10, L_y, L_z)$ as illustrated in figure 3.9. The pressures were fixed on the first layer of the inlet ($P = P_{inlet}, l_x = 1$) and the last layer of the outlet ($P = P_{outlet} < P_{inlet}, l_x = L_x + 10$) following the description of Hecht and Harting [71] by setting the densities to ρ_{inlet} and $\rho_{outlet} < \rho_{inlet}$, the velocities to $u_y = u_z = 0$ and then solving for u_x . For more information see Appendix B.

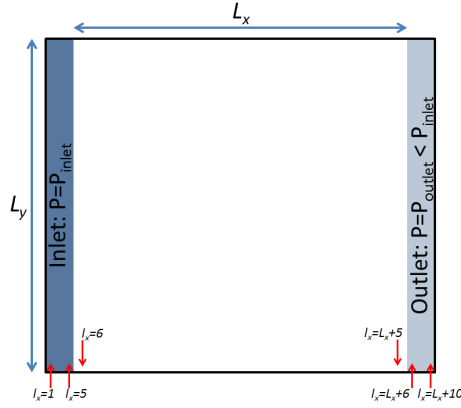


Figure 3.9: A 2D illustration of the setup used to impose pressure boundary conditions and calculate permeability.

The pressure gradient was approximated by the arithmetic mean of the pressures at the first surface layer ($l_x = 5, l_x = 6$) and last surface layer ($l_x = L_x + 5, l_x = L_x + 6$) of the sample as described by Narváez *et al.* [69]. The permeability was calculated with equation 2.1 when the simulations were considered to be converged, that is, when the relative permeability change per 1000 time steps was less than 10^{-5} .

3.2.5 Validation

In this section, the implemented algorithm is validated by comparing the numerical results with analytical predictions for a suite of standard test cases including flows in square pipes, flows through arrays of overlapping impermeable spheres, and flows through homogenous media with effective transport properties. In these cases, the relative error in permeability is calculated using equation 3.19. For some additional test cases, analytical solutions do not

exist and the results are discussed qualitatively.

Recovery of the standard lattice Boltzmann algorithm

Flow in square pipes First, to verify that the effective media algorithm recovered the standard lattice Boltzmann model behaviour, the flow was computed in a 3D infinitely long square pipe of side length h . The effective media parameter was set to $\sigma(\mathbf{r}) = 0$ for the fluid pores and to $\sigma(\mathbf{r}) = 1$ for the solid walls. The analytical permeability is given by equation 3.20. The relative error in permeability of the resultant Poiseuille flow decreases from 13 to 1% when the side length of the pipe increases from 3 to 7 nodes (figure 3.10). Figure 3.11 shows that the relative error is slightly different than that obtained using the standard LB algorithm of section 3.1. The small difference arises from the fact that the present algorithm uses an SRT collision operator with pressure boundary conditions while the algorithm developed in section 3.1 uses an MRT collision operator with an external body-force.

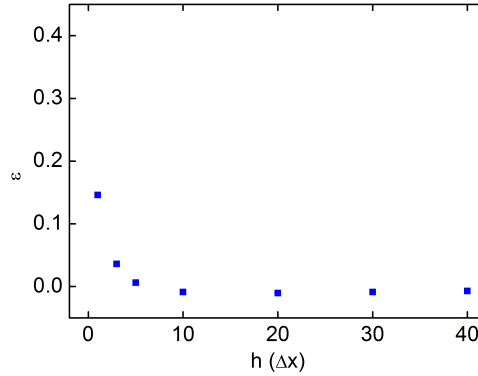


Figure 3.10: Relative error in permeability ϵ vs. the side length h of a 3D infinitely long square pipe.

Flow through a cubic array of overlapping spheres The accuracy of the model in a more complicated geometry was tested by computing the flow through a cubic array of overlapping spheres of radius r and centre-to-centre spacing L as previously illustrated in figure 3.4. First, the effective media parameter was set to $\sigma(\mathbf{r}) = 0$ for the pores and $\sigma(\mathbf{r}) = 1$ for the spheres. This makes the spheres impermeable and replicates the media studied in section 3.1. The size of the system was varied while keeping the porosity constant at circa 20%. The analytical permeability is given by equation 3.21. The analytical and numerical permeabilities and the relative error in permeability are shown in figure 3.12. There is a very good agreement. With increasing resolution, the error decreases and the calculated permeability converges to the analytical value. Moreover, the numerical error is comparable to that previously obtained using conventional finite difference schemes [76] and lattice Boltzmann solvers with single [76] and multiple (this work, section 3.1, figure 3.13) relaxation times collision operators.

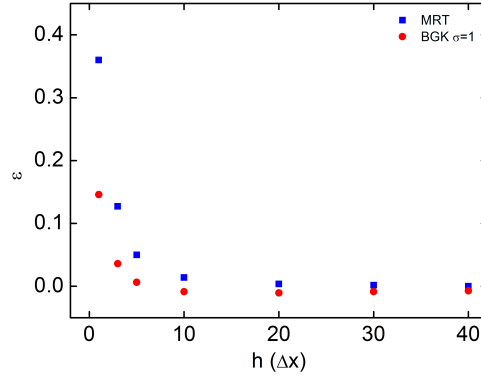


Figure 3.11: Relative error in permeability ε vs. the side length h of a 3D infinitely long square pipe as obtained with (1) a standard algorithm with an MRT collision operator and an external body-force and (2) an effective media algorithm with an SRT collision operator and pressure boundary conditions.

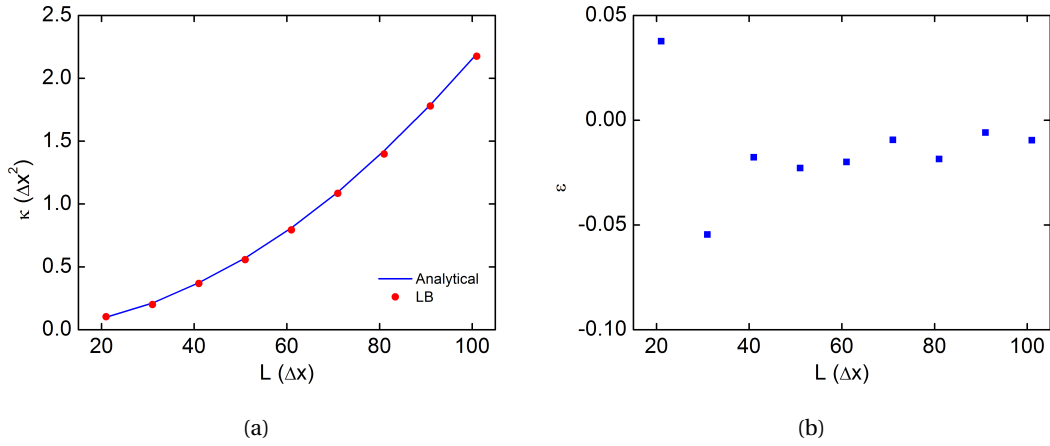


Figure 3.12: (a) Analytical and numerical permeabilities κ and (b) relative error in permeability ε vs. the size L of a system of overlapping spheres with 20% porosity.

We note, however, as for the results obtained using the MRT collision operator, the error does not decrease monotonically, presumably due to the discretization of the spheres as previously observed in section 3.1 and in [76].

Effective media algorithm

Homogeneous media To validate the partial bounce-back algorithm, the permeability of a medium of size $L^3 = 10^3$ uniformly filled with grey nodes of effective media parameter $\sigma(\mathbf{r}) = \sigma \forall \mathbf{r}$ was calculated as a function of σ . Figure 3.14 compares the simulation results to analytical predictions (equation 3.32). The relative error in permeability ε is smaller than

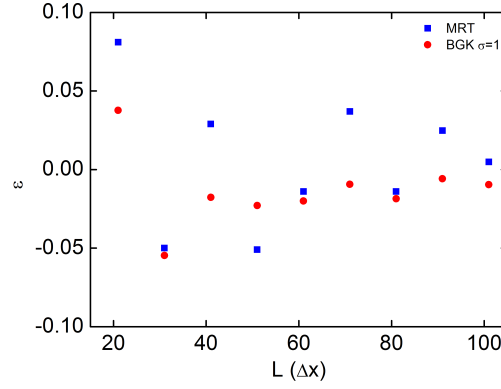


Figure 3.13: Relative error in permeability ε vs. the size L of a system of overlapping spheres as obtained with (1) a standard algorithm with an MRT collision operator and an external body-force and (2) an effective media algorithm with an SRT collision operator and pressure boundary conditions.

1% for homogeneous media with permeability $\kappa > 8.10^{-7} \Delta x^2$ and on the order of 5% for $\kappa > 8.10^{-17} \Delta x^2$.

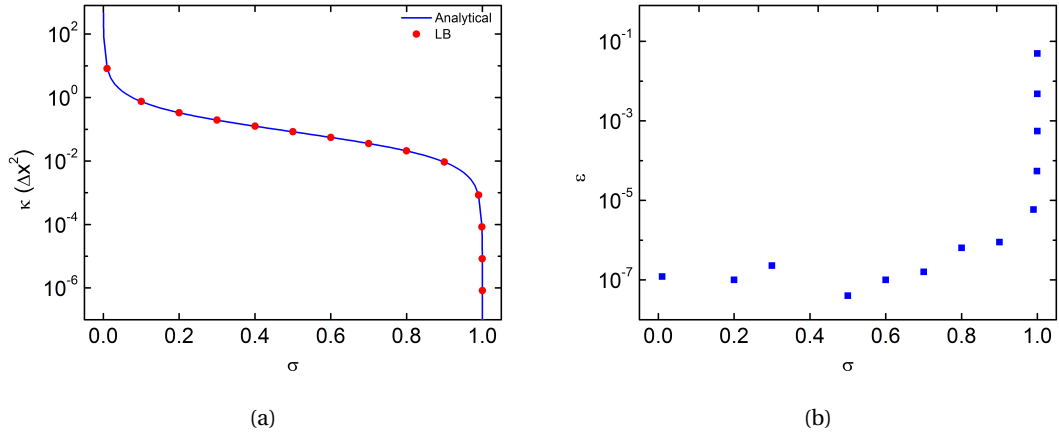


Figure 3.14: (a) Analytical and numerical permeabilities κ and (b) relative error in permeability vs. the effective media parameter σ of a 3D homogeneous system filled with grey nodes. In (b), the relative error for $\sigma = 0.1$ and $\sigma = 0.4$ is smaller than 10^{-8} .

The permeability results are in excellent agreement with the corresponding two-dimensional simulations performed by Walsh *et al.* [91] since, for homogeneous media, the number of spatial dimensions does not matter because $\sigma(\mathbf{r}) = \sigma \forall \mathbf{r}$. Indeed, it is worth noting that one of the methods that can be used to derive equation 3.32 starts by projecting the 3D lattice onto a 1D lattice (see appendix C and appendix A of [91]).

The case of $\sigma = 0.5$ is a special case and may be interpreted as a checkerboard structure with

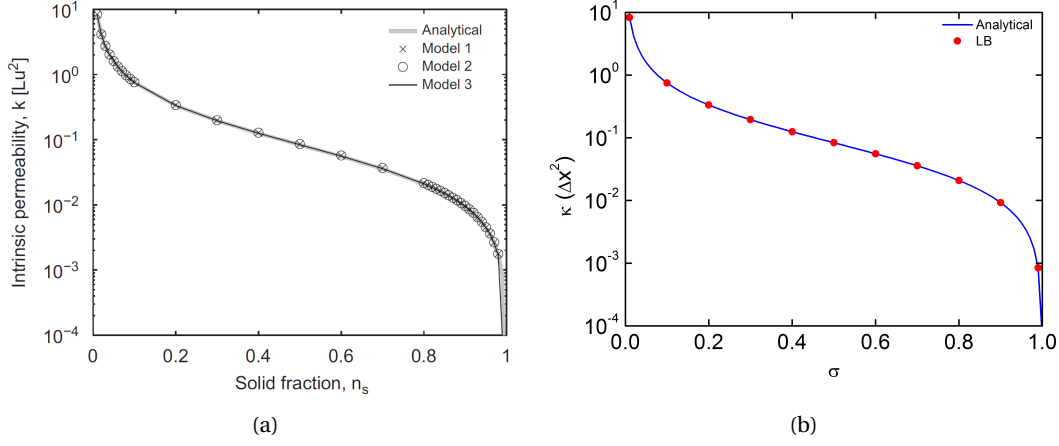


Figure 3.15: A comparison of results from literature with the results obtained in this work and previously shown in figure 3.14. (a) Analytical and numerical permeabilities κ vs. the “solid fraction” n_s of a 2D homogeneous system filled with grey nodes. The analytical results are obtained with equation 3.32. Model 1 is the extension of the Dardis and McCloskey [84] model to a $D2Q9$ lattice. Model 2 is the model proposed by Thorne and Sukop [88]. Model 3 is the model proposed by Walsh *et al.* [91]. Figure adapted from [91]. (b) Reproduction of the results of this work, as previously shown in figure 3.14, for the range of σ investigated by Walsh *et al.* [91] and shown in part (a) of this figure.

50% impermeable solids and 50% pores. Indeed, the permeability of a checkerboard structure equals the permeability of a homogeneous medium for which $\sigma(\mathbf{r}) = 0.5 \forall \mathbf{r}$. In this case, $\kappa_{\text{checkerboard}} = \kappa_{\sigma=0.5} = 0.0833\Delta x^2$. Additionally, the pressure drop is found to be linear inside homogenous samples with a coefficient of determination of $R^2 > 0.99$ (figure 3.16).

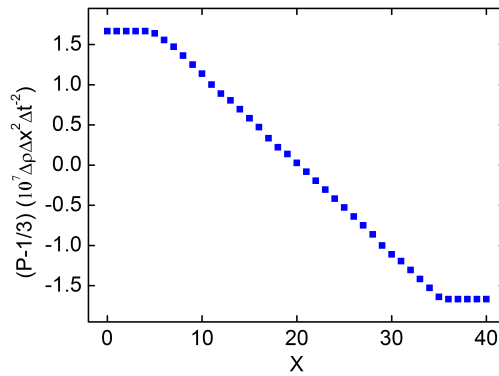


Figure 3.16: Pressure drop across a homogenous medium filled with grey nodes. The first and last five layers correspond to the inlet and outlet, respectively.

Flow through a cubic array of permeable overlapping spheres To investigate the effect of the permeability of the spheres on the overall permeability of the system of overlapping spheres, the effective media parameter of the spheres was varied from $\sigma(\mathbf{r}) = 1$ to $\sigma(\mathbf{r}) = 0.1$. This increases the intrinsic permeability of the spheres from zero to $0.75\Delta x^2$. Figure 3.17 shows the permeability of the system as a function of the effective media parameter and the permeability of the spheres. As expected, the permeability of the system increases with the permeability of the spheres.

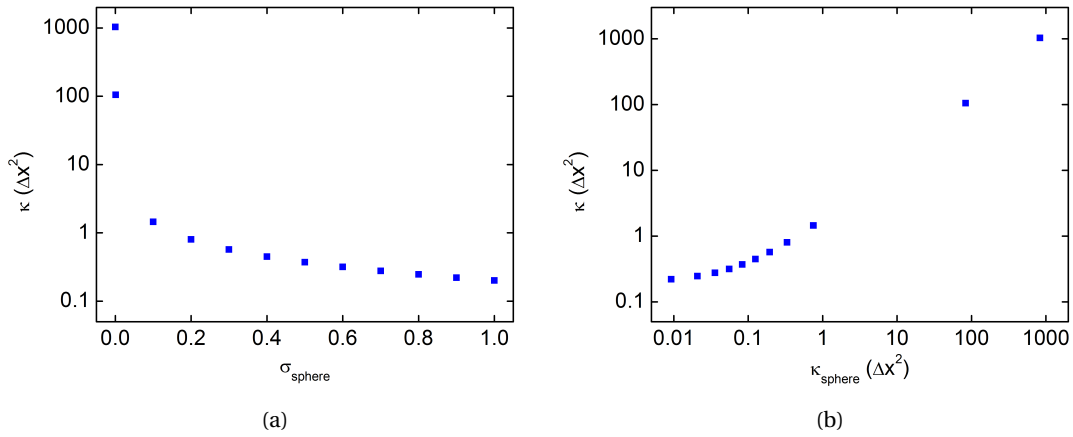


Figure 3.17: Permeability κ of a system of permeable overlapping spheres *vs.* (a) the effective media parameter of the spheres σ_{spheres} and (b) the permeability of the spheres κ_{spheres} . The size of the system is $L^3 = 31^3$ and the porosity is 20.7%.

Clips of the velocity in the flow direction are shown in figure 3.18 for multiple configurations. In all cases, the size of the system is $L^3 = 51^3$ and the porosity is 66.4%. The remaining volume, 33.6%, is filled with nodes of effective media parameters $\sigma_{\text{sphere}} = [1.0, 0.012, 0.005, 0.001]$. As expected, for an impermeable solid sphere ($\sigma_{\text{sphere}} = 1$), the flow goes around the sphere through the pores located at the corners of the sample. As the effective media parameter of the sphere is decreased ($\sigma_{\text{sphere}} = 0.012 - 0.001$), the intrinsic permeability of the grey nodes of the sphere increases, and consequently an increasing fraction of the flow goes through the sphere. At even lower effective media parameters, the sphere stops behaving like an obstacle to the flow and the flow becomes homogeneous in the sample.

Layered media In this section, the permeability of structures built from layers of different permeability materials is calculated (figure 3.19). Analytical expressions may be derived by analogy with the resistance of parallel and series networks of electrical resistors. In the simplified case where the structure is formed of two equal layers of permeability κ_1 and κ_2 , the equivalent permeabilities for the parallel and series configurations are:

$$\kappa_{\text{parallel}} = \frac{\kappa_1 + \kappa_2}{2} \quad (3.33)$$

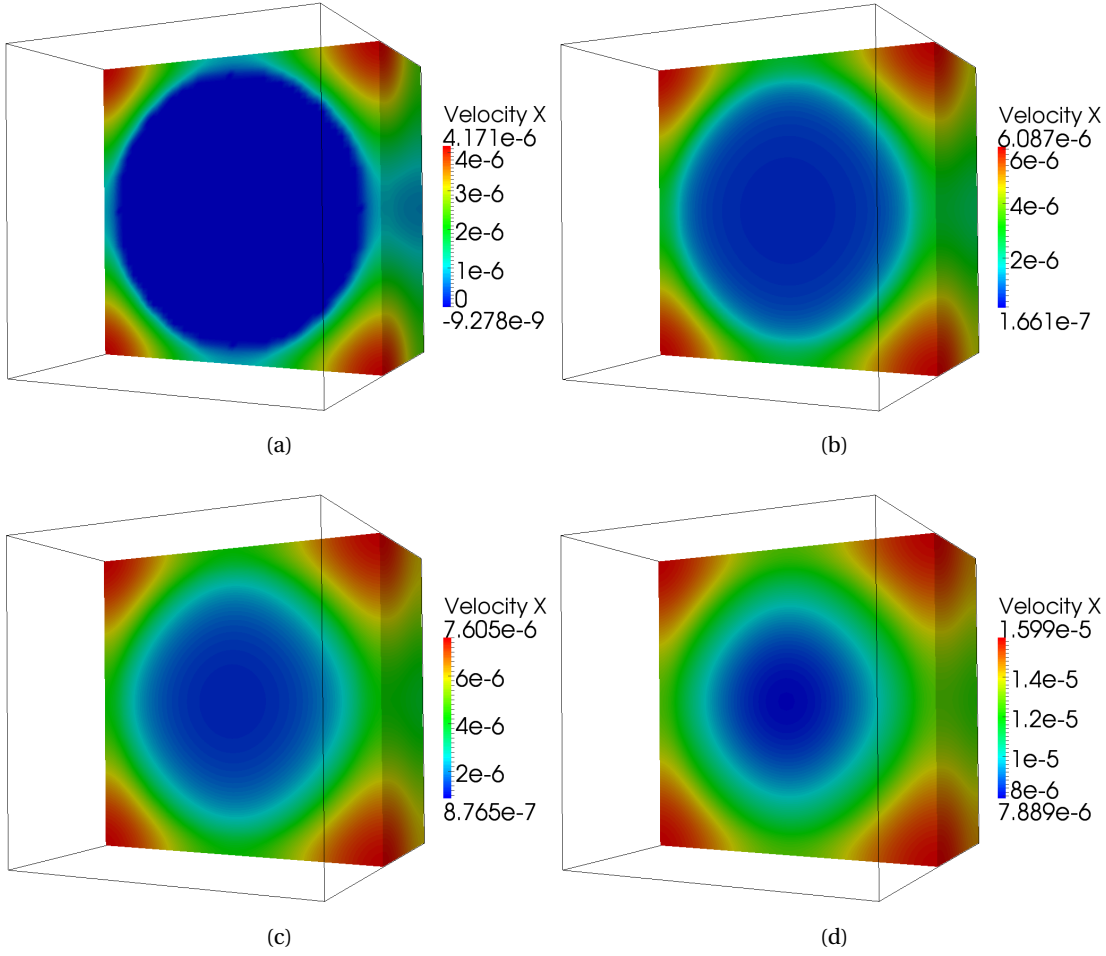


Figure 3.18: Clips of the velocity in the flow direction in a system of overlapping spheres where the effective media parameter of the sphere is (a) 1.0, (b) 0.012, (c) 0.005 and (d) 0.001. The size of the system is $L^3 = 51^3$ and the porosity is 66.4%.

and

$$\kappa_{series} = \frac{2\kappa_1\kappa_2}{\kappa_1 + \kappa_2}. \quad (3.34)$$

The equivalent permeabilities were computed while varying the configurations, the permeabilities, and the ratio between the permeabilities of the two layers. Table 3.1 shows the relative error in permeability for the various scenarios. The simulations and the analytical predictions are in excellent agreement for the series configurations and in good agreement for the parallel configurations. The larger error in the latter case is attributed to non-linearity of the pressure field.

3.2. Effective media methods for the transport properties

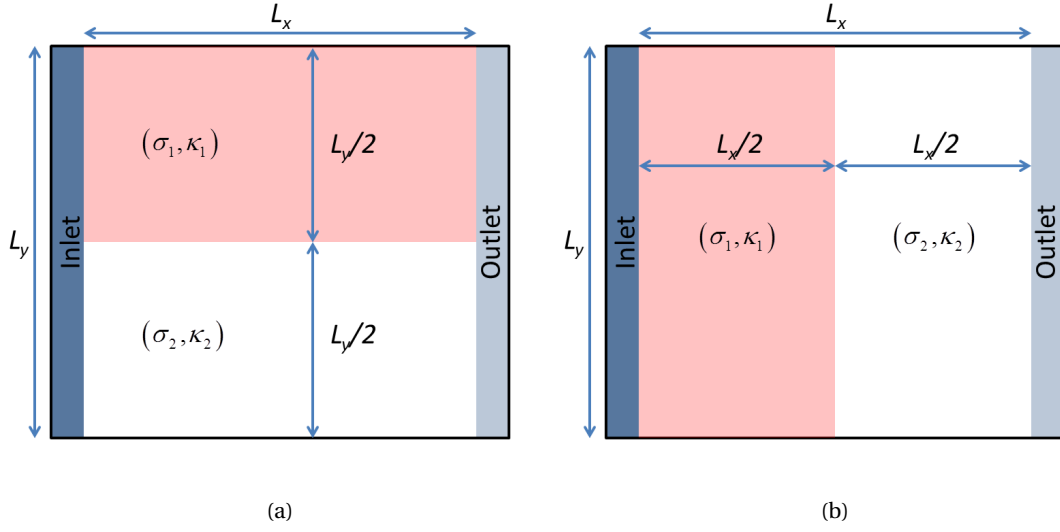


Figure 3.19: 2D schematic illustration of media composed of two equal layers and setup in (a) parallel and (b) serial configurations. The effective media parameters are (σ_1, σ_2) and the corresponding permeabilities (κ_1, κ_2) are calculated with equation 3.32.

Table 3.1: Relative error in permeability for structures built from layers of different effective media parameter.

$\sigma_1 - \sigma_2$	0.1–0.2	0.5–0.6	0.5–0.8	0.1–0.9	0.9–0.99	0.99–0.999
$\varepsilon_{parallel}$	-3.9×10^{-2}	-4.9×10^{-3}	-4.4×10^{-2}	-2.7×10^{-1}	-7.0×10^{-2}	-6.5×10^{-2}
ε_{series}	-3.4×10^{-2}	-1.8×10^{-2}	-5.2×10^{-2}	-8.1×10^{-2}	-6.4×10^{-6}	9.6×10^{-6}

Other tests The flow was computed inside a cubic sample of size $L^3 = 31^3$ composed of very low permeability grey nodes (σ_1, κ_1) surrounding a hollow sphere of effective media parameter σ_2 as shown in figure 3.20. Since the flow is conserved and $\kappa_{sphere} \gg \kappa_{sample}$, the pressure drop is not linear throughout the sample. Rather, as expected, an extremely small pressure drop was observed inside the sphere (figure 3.21).

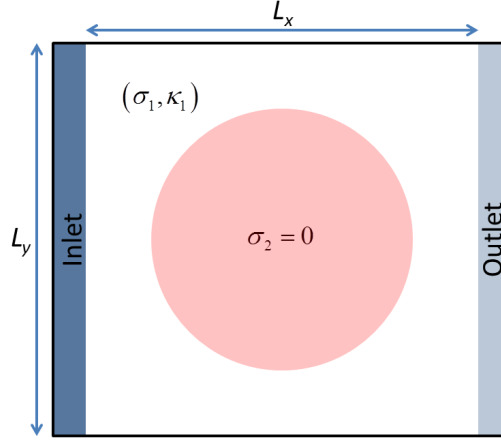


Figure 3.20: 2D schematic illustration of a medium composed of very low permeability grey node surrounding a hollow sphere.

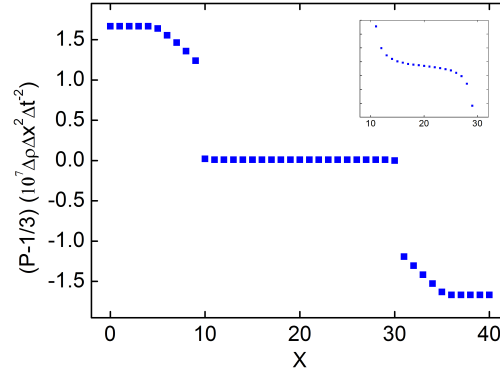


Figure 3.21: Pressure drop inside the medium described in the text and illustrated in figure 3.20.

Comment on Zhu and Ma findings on the discontinuity of the velocity In a recent paper, Zhu and Ma [92] compared their partial bounce-back model to their implementation of the Walsh *et al.* model [91]. In most of the test cases, they reported that the results obtained using both models matched closely. However, for one particular case labelled case 3, the authors reported that in the Walsh *et al.* model the “*velocity appear to be discontinuous at the two interfaces, an unphysical behaviour, whereas the velocity of the proposed model remains smooth*” (*sic*). In their case 3, as described in section 4.3 and figure 2 of [92], the flow is simulated “*along three layer strata of porous media, where the top and bottom layers are the same but different from the middle one*” and the three layers are sandwiched between solid walls in the directions parallel to the flow (figure 3.22).

The partial bounce-back algorithm as described in section 3.2 is a 3D implementation of the Walsh *et al.* model. It uses the same master equation of the Walsh *et al.* model implemented by

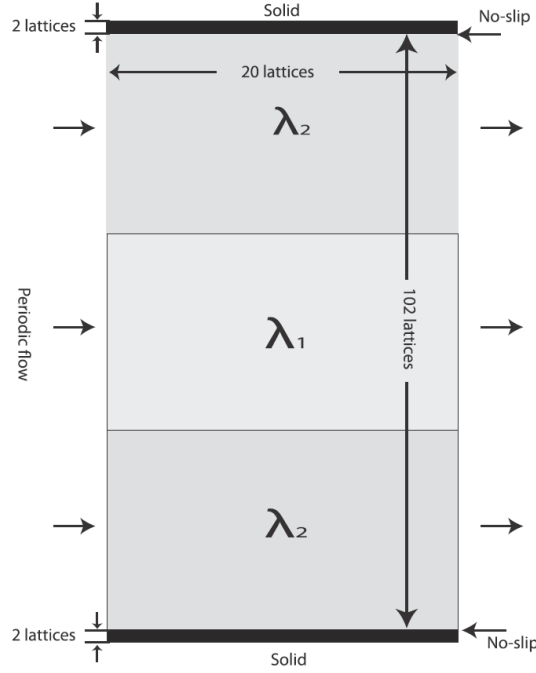


Figure 3.22: Schematic illustration of the test case 3 as described in [92]. The porous media model parameters λ are equivalent to the term σ used in this work. Figure adapted from [92].

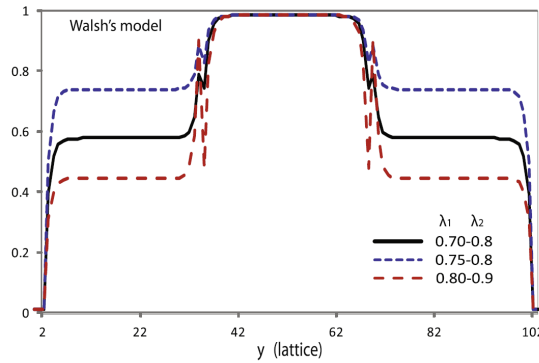


Figure 3.23: Normalized velocity profile along the y axis for test “case 3” as described in figure 3.22 and in section 4.3 of [92]. The porous media model parameters λ are equivalent to the term σ used in this work. Figure adapted from [92].

Zhu and Ma but employs (1) pressure boundary conditions acting inside injection chambers instead of forcing to drive the fluid and (2) a relaxation time $\tau = 1$ instead of $\tau = 2$. Using this implementation, the flow was computed for test case 3 of [92]. No discontinuity was observed in the velocity profile at the interfaces as reported in [92]. Furthermore, the implementation was modified in order to match the exact setup of Zhu and Ma by using a force to drive the fluid and a relaxation time of $\tau = 2$. The results are essentially the same. Figure 3.24 shows the normalized velocity profile in the direction of the flow along the y axis for the setup of

case 3. Clearly, using the 3D LB model implemented in this work, the velocity profile is smooth and displays no discontinuity as shown in figure 5 of [92] and figure 3.23. It is concluded that the discontinuity reported by Zhu and Ma is not a property or a limitation of the Walsh *et al.* model. Rather, it may be due to an artefact specific to the implementation of the Walsh *et al.* model by Zhu and Ma (e.g. initialization of the system, definitions of microscopic and macroscopic moments).

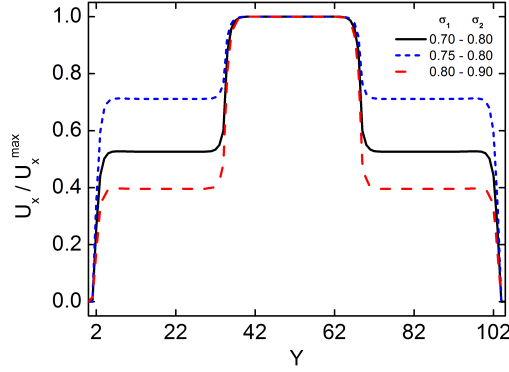


Figure 3.24: Normalized velocity profile along the y axis for test “case 3” as described in figure 3.22.

Finally, it is noted that in all tests, mass was conserved up to the numerical accuracy of the simulation. Moreover, in all the validation tests described above, a very good agreement was observed between numerical and analytical results. This suggests that the implemented algorithm can be trusted to compute the flow in more complex media composed of pores, grey nodes and solids.

4 Lattice Boltzmann Methods for non-Ideal Fluids

Contents

4.1 Standard methods	43
4.1.1 Overview	43
4.1.2 Free energy approach for non-ideal fluids	44
4.1.3 Wetting dynamics	46
4.1.4 Implementation	47
4.1.5 Methods for modelling adsorption and desorption	48
4.1.6 Validation	48
4.2 Effective media methods for the transport and wetting properties	60
4.2.1 Overview	60
4.2.2 Free energy approach for effective wetting properties	60
4.2.3 Implementation	61
4.2.4 Methods for modelling adsorption and desorption	61
4.2.5 Validation	61
4.2.6 Application to a 2D characteristic microstructure	65
4.2.7 Conclusions	69

4.1 Standard methods

4.1.1 Overview

Numerical simulation of *complex* non-ideal fluids is rather challenging. In addition to the theoretical framework that is required to describe the interactions between the multiple physical and chemical phases of the fluid, a numerical algorithm is needed to track the interfaces between the phases. The latter part usually requires unrealistic computational costs. Notwithstanding, lattice Boltzmann methods offer an implicit tracking of the interfaces. The creation,

movement and annihilation of interfaces are tracked *automatically*. Consequently, LB methods have been successful in simulating complex fluids for a wide variety of applications.

Three conceptually different algorithms have been developed to describe complex fluids: Gunstensen *et al.* [94] developed a color-fluid algorithm particularly adapted for strong phase separation, Shan and Chen [55] introduced an inter-particle potential that mimics microscopic interactions, and Swift *et al.* [56] implemented a pressure tensor to incorporate a free energy in the lattice Boltzmann algorithm. In the color-fluid model [94, 95], two fluids, typically labelled red and blue, are introduced and phase separation is achieved by a forcing particles to regions of the same colour. This model is particularly adapted for multi-fluid applications with strong phase separation such as is the case for oil and water. The inter-particle potential model of Shan and Chen [55] is based on the concept of interactions between nearest-neighbours. In this model, the equilibrium velocity is modified in order to include an interactive force that causes phase separation and creates surface tension. The main drawback is the dependency of both surface tension and equation of state on one single parameter. Recently, this problem was addressed by Sbragaglia *et al.* [96] by extending the inter-particle interactions to include the next-nearest-neighbours. While the two models described above are based on phenomenological descriptions of the interface and dynamics, the free-energy model of Swift *et al.* [56] uses equilibrium functions that can be defined more consistently, based on thermodynamics. This makes it possible to implement an equation of state that describes both liquid and gas phases, as well as their coexistence curve.

4.1.2 Free energy approach for non-ideal fluids

The equilibrium properties of a one-component non-ideal fluid with no solid surfaces can be described by a Landau free energy functional [56, 97, 98]:

$$\Psi = \int_V dV \left[\psi(T, \rho) + \frac{\chi}{2} (\partial_\alpha \rho)^2 \right]. \quad (4.1)$$

In this case, $\int_V dV \rho$ is the total mass of the fluid, $\psi(T, \rho)$ the free energy density of the bulk phase and T the temperature of the fluid. The second term of the RHS of equation 4.1 describes the liquid – vapour interfaces and χ is a constant related to the surface tension between the liquid and vapour phases.

This free energy can be incorporated in the lattice Boltzmann algorithm via the pressure tensor [99, 100]:

$$P_{\alpha\beta} = \left[p_0 - \chi \left(\rho \nabla^2 \rho + \frac{1}{2} |\nabla \rho|^2 \right) \right] \delta_{\alpha\beta} + \chi \partial_\alpha \rho \partial_\beta \rho \quad (4.2)$$

where p_0 is the equation of state of the fluid and the other terms, dependent on χ , describe the liquid – vapour interfaces. The symbols ∂_α , ∇ and ∇^2 refer to the derivative with regards to α , the gradient and the Laplacian operators, respectively. Summation over repeated indices is

assumed.

The pressure can be scaled by a factor ξ in order to improve the numerical stability of the system without affecting its equilibrium behaviour [100]. Equation 4.2 becomes:

$$P_{\alpha\beta} = \xi \left\{ \left[p_0 - \chi \left(\rho \nabla^2 \rho + \frac{1}{2} |\nabla \rho|^2 \right) \right] \delta_{\alpha\beta} + \chi \partial_\alpha \rho \partial_\beta \rho \right\}. \quad (4.3)$$

The water can be described by a van der Waals fluid in a limited range of (P, V) . The equation of state can be written under the form:

$$p_0 = \frac{RT}{V-b} - \frac{a}{V^2} \quad (4.4)$$

where p_0 is the bulk pressure, V the specific volume, T the temperature and R the universal gas constant. The constants a and b are dependent on the fluid. The volume term V can be substituted with the density $1/\rho$. This leads to:

$$p_0 = \frac{\rho T}{1 - \rho b} - a \rho^2. \quad (4.5)$$

Figure 4.1 shows a schematic illustration of the $P - V$ phase diagram of a van der Waals fluid. The phase separation occurs when the areas under (shown in yellow) and over (shown in green) the curve become equal. The densities of the liquid and vapour phases can be obtained from the corresponding volumes V_L and V_G .

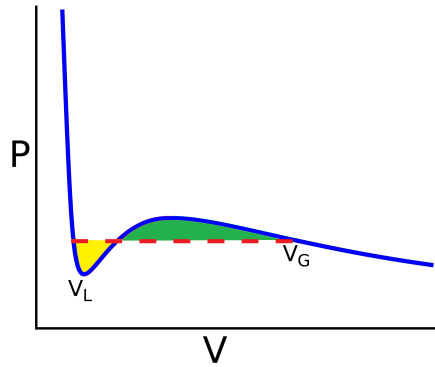


Figure 4.1: Schematic illustration of the phase diagram $P - V$ of a van der Waals fluid.

In reduced units, the equation of state becomes:

$$p_0 = \frac{\rho}{3 - \rho} - \frac{9}{8} \theta_c \rho^2 \quad (4.6)$$

where the temperature is $\theta = 1/3$ and the critical temperature is θ_c . The critical density ρ_c defines the liquid - vapour phase transition and is set to unity.

According to this model, and under the assumptions that $\Delta x = \Delta t = 1$, the equilibrium distri-

butions are [101]:

$$f_i^{eq}(\mathbf{r}, t) = \omega_i \left[\frac{\rho(\mathbf{e}_i \cdot \mathbf{u}) + \frac{3}{2}\rho(\mathbf{e}_i \cdot \mathbf{u})^2 - \frac{1}{2}\rho(\mathbf{u} \cdot \mathbf{u}) + \frac{3}{2}\lambda[2(\mathbf{e}_i \cdot \mathbf{u})(\mathbf{e}_i \cdot \nabla \rho) + (\mathbf{e}_i \cdot \mathbf{e}_i - 1)(\mathbf{u} \cdot \nabla \rho)]}{\omega_i^p p_0 - \chi \left(\omega_i^t \rho \nabla^2 \rho + \sum_{\alpha=x,y,z} \omega_i^{\alpha\alpha} \partial_\alpha \rho \partial_\alpha \rho + \sum_{\alpha,\beta=x,y,z} \omega_i^{\alpha\beta} \partial_\alpha \rho \partial_\beta \rho \right)} \right] \quad (4.7)$$

where the stationary equilibrium distribution function is chosen in order to conserve mass:

$$f_1^{eq}(\mathbf{r}, t) = \rho(\mathbf{r}, t) - \sum_{i=2}^Q f_i^{eq}(\mathbf{r}, t). \quad (4.8)$$

The coefficients ω_i are the lattice weights. The term involving the parameter λ ensures Galilean invariance [102]:

$$\lambda = \left(\tau - \frac{1}{2} \right) \left(\frac{1}{3} - \frac{dp_0}{d\rho} \right). \quad (4.9)$$

The last line of equation 4.7 gives the contribution of the pressure tensor. The coefficients $\omega_i^{p,t,\alpha\alpha,\alpha\beta}$ are free adjustable parameters and can be found in [101].

It is worth noting that in addition to the macroscopic moments ρ and \mathbf{u} , the equilibrium functions require several derivative forms of the density. These operations make the computation of the equilibrium functions very expensive, especially when compared to the operations that are required to calculate the equilibrium functions of isothermal fluids (equation 3.11). Additional information about the numerical algorithms that are used to calculate the gradients in the bulk can be found in appendix D.

4.1.3 Wetting dynamics

The contact angle Θ quantifies the wettability of a solid surface by a liquid via the Young's equation [103]. Hence, the wetting dynamics can be incorporated in the lattice Boltzmann simulations by creating a boundary condition that reproduces Young's equation in equilibrium [98]. The solid – liquid and solid – vapour surface tensions can be incorporated in the Landau free energy functional by the addition of a surface term [98]. Cahn [104] assumed that the fluid – solid interactions are short ranged so that they contribute to the total free energy of the system with a surface integral:

$$\Psi_s = \int_S dS \Phi(\rho_s). \quad (4.10)$$

The total free energy becomes:

$$\Psi = \int_V dV \left[\psi(\theta, \rho) + \frac{\chi}{2} (\partial_\alpha \rho)^2 \right] + \int_S dS \Phi(\rho_s) \quad (4.11)$$

where S is the surface bounding V . The surface free energy density $\Phi(\rho_s)$ depends only on the fluid density at the surface ρ_s .

Following some assumptions described in [98], the desired contact angle Θ can be imposed in the simulation by calculating the required wetting potential ϕ where

$$\Phi(\rho_s) = -\phi\rho_s. \quad (4.12)$$

The wetting potential that should be prescribed in the algorithm (see appendix D) is:

$$\phi = \Omega \left(1 - \frac{\theta}{\theta_c} \right) \frac{\sqrt{2\chi}}{\chi} \quad (4.13)$$

where Ω is a dimension-less wetting potential that should satisfy the equation:

$$\cos(\Theta) = \frac{\left((1 + \Omega)^{\frac{3}{2}} - (1 - \Omega)^{\frac{3}{2}} \right)}{2}. \quad (4.14)$$

Additional information about the numerical methods that are used to calculate the gradients near solid boundaries and to define the contact angle can be found in appendix D.

4.1.4 Implementation

A free energy lattice Boltzmann algorithm was previously written in MATLAB by McDonald as reported in [10]*. The algorithm was re-cast and optimized by the author in C by extending the effective media algorithm that was initially developed for isothermal fluids in chapter 3 section 3.2[†]. The effective media parameter was restricted to $\sigma = 0$ and $\sigma = 1$ in order to disallow the presence of grey nodes and to recover a *standard* LB model. The effective media parameter will be relaxed to $\sigma = [0, 1]$ so as to include grey nodes in section 4.2.

As part of this work, the following model was implemented. The equilibrium distribution functions were set according to equation 4.7 in order to implement a pressure tensor in the algorithm and to describe the fluid with a van der Waals equation of state. A single-relaxation-time collision operator was used where, for numerical efficiency, the relaxation time was set to $\tau = 1$. The no-slip fluid-solid boundary condition was taken into account in an implicit way with equation 3.24 on solid boundaries marked with $\sigma = 1$. The wetting dynamics were incorporated via equation 4.10. Systems were equilibrated in the absence of external forces. *Closed* systems had periodic boundary conditions in the three spatial directions to minimize boundary effects. *Open* systems were connected to a *source* at a controlled density (vapour relative humidity) and periodic boundary conditions were applied in the two remaining spatial directions.

* [10] was a collaborative study where the present author was primarily responsible for the permeability simulations and Peter McDonald was primarily responsible for the desorption simulations.

[†]The author would like to acknowledge the help of Dr. Cyrille Dunant with the performance aspects of the code.

4.1.5 Methods for modelling adsorption and desorption

The adsorption and desorption isotherms are usually obtained by plotting the water content at equilibrium *vs.* the relative humidity (RH) of the surrounding environment. To model adsorption and desorption using a lattice Boltzmann algorithm, the test structures are first put in contact with a *source* of vapour at a controlled RH. As a result of periodic boundary conditions, the source is effectively in contact with the test structure from two sides. For optimal stability, the source is given a width of $1 + 2(\varpi + 1)$ where ϖ is the width of the liquid – vapour interface and the RH is fixed only in the middle layer. The maximum relative humidity, 100%, corresponds to the gas density ρ_{gas} of the Van der Waals fluid. Hence, the density, and consequently the RH, can be fixed by using the equation of state of the fluid (equation 4.6). To model the isotherms, all the pores are initially saturated with liquid ($\rho = \rho_{liquid}$) and the source is initialized to 100% RH ($\rho = \rho_{gas}$). Once the system is equilibrated, the RH of the source is progressively reduced and the system re-equilibrated at each RH step. Afterwards, the RH is progressively increased back to 100%. At each RH step, the convergence is considered to be achieved when the relative mass change per 5000 time steps is less than 10^{-5} . Finally, the isotherms are obtained by plotting the average density in the fluid nodes as a function of the relative humidity.

4.1.6 Validation

Previous validation by McDonald

A free energy algorithm, similar to the one implemented above, was previously validated by McDonald as reported in [10]. It was shown that the contact angle varies approximately linearly with the surface normal fluid density (figure 4.2). It was also shown that the pressure decrease across the interface of a spherical liquid drop in vapour varies inversely with its radius (figure 4.3) and that the simulated interfacial tension is within 6% of the input.

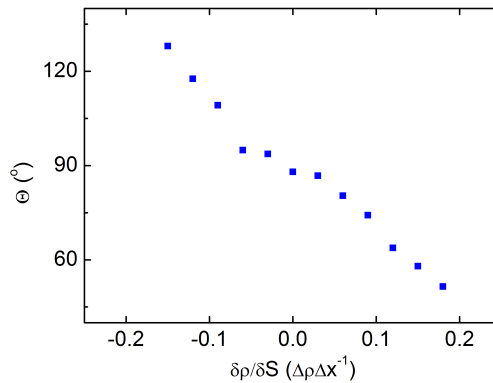


Figure 4.2: Contact angle Θ *vs.* the surface-normal fluid density gradient.

It was also noted that for a system that comprises a liquid reservoir maintained full by a

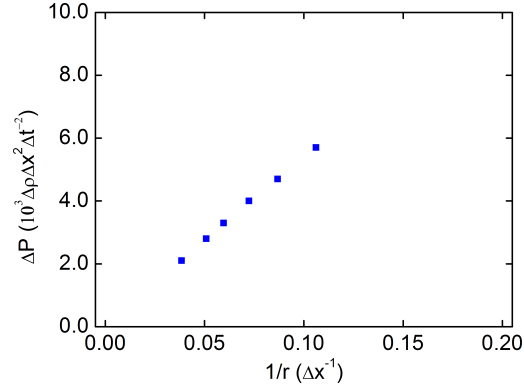


Figure 4.3: Pressure drop across the liquid – vapour interface of a droplet *vs.* the inverse of the radius r of the droplet.

liquid source and coupled to a large vapour reservoir by a capillary, the liquid rose in the capillary with the square root of time (figure 4.4). Finally, it was observed that at reduced vapour pressures, liquid pendular rings condensed between the near points of a cubic array of liquid-wetting spheres (figure 4.5).

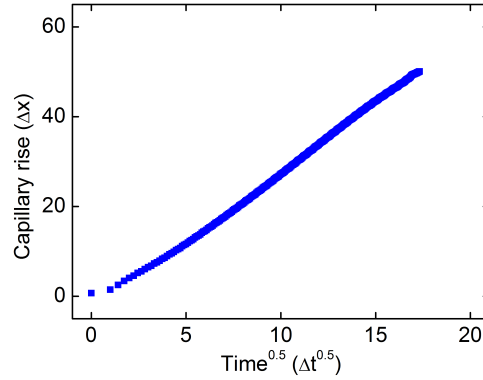


Figure 4.4: Capillary rise *vs.* the square root of time.

The simulations described above were carried out at reduced temperatures θ/θ_c ranging from 0.8 to 0.96. The resulting liquid to vapour density ratio ranges between 8.1 and 2.3. This relatively small liquid to vapour density ratio is a key limitation of LB models. Wagner and Pooley [100] have shown how relatively large density differences, corresponding to a low temperature θ , can be achieved by introducing a pressure scaling factor ξ as shown in equation 4.3. However, McDonald reported that the required computational times became prohibitive in the case of large density ratios in porous media [10]. Nonetheless, it can be shown that the equilibrium fluid distributions obtained at reduced temperatures ranging from 0.5 to 0.96 (correspond to density ratios of 113 to 2.3) are broadly similar [10] (figure 4.6).

Another difficulty in diffuse interface models is to adequately characterize the liquid – vapour

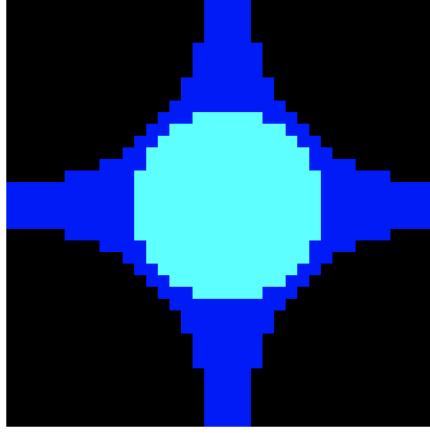


Figure 4.5: 2D snapshot of pendular rings formed between packed liquid-wetting spheres. Liquid is shown in blue, vapour in cyan and solids in black.

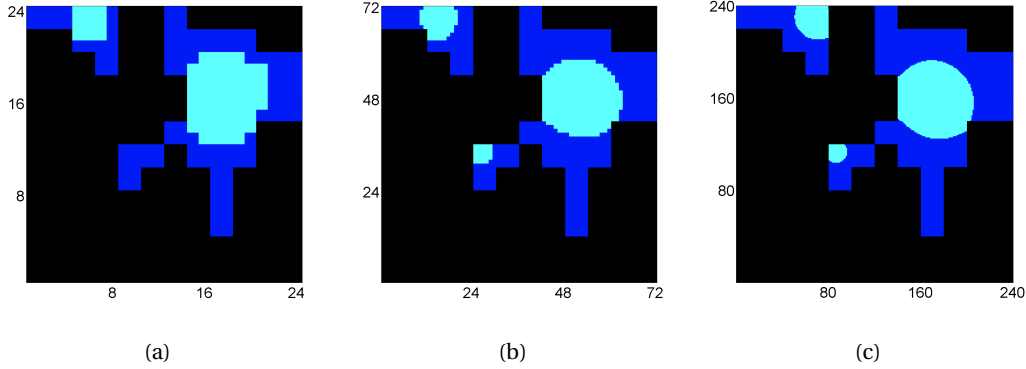


Figure 4.6: Equilibrium fluid distributions obtained at three different reduced temperatures (liquid to vapour density ratios) of (a) 0.95 (2.3), (b) 0.8 (8.1) and (c) 0.5 (113) for a constant bulk liquid volume fraction of $2/3$. Liquid is shown in blue, vapour in cyan and solids in black. The microstructure is the same in each case but the resolution varies by a factor of 10 between the first and last. The computation time increases by a factor of approximately 10000. The key observation, however, is that the essential fluid distribution is similar for the three reduced temperatures.

interfaces. When working on the mesoscale, the lattice space Δx of the simulation, and therefore the interface width, will be on the order of micrometres. Hence, the interface width will be around 1000 times larger than its correct physical value. The effect of the large interface is that, for example, a liquid drop moves quicker than observed experimentally [105]. However, there is no evidence that the drop does not follow the correct dynamical pathway [105] or that the equilibrium distribution of the fluid is affected.

Consequently, for the simulations to be feasible, the simulated liquid – vapour density ratio and interface width are always smaller and larger, respectively, than their correct physical values. These limitations are expected to have a relatively limited impact on the overall results [10, 105].

Further validation

All the following simulations were carried out at a reduced temperature $\theta/\theta_c = 0.96$ yielding a liquid density of $\rho_{liquid} = 1.41$ and a gas density of $\rho_{gas} = 0.62$. The pressure scaling factor was set to $\xi = 0.5$. The parameter describing the liquid – vapour interfaces χ was calculated in order to return the desired interface width ϖ following [100]:

$$\chi = \frac{\varpi^2}{2} \left(\frac{\theta_c}{\theta} - 1 \right). \quad (4.15)$$

The interfacial tension is then given by:

$$\gamma = \frac{4}{3} \sqrt{\frac{16\chi}{3}} \left(1 - \frac{\theta}{\theta_c} \right)^{\frac{3}{2}}. \quad (4.16)$$

The simulations were considered to be converged when the maximum density variation per 5000 time steps was smaller than 10^{-6} .

Young-Laplace equation The Laplace pressure is the difference in pressures between the inside and the outside of a curved surface. It is caused by the surface tension at the interface between the liquid and gaseous phases and can be expressed with:

$$\Delta P = \frac{2\gamma}{r} \quad (4.17)$$

where γ is the surface tension and r is the radius of the droplet.

To validate the multi-phase algorithm, cubic boxes of different side lengths L were initialized with centred liquid (ρ_{liquid}) spheres of radius $r = \frac{L}{3}$, surrounded by vapour of density ρ_{gas} , and left to equilibrate. The interface width was set to $\varpi = 1$. Snapshots of the liquid density contours are shown in figure 4.7 at initialization and at equilibrium for a system of size $L^3 = 51^3$.

The relative error between the input (equation 4.16) and output (calculated from the slope of the fit line to the data of figure 4.8) is $\sim 6\%$, as previously observed by McDonald [10]. In the implemented LB algorithm, the surface tension increases linearly with the interface width (equations 4.15 – 4.16). Figure 4.9 shows the Laplace pressure as a function of the inverse of the radius for an interface width of $\varpi = 2$. The slope of the linear fit, and consequently the simulated surface tension, is, as expected, twice larger than that obtained with $\varpi = 1$. Again, the relative error in the simulations is $\sim 6\%$.

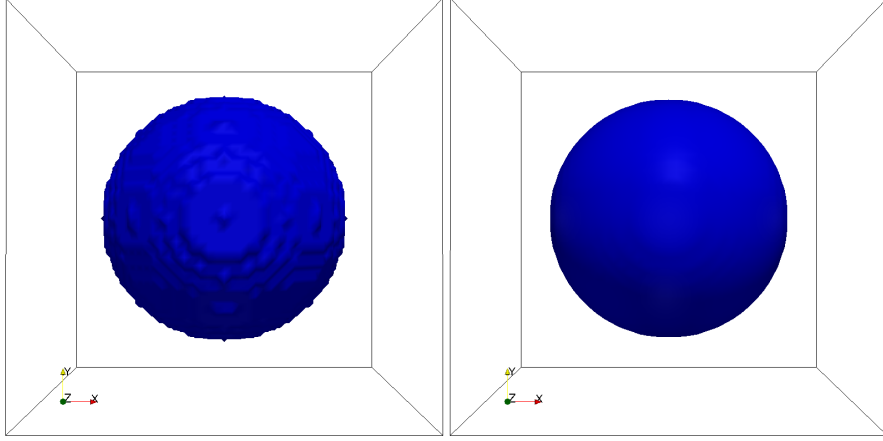


Figure 4.7: Contour of the liquid phase at (left) initialization and (right) equilibrium. Liquid is shown in blue and vapour in white.

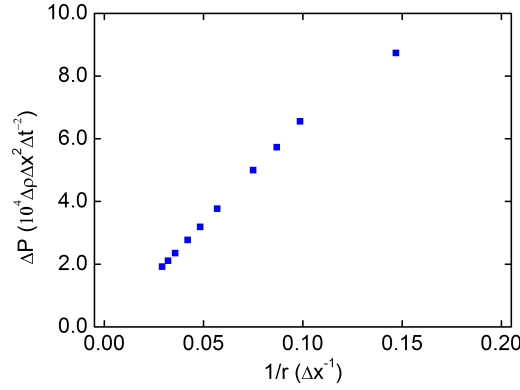


Figure 4.8: Pressure drop across the liquid – vapour interface of a droplet *vs.* the inverse of the radius r of the droplet. The interface width is $\varpi = 1$.

Spinodal decomposition To investigate phase separation, cubic boxes of different side lengths L were randomly initialized with fluid nodes with densities in the range $\rho = 1 \pm 0.05$ close to the critical density $\rho_c = 1$. Phase separation must take place in order to minimize the surface energy. There are two acceptable *physical* solutions. The first is the formation of a sphere since a sphere has the lowest surface to volume ratio. The second solution, which exists only because of the periodic boundary conditions, is the formation of two parallelepipeds. In this particular case, the surface to volume ratio is lower than that of the sphere because the periodic boundary conditions can *cancel* the surface in one of the spatial directions. Figure 4.10 shows the fluid distribution at equilibrium for two different random initial distributions in boxes of size $L^2 = 21^2$ for an interface width of $\varpi = 1$. It is clear that the liquid – vapour interface is much smaller in the case of parallelepipeds.

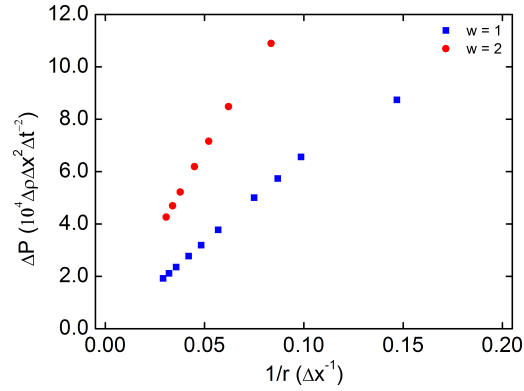


Figure 4.9: Pressure drop across the liquid – vapour interface of a droplet *vs.* the inverse of the radius r of the droplet. The interface width is $\varpi = 1$ or $\varpi = 2$.

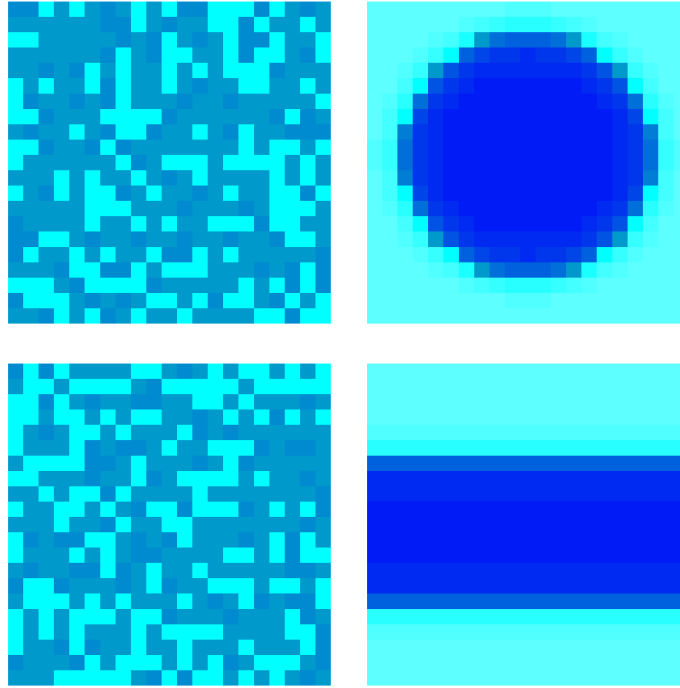


Figure 4.10: Fluid distribution at (left) initialization and (right) equilibrium. Liquid is shown in blue and vapour in cyan.

Spinodal decomposition in solid-bound environments To investigate phase separation in solid-bound environments, cubic boxes of different side lengths L were randomly initialized with fluid nodes with densities in the range $\rho = 1 \pm 0.05$ close to the critical density $\rho_c = 1$ and surrounded by solid walls. In addition to the tendency of the system to minimize the interfaces, the equilibrium fluid distribution is dependent on the interactions between the fluid and solid nodes as described by the contact angle. Figure 4.11 shows the equilibrium

distributions of the fluid for wetting and non-wetting solid boundaries for a system of size $L^3 = 71^3$ for an interface width of $\varpi = 1$. As expected, spherical shapes of vapour and liquid develop in the centre of the boxes for wetting and non-wetting solid boundaries, respectively.

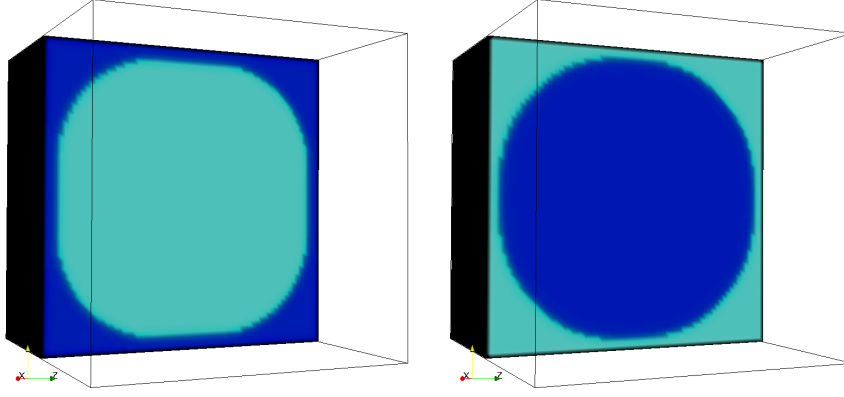


Figure 4.11: Fluid distribution at equilibrium for a liquid – solid contact angle of (left) 45 and (right) 135. Liquid is shown in blue, vapour in cyan and solids in black.

Contact angles To investigate the formation of contact angles on solid surfaces, boxes of different sizes $L_x \times L_y \times L_z$ were initialized with centred liquid (ρ_{liquid}) semi-spheres of radius $r = \frac{2}{3}L_y$, surrounded by vapour of density ρ_{gas} , set on a solid impermeable surface, and left to equilibrate. The interface width was set to $\varpi = 1$. The wetting potentials were set to $\phi = 0.187$ and $\phi = -0.187$ to obtain contact angles of $\Theta = 45^\circ$ and $\Theta = 135^\circ$, respectively. Figure 4.12 shows the fluid distribution at initialization and at equilibrium for a system of size $70 \times 30 \times 70$ and contact angles of 45 and 135 degrees.

The contact angles were calculated with the tangent method by fitting the liquid drop to the arcs of imaginary circles. Table 4.1 shows the simulated contact angles for a wide range of system sizes and for different initial shapes of the liquid drop. In general, the simulated contact angle is within $\sim 5^\circ$ of the input value. In some cases, the initial quantity of liquid in the system was too large so that the liquid spread over all of the surface and the contact angle could not be calculated (it is effectively 0°). It is worth noting that the accuracy of the algorithm was not affected by the initial shape of the liquid as proven in the few test cases where the liquid drop was initialized with a cubic shape.

Kelvin's equation The Kelvin equation describes the changes in vapour pressure due to the curvature of a liquid – vapour interface of radius r with:

$$RH = \exp\left(-\frac{2\gamma M^* \cos(\Theta)}{rRT\rho}\right) \quad (4.18)$$

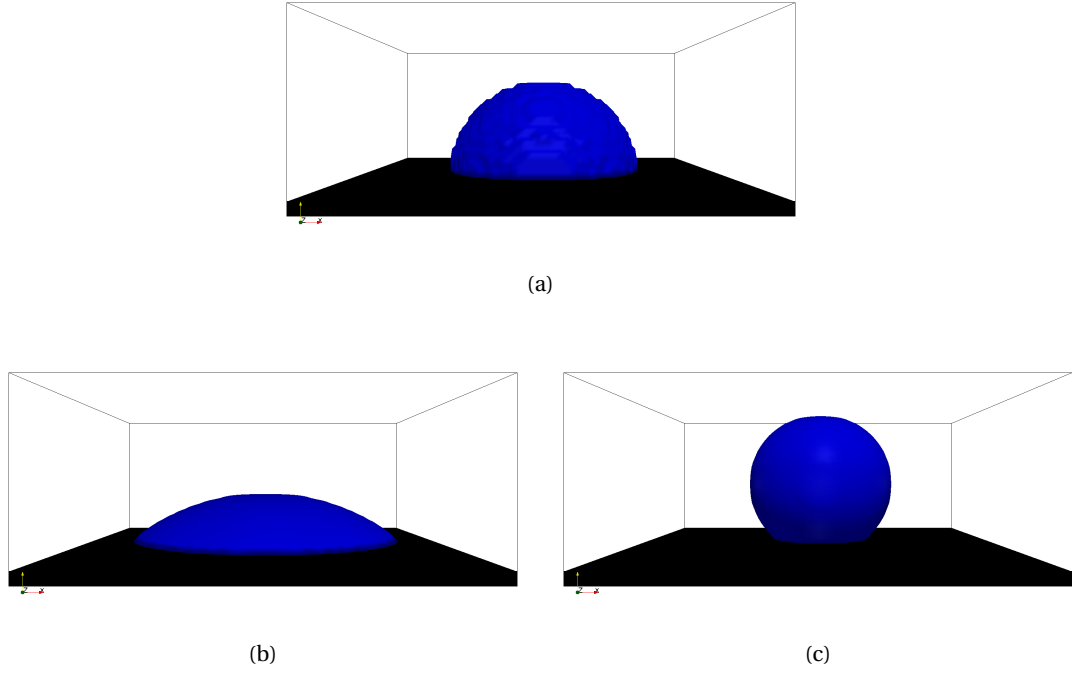


Figure 4.12: Fluid distribution at (a) initialization and (b-c) equilibrium for a liquid – solid contact angle of (b) 45 and (c) 135 degrees. Liquid is shown in blue, vapour in white and solids in black.

Table 4.1: Simulated equilibrium contact angles between liquid and solid.

$L_x \times L_y \times L_z$	Initial liquid drop radius	45°	135°
50 × 20 × 50	12	48.0°	135.8°
70 × 30 × 70	18	42.8°	138.4°
100 × 40 × 100	25	43.0°	140.7°
50 × 30 × 50	18	N.A.	139.9°
70 × 40 × 70	25	N.A.	140.1°
70 × 40 × 70	Cube of side length 30	N.A.	142.1°
120 × 40 × 120	25	43.0°	140.7°
70 × 30 × 70	Cube of side length 20	46.4°	146.0°

where RH is the relative vapour pressure, R the universal gas constant, T the absolute temperature, Θ the contact angle, M^* , ρ and γ the molar mass, density, and surface tension of the fluid, respectively. The Kelvin equation is often used to estimate, for a certain set of parameters $\{\gamma, M^*, \rho, \Theta, R, T\}$, the relative humidity at which pores of a certain radius r will become devoid of liquid water. To test this, desorption curves were modelled for spherical pores of different radii as illustrated in figure 4.13. The simulation parameters were $\theta/\theta_c = 0.96$, $\omega = 1$ and $\Theta = 30^\circ$.

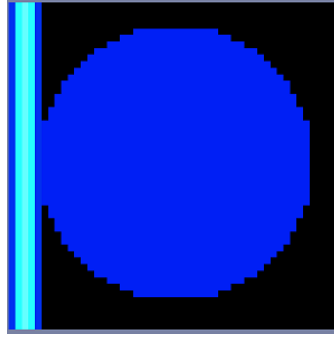


Figure 4.13: 2D slice of a spherical pore in contact with a vapour source at a controlled RH. Liquid is shown in blue, vapour in cyan and solids in black.

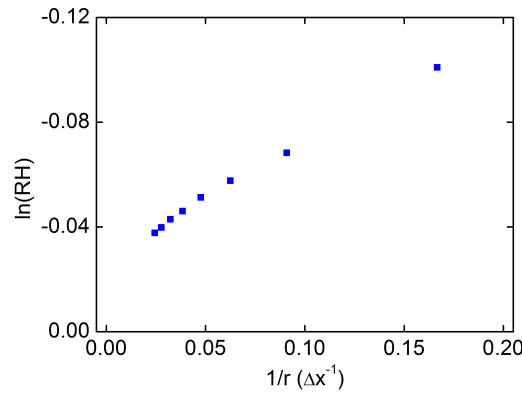


Figure 4.14: Natural logarithm of the RH at which a pore of radius r empties from liquid water *vs.* the inverse of the radius.

Figure 4.14 shows the natural logarithm of the relative humidity at which a pore of radius r empties from liquid water *vs.* the inverse of the radius. The natural logarithm of the RH varies approximately linearly with the inverse of the radius, in agreement with equation 4.18.

Ink-bottle effect Caution is required when using the Kelvin equation to check whether, for a certain set of parameters $\{RH, \gamma, M^*, \rho, \Theta, R, T\}$, a pore of radius r is devoid of liquid water. Figure 4.15 shows a 2D system of size 125 x 75 composed of three serial pores of radii 12, 36 and 12 lattice units. The system is connected to a vapour source at a controlled RH.

Simulations show that for a contact angle of $\Theta = 30^\circ$, 2D pores of radii 36 and 12 should empty at ~ 96.9 and 96.2% RH, respectively. However, when set up as in figure 4.15, the large pore does not have a direct access to the vapour source. Consequently, it *cannot* empty at 96.9% RH. Rather, it has to wait until a liquid-free access to the vapour source becomes available. This happens at 96.2% RH, when the small pore on the LHS empties (figure 4.16).

This phenomenon is known as the ink-bottle effect and plays a critical role in complex multi-

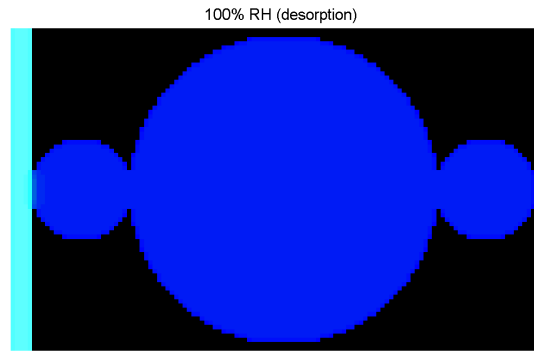


Figure 4.15: Illustration of the ink-bottle effect: Three pores of different radii in contact with a vapour source at a controlled RH. Liquid is shown in blue, vapour in cyan and solids in black.

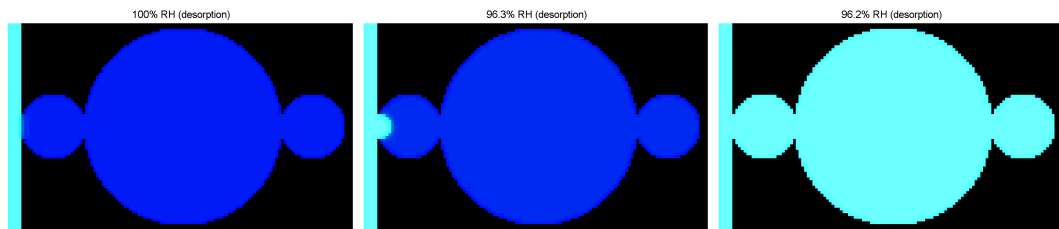


Figure 4.16: Equilibrium fluid distributions during desorption at 100%, 96.3% and 96.2% RH. Liquid is shown in blue, vapour in cyan and solids in black.

scale porous materials like cement paste. Figure 4.17 shows the *non-equilibrium* fluid distribution in the system at different simulation time steps between 96.3 and 96.2% RH.

Finally, it is worth noting that this particular system, with a contact angle of $\Theta = 30^\circ$, did not re-fill with liquid when the RH was increased back to 100%. This is because the equilibrium at 100% RH consists of a system filled with vapour. However, for a contact angle of $\Theta = 0^\circ$, the system re-filled with liquid and the inkbottle effect was not observed during adsorption (figure 4.18). In this case, the small pore on the RHS refilled with liquid water before the larger pore, as expected from the Kelvin equation (figure 4.19).

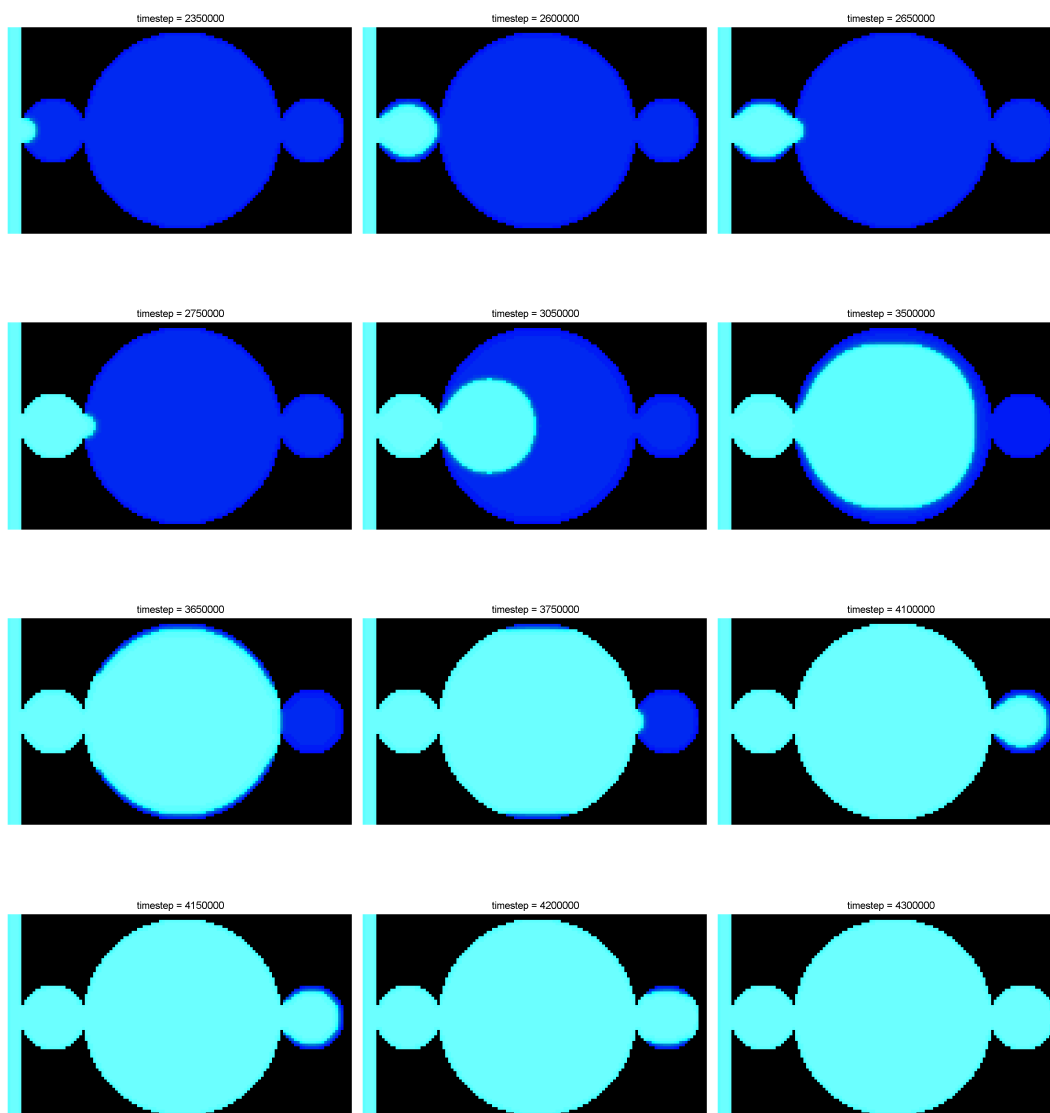


Figure 4.17: Non-equilibrium fluid distributions during desorption between 96.3 and 96.2% RH. Liquid is shown in blue, vapour in cyan and solids in black.

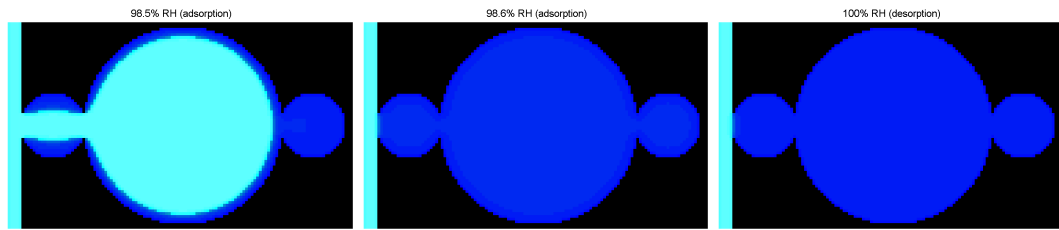


Figure 4.18: Equilibrium fluid distributions during adsorption at 98.4%, 98.5% and 98.6% RH. Liquid is shown in blue, vapour in cyan and solids in black.

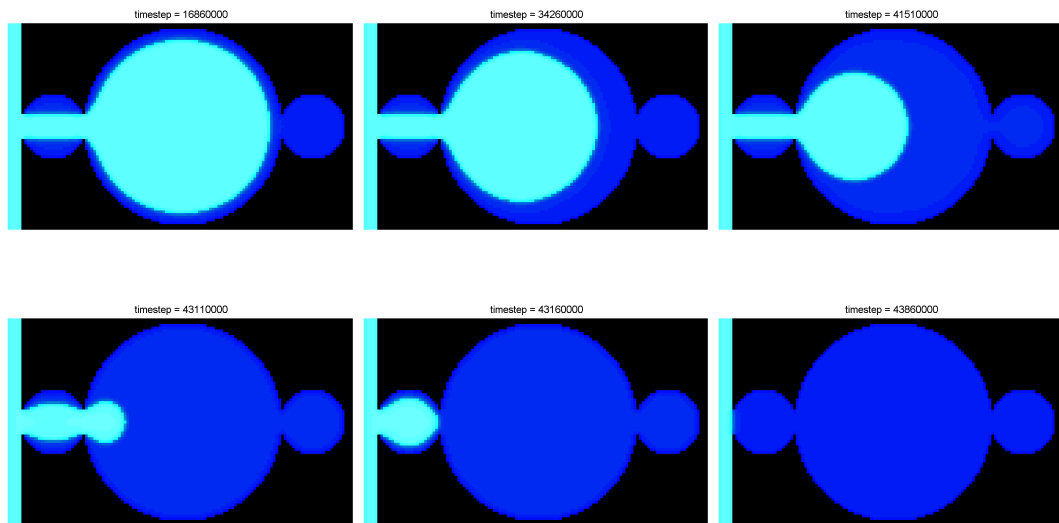


Figure 4.19: Non-equilibrium fluid distributions during adsorption between 98.5 and 98.6% RH. Liquid is shown in blue, vapour in cyan and solids in black.

4.2 Effective media methods for the transport and wetting properties

4.2.1 Overview

The methodology introduced in chapter 3 section 3.2 allows the introduction of grey nodes with effective transport properties. This allows, as will be shown in chapter 5 section 5.2 to overcome the difficulty of modelling the flow in microstructures where the porosity spans several length scales. The approach introduced in section 4.1 makes it possible to describe the fluid with an equation of state. This is necessary, as will be shown in chapter 6, to study desorption and adsorption of water in unsaturated cement paste model microstructures. The question that arises is whether the two methods can be combined to tackle both problems simultaneously, that is, whether it is possible to define grey nodes with effective transport *and* wetting properties.

In this section, the novel step is made of interpreting the effective wetting within a free energy framework. This is done without rigorous mathematical derivation and perhaps, such a derivation is not possible. However, this approach has great merit as will be shown below and in chapter 6. The method combines two independent parameters, the effective media parameter σ_{grey} that describes the intrinsic permeability of the grey nodes, with the internal wetting parameter ϕ_{grey} that describes the wetting behaviour of the grey nodes. Having two independent parameters enables the model to be tuned so as to reasonably characterize both permeability and adsorption and desorption isotherms. Neither of the previous models could do this alone. In particular, it will be shown that the sorption isotherms are independent of the permeability (as long as the grey nodes are permeable). It will also be shown that two-step isotherms can be obtained for media composed of pores, grey nodes, and solids.

4.2.2 Free energy approach for effective wetting properties

The free energy functional was previously defined for fluid nodes ($\sigma = 0$) in bulk (equation 4.1) and near solid surfaces (equation 4.10). The presence of grey nodes ($0 < \sigma < 1$) creates an additional class of bulk nodes. Thus, the volume term of equation 4.1, originally including only the fluid nodes $V \subset \{\sigma = 0\}$, should henceforth include the grey nodes so that: $V \subset \{0 \leq \sigma < 1\}$.

Moreover, the presence of grey nodes creates additional classes of surfaces. Accordingly, equation 4.10, $\int_S dS \Phi(\rho_s)$, is extended to:

$$\sum_{\zeta} \int_{S_{\zeta}} dS_{\zeta} \Phi_{\zeta}(\rho_{\zeta}) \quad (4.19)$$

4.2. Effective media methods for the transport and wetting properties

where the sum is over the classes of surfaces ς . In the simplest case, the surfaces are:

$$\varsigma \subset \left\{ \begin{array}{l} \text{fluid over solid nodes} \\ \text{fluid over grey nodes} \\ \text{grey over solid nodes} \end{array} \right\}. \quad (4.20)$$

Lastly, it is assumed that the grey nodes contribute an effective energy to the total free energy through their internal wetting via:

$$\int_{V_{grey}} dV_{grey} \Phi_{grey}(\rho_{grey}) \quad (4.21)$$

where $\Phi_{grey}(\rho_{grey})$ characterizes the internal wetting of the grey nodes. The total free energy therefore becomes:

$$\Psi = \int_V dV \left[\psi(\theta, \rho) + \frac{\chi}{2} (\partial_\alpha \rho)^2 \right] + \sum_\varsigma \int_{S_\varsigma} dS_\varsigma \Phi_\varsigma(\rho_\varsigma) + \int_{V_{grey}} dV_{grey} \Phi_{grey}(\rho_{grey}). \quad (4.22)$$

The effective media parameter σ_{grey} defines the grey nodes in terms of intrinsic transport properties and Φ_{grey} defines them in terms of internal wetting. The characteristic features of this effective free energy will be demonstrated in the next sections.

4.2.3 Implementation

The effective media free energy algorithm was implemented as an extension to the standard free energy algorithm as previously discussed in section 4.1.4.

4.2.4 Methods for modelling adsorption and desorption

The isotherms are modelled in a similar fashion to that discussed in section 4.1.5. However, in addition to the pores, the grey nodes are initialized with liquid water and are included in the calculation of the average mass of adsorbed fluid.

4.2.5 Validation

For the validation of the effective media algorithm for non-ideal fluids, the interactions between fluid and grey nodes, between grey and solid nodes, and *inside* grey nodes were analysed. All the following simulations were carried out at a reduced temperature $\theta/\theta_c = 0.96$ yielding a liquid density of $\rho_{liquid} = 1.41$ and a gas density of $\rho_{gas} = 0.62$. The pressure scaling factor was set to $\xi = 0.5$. The parameter describing the liquid – vapour interfaces χ was calculated using equation 4.15 in order to return an interface width $\varpi = 1$.

Spinodal decomposition inside grey nodes

To test the liquid – vapour phase separation in systems composed of grey nodes, simulation boxes of size $L^2 = 21^2$ were initialized with grey nodes with densities in the range $\rho = 1 \pm 0.05$ close to the critical density $\rho_c = 1$. Phase separation takes place, as previously observed in section 4.1.6, in order to minimize the interfaces and independently of the value of the imposed internal wetting potential ϕ_{grey} or intrinsic permeability κ_{grey} . However, when the simulation boxes are surrounded by solid walls, the results of the phase separation, *i.e.* where the liquid condensates and which phase wets the solid boundaries, depend on a complex interplay between the wetting potentials $\phi_{grey/solid}$ and ϕ_{grey} . Figure 4.20 shows the equilibrium fluid distribution for different values of the wetting potentials $\phi_{grey/solid}$ and ϕ_{grey} .

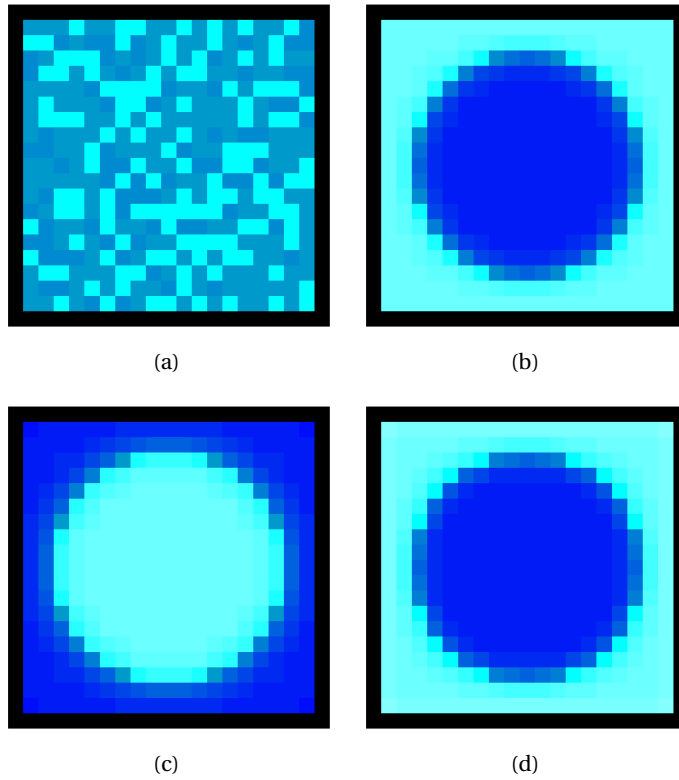


Figure 4.20: Fluid distribution at (a) initialization and (b-d) equilibrium for systems composed of grey nodes and bound by solids. In (b) $(\phi_{grey/solid}, \phi_{grey}) = (0.19, 0.13)$, in (c) $(\phi_{grey/solid}, \phi_{grey}) = (0.19, 0.07)$ and in (d) $(\phi_{grey/solid}, \phi_{grey}) = (-0.19, 0.13)$. Liquid is shown in blue, vapour in cyan and solids in black.

Figure 4.20 shows that even when the grey nodes are defined to wet the solid ($\phi_{grey/solid} > 0$) as shown in parts (b) and (d), the equilibrium distribution of the fluid, *i.e.* if the grey nodes do indeed wet the solid, depends on the degree of internal wetting of the grey nodes. This is expected as for high values of ϕ_{grey} , the grey nodes would prioritize wetting themselves. In figure 4.20(c), the wetting potential between the grey and solid surfaces ($\phi_{grey/solid}$) is larger than the internal wetting potential ϕ_{grey} . In this case, the grey nodes do wet the solid surfaces.

Contact angles on grey surfaces

To investigate the formation of contact angles on weakly-permeable grey surfaces, the contact angle test of section 4.1.6 was repeated and the solid nodes were replaced with liquid-saturated grey nodes. The wetting potentials were set to $\phi_{fluid/grey} = 0.187$ and $\phi_{fluid/grey} = -0.187$ to obtain contact angles of $\Theta_{fluid/grey} = 45^\circ$ and $\Theta_{fluid/grey} = 135^\circ$, respectively. The effective media parameter of the grey nodes was set to $\sigma_{grey} = 0.9$ and their wetting potential was set to $\phi_{grey} = 0.267$. Table 4.2 shows the calculated equilibrium contact angles for a wide range of system sizes and for different initial shapes of the liquid drop. It is clear that the presence of liquid in the grey nodes has not affected the ability of the model to recover an equilibrium contact angle.

Table 4.2: Simulated equilibrium contact angles between liquid and grey nodes.

$L_x \times L_y \times L_z$	Initial liquid drop radius	45°	135°
$50 \times 20 \times 50$	12	45.0°	142.0°
$70 \times 30 \times 70$	18	$44.4.8^\circ$	142.4°
$100 \times 40 \times 100$	25	43.0°	140.7°
$70 \times 40 \times 70$	25	N.A.	140.7°
$120 \times 40 \times 120$	25	44.2°	140.7°
$70 \times 30 \times 70$	Cube of side length 20	41.7°	135.5°

Figure 4.21 shows the fluid distribution at initialization and at equilibrium for a system of size $70 \times 30 \times 70$ and contact angles between the liquid and the grey nodes of 45 and 135 degrees.

Internal wetting of the grey nodes

To better understand the wetting *behaviour* of grey nodes, water isotherms were modelled for homogenous systems composed of grey nodes only. The size of the systems was $L^3 = 10^3$ and the effective media parameter of the grey nodes was set to $\sigma_{grey} = 0.01$. Figure 4.22 shows the desorption and adsorption curves for different numerical values of the internal wetting potential ϕ_{grey} ranging from 0.067 to 1.6.

As described in section 4.2.4, regardless of the internal wetting potential, the grey nodes are initially saturated with liquid and their density is $\rho_{grey} = \rho_{liquid} = 1.41$. Figure 4.22(b) shows that as the internal wetting potential ϕ_{grey} is increased, the amount of liquid adsorbed at equilibrium, when the external RH is 100% RH, increases. This is consistent with the expectations from the *definition* of the internal wetting potential. Moreover, the system with the highest wetting potential *retains* the liquid fluid for longer when the surrounding RH is decreased and starts adsorbing the liquid fluid earlier when the surrounding RH is increased. All the tested systems show considerable hysteresis. For the lowest value of internal wetting potential, $\phi_{grey} = 0.067$, the potential was not large enough to allow the fluid to condense when the RH of the source was increased back to 100%. For the highest value of internal

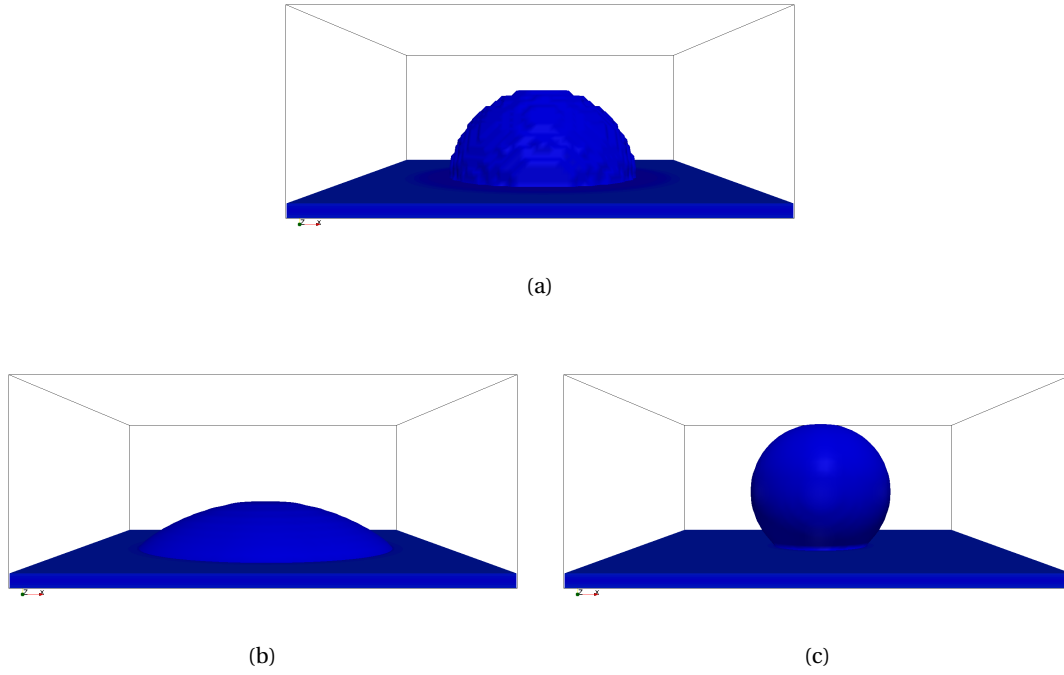


Figure 4.21: Fluid distribution at (a) initialization and (b-c) equilibrium for a liquid – grey contact angle of (b) 45 and (c) 135 degrees. Liquid is shown in blue and vapour in white. The grey nodes are saturated with liquid and thus appear blue.

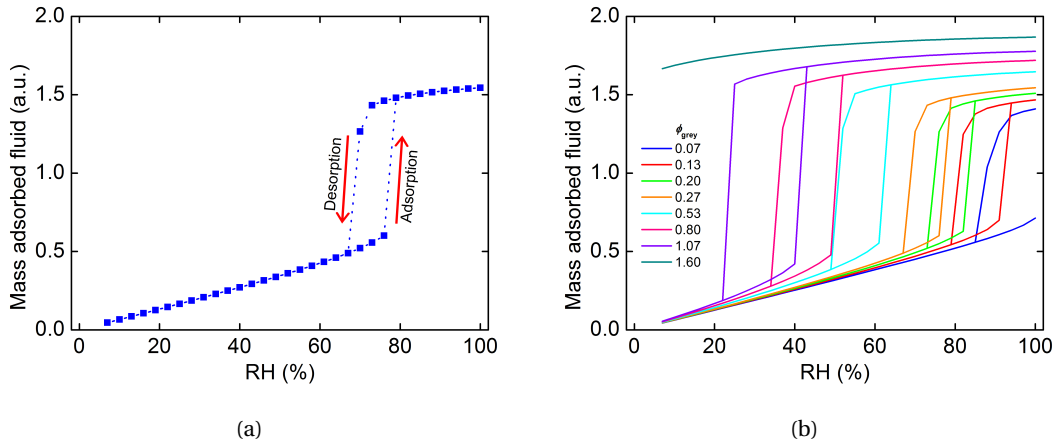


Figure 4.22: Mass of adsorbed fluid *vs.* the RH for different values of internal wetting potential of the grey nodes ϕ_{grey} . In (a) $\phi_{grey} = 0.27$. In (b) ϕ_{grey} ranges from 0.067 to 1.6.

wetting, $\phi_{grey} = 1.6$, the wetting potential was very high and the system *held* the liquid water down to the smallest tested RH, 7%. Lastly, it is worth noting that for $\phi_{grey} = 0$, the algorithm recovers the standard free energy model without grey nodes. In this case, because of the periodic boundary conditions in two of the spatial directions, the system is *effectively* infinite

and consequently does empty at 100% RH and does not refill.

Figure 4.23 shows the effect of varying multiple parameters while keeping the internal wetting potential constant at $\phi_{grey} = 0.267$. First, the internal wetting was verified to be independent of the transport properties of the grey nodes. This was confirmed by varying the intrinsic permeability of the grey nodes by a factor 891 ($\sigma_{grey} = 0.01$ to $\sigma_{grey} = 0.9$). This was expected as the isotherms are obtained at mass equilibrium and should be independent of the dynamics. Second, the isotherms were verified to be independent of the size of the system. This was tested by increasing the size of the system by 16 times from $10 \times 10 \times 10$ to $10 \times 40 \times 40$ and keeping constant the size of the surface exposed to the vapour source. The results of figure 4.23 show that the grey nodes possess intrinsic isotherms that are only dependent on the wetting potential ϕ_{grey} , and thus could be ultimately linked with a *characteristic pore size*.

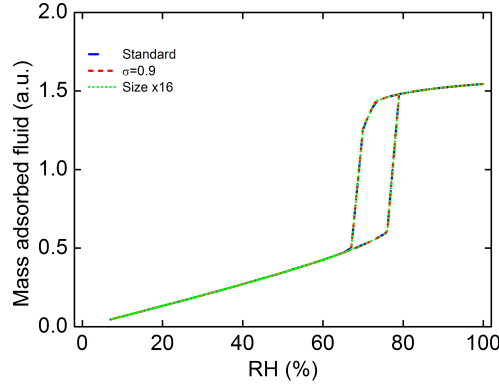


Figure 4.23: Mass of adsorbed fluid *vs.* the RH for different system sizes and intrinsic permeabilities.

4.2.6 Application to a 2D characteristic microstructure

To better understand the effect of the inclusion of grey nodes on the isotherms of a porous medium, two 2D *pseudo*-random systems of size 67×30 were created out of pores, grey, and solid nodes as illustrated in figure 4.24.

First, the isotherms of system A were modelled. The grey nodes were characterized with a wetting potential $\phi_{grey} = 0.27$ and an effective media parameter $\sigma_{grey} = 0.01$. It is worth noting that the water isotherms were proven to be independent of the permeability of the grey nodes in section 4.2.5. The interface wetting potentials were set to $\phi_{fluid/solid} = \phi_{fluid/grey} = \phi_{grey/solid} = 0.27$ to return contact angles of $\Theta_{fluid/solid} = \Theta_{fluid/grey} = \Theta_{grey/solid} = 0^\circ$. Second, the isotherms of system B were modelled. The grey nodes were treated as impermeable solids ($\sigma_{grey} = 1$) with no internal wetting ($\phi_{grey} = 0$). The fluid – solid wetting potential was set to $\phi_{fluid/solid} = 0.27$ to return a contact angle of $\Theta_{fluid/solid} = 0^\circ$.

The isotherms of systems A and B are shown in figure 4.25. There are several important

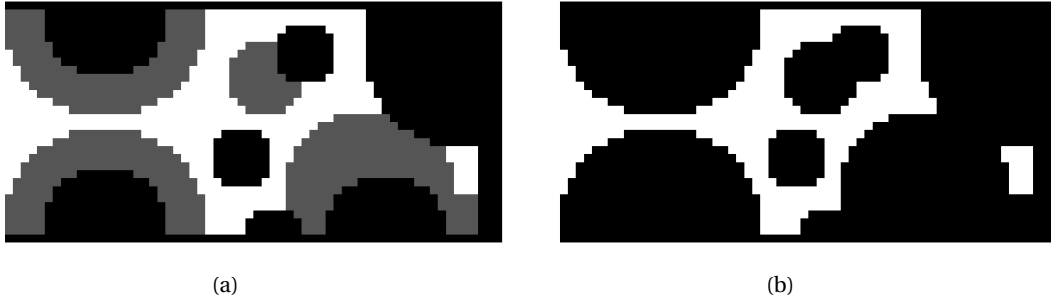


Figure 4.24: (a) System A: a 2D characteristic system composed of pores (white), grey nodes (grey) and solid nodes (black). The system is connected to a vapour source from the LHS. (b) System B: a modified version of system A where the grey nodes are considered impermeable solids with no internal wetting (like a standard LB algorithm).

observations. First, system A empties in two different regimes. The first regime ($\sim 100 - 85\%$ RH) can be attributed to the fluid pores and the second regime ($\sim 85 - 75\%$ RH) to the grey nodes. This division can be confirmed by separately plotting the average densities in fluid pores and in grey nodes as shown in figure 4.26.

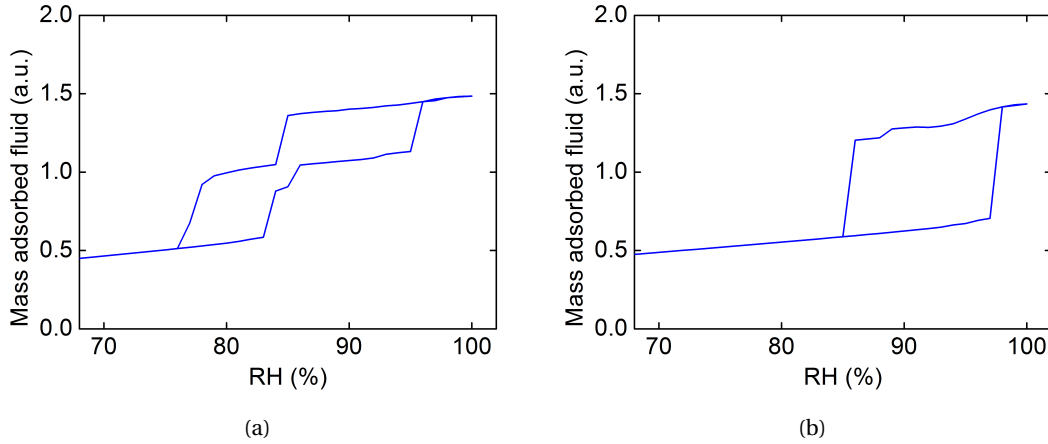


Figure 4.25: Water isotherms of systems (a) A and (b) B.

The second observation is that the average density in the fluid pores of System A is remarkably similar to the average density in system B (figure 4.27). The small difference can be attributed to the internal wetting of the grey nodes which increases the ability of the system to retain water during desorption and to attract water during adsorption as previously seen in figure 4.22(b).

Moreover, the average mass at 75% RH is slightly higher in system B compared to system A. This is because there is a liquid-saturated pore in the right-bottom corner of the structure which is isolated and cannot empty in system B, but do empty in system A by means of transport through the grey nodes (figure 4.28). Furthermore, this specific pore illustrates the

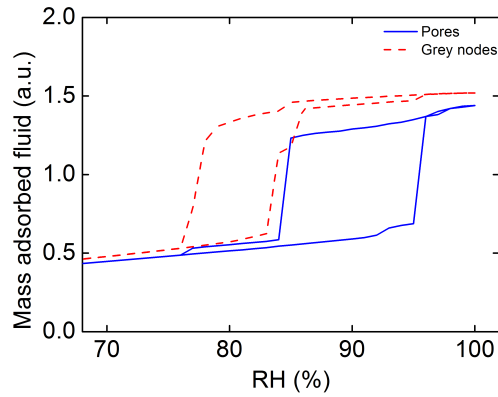


Figure 4.26: Water isotherms of system A split into two parts: pores and grey nodes.

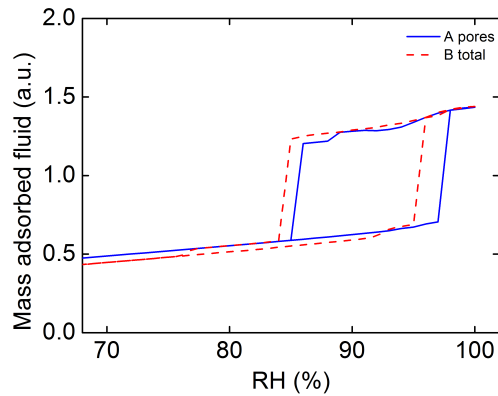


Figure 4.27: Water isotherms of the pores (without grey nodes) of system A and of system B.

inkbottle effect that was previously demonstrated in section 4.1.6 where during desorption, a pore could be blocked from emptying (at the RH expected from the Kelvin equation) until a direct liquid-free access to the vapour source is provided. However, in this case, the pore is not blocked by smaller-sized pores, but by the internal wetness of the grey nodes (figure 4.28).

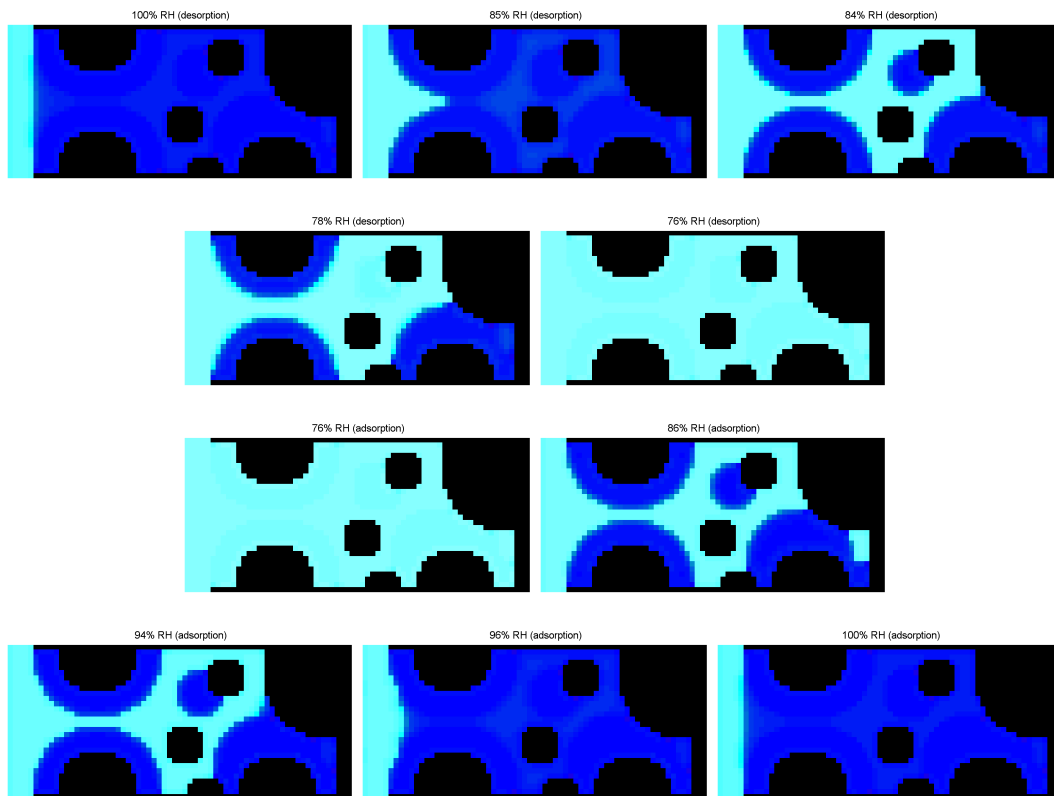


Figure 4.28: Equilibrium fluid distribution in system A (figure 4.27(a)) at critical values of the RH. Liquid is shown in blue, vapour in cyan and solids in black.

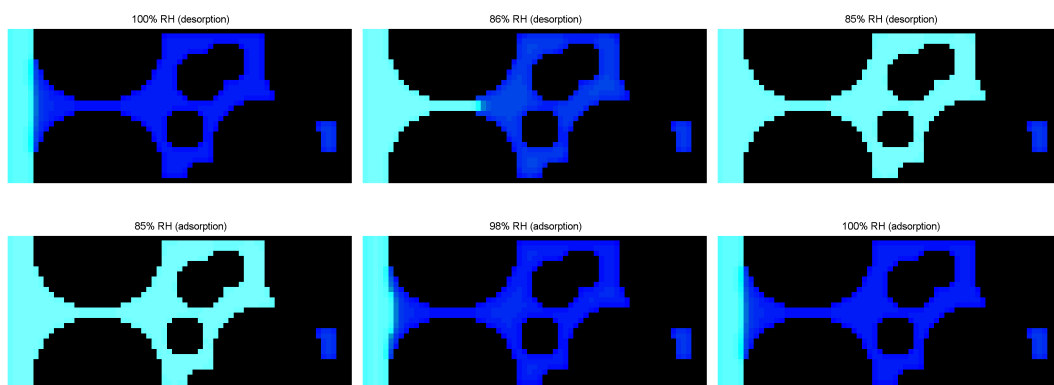


Figure 4.29: Equilibrium fluid distribution in system B (figure 4.27(b)) at critical values of the RH. Liquid is shown in blue, vapour in cyan and solids in black.

4.2.7 Conclusions

In this section, a *novel* lattice Boltzmann model was proposed, implemented within a free energy framework, and validated. The model combines the advantages of the methods presented in chapter 3 section 3.2 and in section 4.1.2 of this chapter. The model allows successful:

1. Description of the fluid with an equation of state and an implicit tracking of the liquid – vapour interfaces.
2. Description of the fluid / solid boundaries with a wetting potential that defines the contact angle.
3. Introduction of grey nodes with:
 - (a) Effective transport properties: the effective media parameter σ_{grey} is mathematically linked with the intrinsic permeability κ_{grey} of the grey nodes.
 - (b) Effective wetting properties: the internal wetting potential ϕ_{grey} is linked with the water isotherms of the grey nodes. This wetting potential could ultimately be mathematically linked with a characteristic pore size, just as the effective media parameter was mathematically linked with the intrinsic permeability.
4. Description of the interactions that arise following the introduction of grey nodes: the fluid / grey and the grey / solid boundaries are characterized with wetting potentials that define the corresponding contact angles.

Finally, the ability of the method was demonstrated in section 4.2.6 where it was applied to study the water isotherms of pseudo-random systems. The simulations captured a two-step isotherm (figure 4.25(a)) and the ink-bottle effect during desorption (figure 4.28). This ability will be further demonstrated in chapter 6 where the method will be used to model the water isotherms of 3D model microstructures of cement paste.

5 Permeability of Cement Paste

Contents

5.1 Saturated permeability of cement paste	71
5.1.1 Cement paste model microstructures	71
5.1.2 Reproducibility of the permeability	72
5.1.3 Permeability of cement paste model microstructures	73
5.1.4 Lattice magnification and microstructural resolution	75
5.1.5 Diagonal leaks	77
5.1.6 Comparison of μ_{ic} and CEMHYD3D	78
5.1.7 Comparison of μ_{ic} and HYMOSTRUC3D	78
5.1.8 Conclusions	79
5.2 Unsaturated permeability of cement paste	80
5.2.1 Cement paste model microstructures	80
5.2.2 Model microstructures at reduced degrees of water saturation	81
5.2.3 Permeating fluid: accessible pore network and permeability of the C-S-H	82
5.2.4 Apparent permeability of cement paste model microstructures	83
5.2.5 Discussion	85
5.2.6 Conclusions	86

5.1 Saturated permeability of cement paste*

5.1.1 Cement paste model microstructures

Cement paste model microstructures ($100\mu\text{m}$)³ in size were created using the vector model μ_{ic} [45, 106]. Structures were generated with water-to-cement (w/c) ratios ranging from 0.3

*The following results were published by the author in: M. Zalzale and P.J. McDonald, Lattice Boltzmann simulations of the permeability and capillary adsorption of cement model microstructures, Cement and Concrete Research, vol. 42, no. 12, pp. 1601–1610, 2012.

to 0.7 as a function of degree of hydration. The smallest and largest anhydrous particle sizes were set to 0.25 and 18 μm respectively. The model cement clinker comprised 69% alite, 10% belite, 8% ferrite, 7% aluminate, and 6% gypsum by solid mass. The reaction kinetics were defined according to Rietveld analysis results reported by Kocaba [107] for a similar cement composition. The reactant and hydrate (except C-S-H) densities were set to standard literature values [108] and are shown in table 5.1. Calculations based on the Powers-Brownnyard model [109] as reported by Taylor [108], predict that for a water-to-cement ratio of 0.4 at 85 and 95% degree of hydration, the capillary porosity is 10.7 and 5.4%, respectively. In order to match these porosities within the μic framework described above, the density of C-S-H including the gel porosity was set to $\rho_{\text{C-S-H}} = 1.965 \text{ g.cm}^{-3}$.

Table 5.1: Densities of the reactants and hydrates used for the simulation of the cement paste model microstructures.

Phase	Alite	Belite	Alumi- nate	Ferr- ite	Gyp- sum	Port- landite	C-S-H	Ettrin- gite	Mono- sulfate
Density (g.cm^{-3})	3.15	3.25	3.15	3.73	2.32	2.24	1.965	1.78	1.9

The resolution-free microstructures were subsequently translated onto cubic grids with lattice spacings of 1 μm by taking the phase present at the voxel centre as representative of the voxel (figure 5.1). The effect of this discretization on the calculated permeability will be discussed in subsequent sections. All the solids phases, including C-S-H, were treated as impermeable solids with no inherent porosity. The permeability simulations were carried out with the lattice Boltzmann algorithm presented in chapter 3 section 3.1.

Figure 5.2 shows the solid and pore volumes in a μic model cement paste with water-to-cement ratio of 0.4 at 0 and 85% degree of hydration. The capillary porosity has a significantly larger fraction of large pores than is typically measured in cement paste with, for example, mercury intrusion porosimetry. This is partly a resolution issue associated with the transfer of the resolution-free output of μic onto a discrete grid with a resolution of 1 μm .

5.1.2 Reproducibility of the permeability

The model microstructures were first verified to be representative elementary volumes (REV) by calculating the permeability of cubic structures of different side lengths (50, 100 and 120 μm). Then, to test the effect of the random initial position of the cement particles on the simulated permeability, the flow was computed in multiple test microstructures generated from different initial configurations. The resulting model microstructures have similar porosities ($\pm 0.1\%$) and the corresponding calculated permeabilities have a normalized standard deviation (standard deviation divided by average permeability) below 2%. Additionally, the isotropy of the samples was tested by computing the permeability in each of the three spatial directions. The normalized standard deviation is again less than 2%. Finally, as expected, the intrinsic

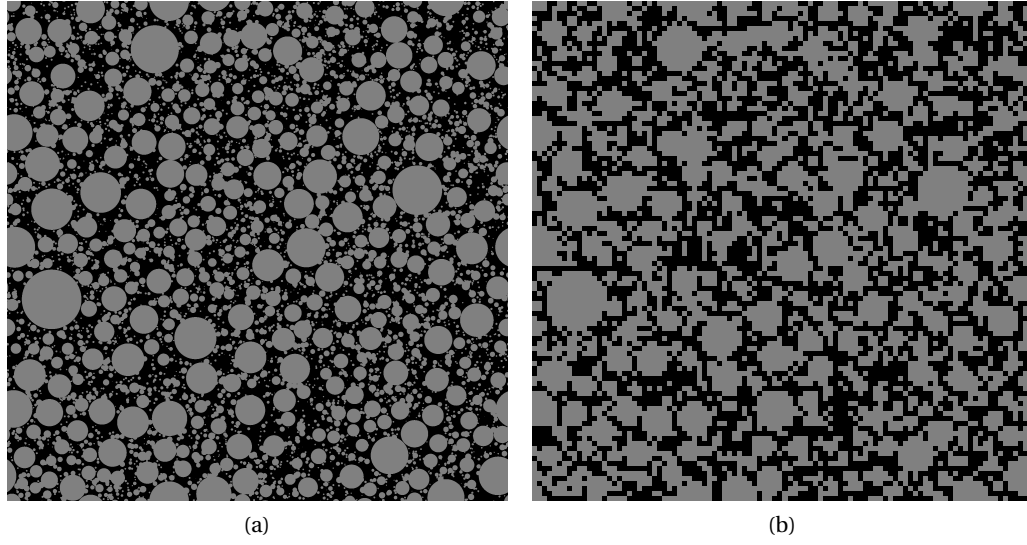


Figure 5.1: Model cement paste microstructure generated with μic (a) before and (b) after discretization with a resolution of $1 \mu m$. The side length is $100 \mu m$. The solid phases (including C-S-H) are shown in grey and the pores in black.

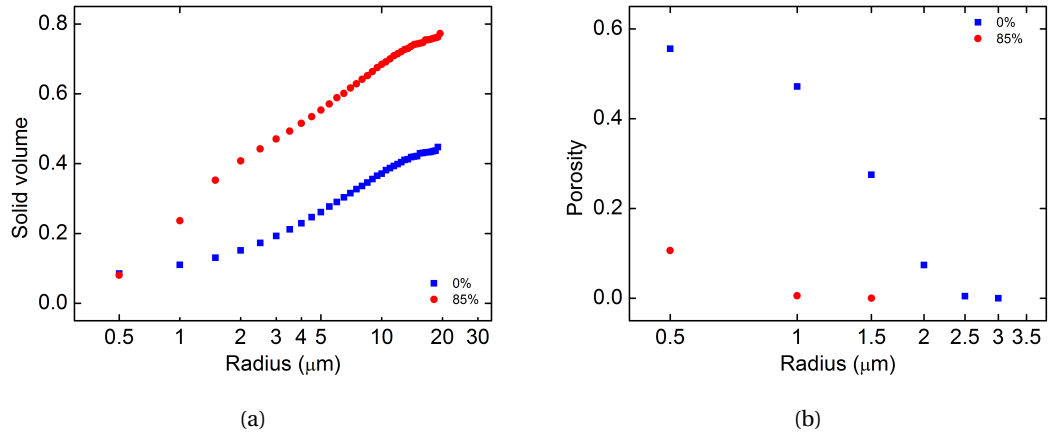


Figure 5.2: (a) Solid and (b) pore volumes in a μic model cement paste with a water-to-cement ratio of 0.4. The pore sizes were determined using a porosimetry algorithm developed by Do *et al.* [110].

permeability was verified to be independent of the value of the applied pressure gradient g .

5.1.3 Permeability of cement paste model microstructures

The permeability was computed for model cement pastes with water-to-cement ratios ranging from 0.3 to 0.7 as a function of degree of hydration (figure 5.3) and porosity (figure 5.4). The

simulations were considered converged when the mean velocity change per voxel per time step averaged over 100 time steps was smaller than 10^{-6} or after 500000 lattice time steps. This latter criterion was only required for porosities less than 11% where, in the worst case, the convergence criterion was smaller than 10^{-4} .

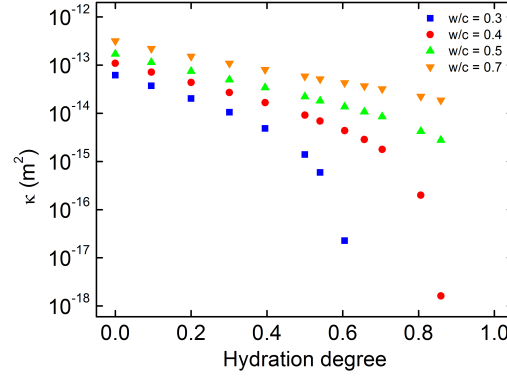


Figure 5.3: Calculated permeability *vs.* the degree of hydration for different water-to-cement ratios.

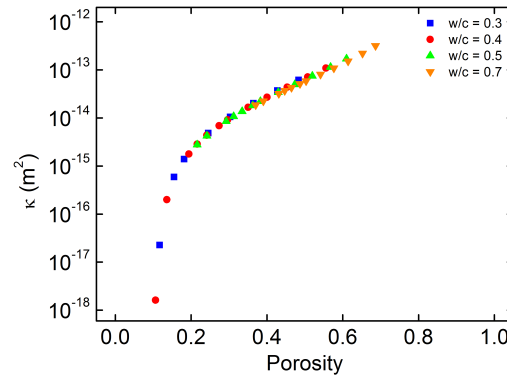


Figure 5.4: Calculated permeability *vs.* the porosity for different water-to-cement ratios.

The permeability is determined by the size and connectivity of the pores. In cement paste, on the one hand, the greater the initial water-to-cement ratio, the smaller the fraction of space occupied by hydrates, and hence the greater the permeability. On the other hand, the higher the degree of hydration, the lower the porosity, and consequently, the smaller the permeability. The permeability evolution can be divided into two regimes: above and below 20% porosity (figure 5.4). Above 20% porosity, the simulated permeabilities of all four water-to-cement ratio systems show similar behaviour. The permeabilities decrease exponentially with the degree of hydration and with broadly similar rate constants. Below 20% porosity (applicable for w/c 0.3 and 0.4), the permeability decrease is noticeably sharper. This latter dependence is attributed to the beginning of the depercolation of the capillary pores.

Although the overall trends agree with expectations, the computed permeability is larger than most experimental measurements (table 2.1). Multiple factors contribute to this:

1. The fact that the smallest pore size is only one pixel wide
2. The relatively coarse microstructural resolution of the model cement pastes
3. The influence of *diagonal leaks* in the lattice Boltzmann method
4. The assumption that the model cement pastes are fully saturated with water.

The first three topics are addressed in the following two sections. The last argument will be addressed in section 5.2.

5.1.4 Lattice magnification and microstructural resolution

In well-hydrated cement paste model microstructures, a large fraction of the pores have a diameter of one pixel (which in the previous simulations equated to 1 μm). As shown in chapter 3 section 3.1.7, the calculated permeability is overestimated by 36% in 3D pipes with side lengths of one pixel (figure 3.3).

To avoid permeability overestimation and accurately recover the hydrodynamics, the pipes should have a minimum width of four nodes (figure 3.3 and [53]). Otherwise, in complex geometries, the overestimation errors might not cancel and can add up to produce permeabilities several orders of magnitude too big. To guarantee a minimum width of four nodes, the lattice resolution should be increased four times in each of the three spatial directions (figure 5.5). This can be done without affecting the morphology or *physical* resolution of the microstructure simply by dividing every voxel into 4^3 identical voxels. The resulting lattice is 64 times larger. This modification is termed *lattice magnification* by a factor 4.

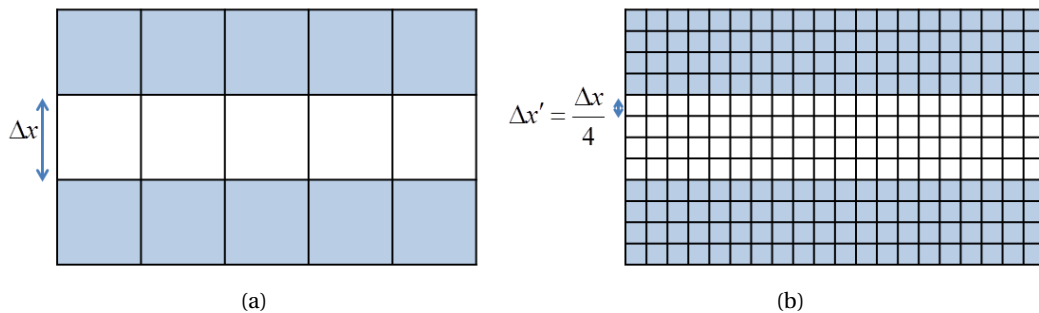


Figure 5.5: Illustration of the lattice magnification of a 2D pipe. Both structures have the same physical size but in (b) the system is magnified four times: every pixel is divided into four pixels. Pores are shown in white and solids in blue.

In parallel to the lattice magnification, the microstructure should be generated at the highest possible resolution. Since μ_{ic} is intrinsically resolution-free, the resolution limit derives from the discretization of the microstructure, and thus from the computational resources available to run the LB algorithms. This is termed *microstructural resolution*.

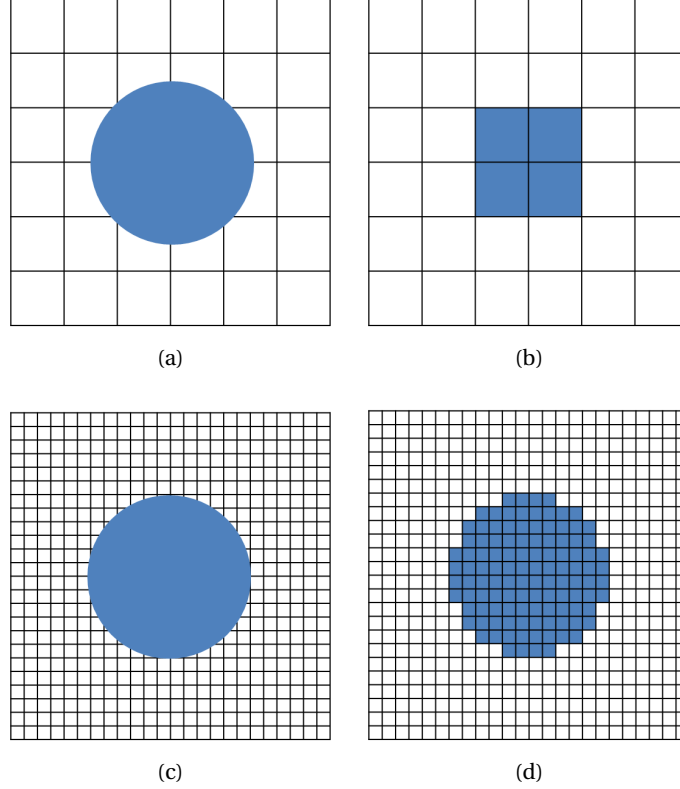


Figure 5.6: 2D illustration of the microstructural resolution: (a-b) relatively coarse and (c-d) fine discretization of a resolution-free circle. Pores are shown in white and solids in blue.

To investigate the combined effects of the lattice magnification and microstructural resolution, the permeability of a model cement paste with a water-to-cement ratio of 0.4 and a degree of hydration of 65% was computed for several lattice magnifications (1, 2 and 4) and microstructural resolutions (1, 0.5 and 0.25 μm). The porosity was kept constant at circa 21.5%. The results are shown in table 5.2.

As expected, the lattice magnification *artificially* widens the channels, allowing the LB algorithm to recover more accurate hydrodynamics. The permeability decreases as expected and as previously observed by Ferréol and Rothman on Fontainebleau sandstones [6]. The effect of the lattice magnification could not be tested for values above 4 because of computational limits. However, a lattice magnification of 4 is likely to be sufficient as previously observed on simpler geometries (figure 3.3). Also, increasing the microstructural resolution increases the structural complexity. The minimum pore diameter and thus the permeability are decreased. This too may have been expected and was previously observed in [22, 9]. What is

5.1. Saturated permeability of cement paste

Table 5.2: Computed permeabilities ($\times 10^{-16} \text{ m}^2$) for different lattice magnifications (1, 2 and 4) and microstructural resolutions (1, 0.5 and $0.25 \mu\text{m}$). The model cement paste has a water-to-cement ratio of 0.4, a degree of hydration of 65% and a porosity of 21.5%.

		Lattice magnification		
		1	2	4
Microstrutural resolution (μm)	1	28.5	10.8	2.66
	0.5	14.7	5.48	
	0.25	7.43		

less expected is that, in the range of tested parameters, both actions result in similar scaling of the permeability and that the effects are multiplicative. The same test was performed on a microstructure with a higher degree of hydration and hence a lower porosity. In this case, the effect of the lattice magnification holds but the dependence of the permeability on the microstructural resolution becomes smaller and is not quantifiable.

5.1.5 Diagonal leaks

At around 10% capillary porosity, and with a microstructural resolution of $1 \mu\text{m}$, the capillary porosity of the μic microstructures is believed to be depercolated [111]. However, it is still possible to calculate *permeability* because standard lattice Boltzmann models allow *diagonal leaks*. Diagonal leaks allow fluid to pass between neighbouring lattice points with a single edge in common as illustrated in figure 5.7. Indeed, Manwart *et al.* [76] reported a non-zero permeability for a 3D checker-board structure.

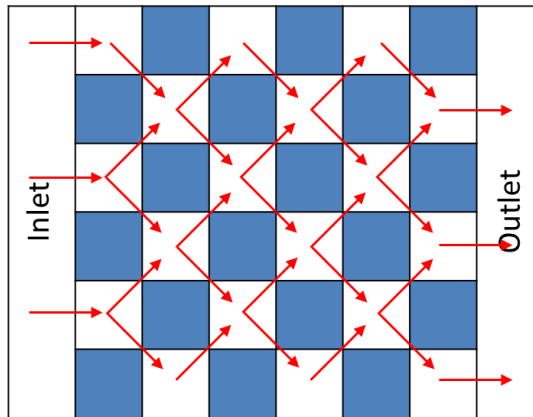


Figure 5.7: 2D illustration of diagonal leaks in a checkerboard structure. Pores are shown in white and solids in blue. The red arrows illustrate possible *leaky* paths for the fluid.

At high porosities, diagonal leaks have a negligible effect on the overall connectivity. However, near the percolation threshold, it is unclear if the diagonal leaks, or at least a fraction of the diagonal leaks, should be stopped. This can be done by applying the bounce-back rule on

leaky edges. An efficient algorithm based on look-up tables was developed to control the leaks. The algorithm successfully reduced the permeability of the checkerboard structure to zero but was not exploited any further due the choice of developing an alternative approach that will be described in section 5.2.

To conclude, in all the cement paste permeability simulations shown above, but especially at low porosities, diagonal leaks have effectively increased the pore connectivity and hence the calculated permeability. Nonetheless, with the current state-of-the-art, it is reasonable to assume that the capillary porosity of all microstructural models lacks complexity and fineness that is partially compensated by diagonal leaks in the lattice Boltzmann method, and by additional connectivity provided by gel pores in experimental measurements.

5.1.6 Comparison of μic and CEMHYD3D

It is interesting to compare the permeabilities calculated for μic microstructures with those reported for CEMHYD3D by Garboczi and Bentz [9]. Taking data at the same physical resolution ($1\ \mu m$) and lattice size (100^3) from figure 14 of [9], permeabilities of circa 8×10^{-15} and $6 \times 10^{-15}\ m^2$ are estimated at 28 and 26% capillary porosity, respectively. This is in good agreement with the permeabilities computed for μic structures of 7×10^{-15} and $4.4 \times 10^{-15}\ m^2$ at 27.4 and 24.1% capillary porosity, respectively (figure 5.4). This good agreement, however, diminishes as the capillary porosity is reduced as will be shown below.

A CEMHYD3D [44] cement paste model microstructure that mimics the lowest porosity μic structure was obtained. The microstructure is based on the Cement and Concrete Reference Laboratory Cement 152 and comprises 73.44% alite, 9.38% belite, 4.07% ferrite and 13.11% aluminate by solid volume [112]. The water-to-cement ratio is 0.4, the degree of hydration is 93.5% and the capillary porosity is 10.58%. The calculated LB permeability is $4.67 \times 10^{-17}\ m^2$. The calculated permeability for a similar μic structure with 10.64% porosity is $1.62 \times 10^{-18}\ m^2$. Clearly, while the porosities of the μic and CEMHYD3D microstructures are very similar, the permeability of the μic microstructure is one order of magnitude smaller. This is in contrast to the comparison at higher porosity (24 – 28%) where the permeabilities were very similar. One of the possible reasons for this discrepancy is the difference in the pore size distributions as CEMHYD3D has a significantly larger number of bigger pores compared to μic (figure 5.8). Also, the CEMHYD3D microstructure has around 10% more diagonal leaks. This is probably due to the discrete nature of the CEMHYD3D model where the resolution is imposed before the hydration and development of the microstructure.

5.1.7 Comparison of μic and HYMOSTRUC3D

As subsequently became apparent, Zhang *et al.* [12] were working on a parallel lattice Boltzmann study where they used a multiple-relaxation-time LB model to calculate the permeability of cement pastes simulated with the model HYMOSTRUC3D [43]. The model microstructures

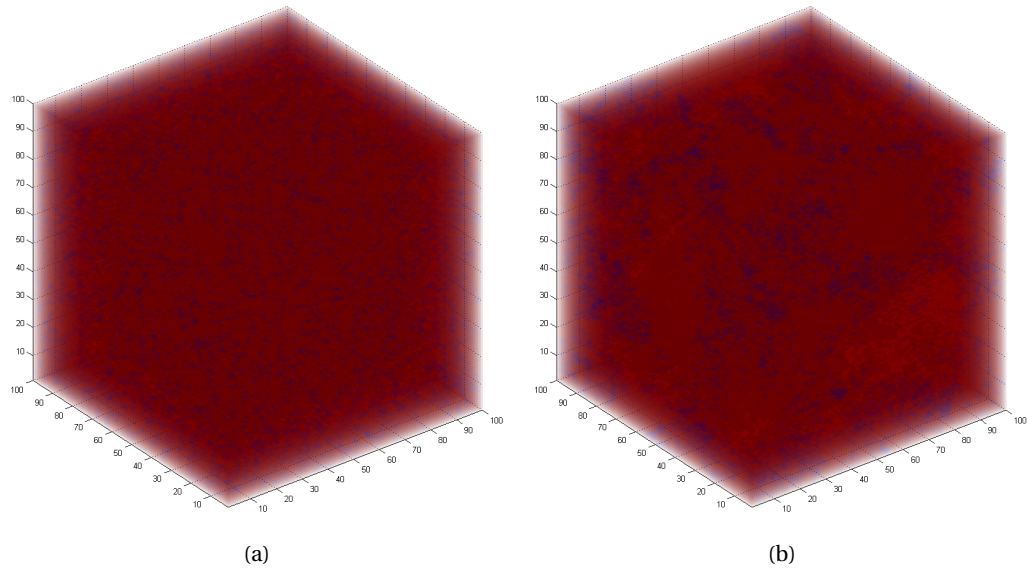


Figure 5.8: Model microstructures generated with (a) μic and (b) CEMHYD3D. Pores are shown in blue and all the solid phases in red. The microstructural resolution is $1 \mu m$.

are $(100 \mu m)^3$ in size, the microstructural resolution is $0.5 \mu m$ and there is no lattice magnification. Taking data from figure 13 of [12] at $\sim 21.5\%$ porosity, a permeability $\kappa \sim 10^{-17} m^2$ is estimated. This is two orders of magnitude smaller than the permeabilities computed at a similar porosity for a μic microstructure with the same microstructural resolution and lattice magnification (table 5.2). This discrepancy is rather surprising as in both cases the flow is simulated with an MRT lattice Boltzmann model through a microstructure essentially formed of overlapping spheres. Without the opportunity to run the lattice Boltzmann code developed in this work on the microstructures of Zhang *et al.*, or vice versa, it is very hard to explain this major discrepancy.

5.1.8 Conclusions

In general, the permeabilities calculated with lattice Boltzmann models are systematically larger than experimental measurements (table 2.1). There are three different *problems*.

First, scaling studies show the importance of the microstructural resolution [9, 10] and lattice magnification [10]. Although the LB simulations are carried out on representative elementary volumes, the required resolutions are not achieved. Consequently, the model microstructures fail to capture the pore break-through diameter [110] which is probably the most critical factor in determining permeability. The dilemma is to satisfactorily exploit the resolution-free character of the microstructural models within a discrete LB simulation. The required computational resources may become prohibitive. The issue is additionally complicated by the necessity to achieve a lattice magnification of four in order to guarantee an accurate

recovery of the hydrodynamics.

Second, the permeability is critically dependent on the overall size and connectivity of the micron-sized capillary pores. These variables are dependent on the density of the C-S-H which remains a point of active discussion. The main question concerns the assignment of porosity either to the nano-scale gel pores or to the larger micron-scale capillary pores. There is recent nuclear magnetic resonance evidence for smaller fractions of capillary porosity than traditionally thought [3]. Fewer capillary pores place a greater fraction of the water in the gel porosity, reduce the overall capillary porosity, and hence decrease the model permeability. However, at realistic microstructural resolutions, a lower capillary porosity would result in a depercolated pore network and hence an unmeasurable permeability. Therefore, to be able to calculate permeability at lower capillary porosities, the C-S-H gel pores must be taken into account. However, in addition to the unrealistic computational requirements, there is the immediate limitation that experimental techniques and microstructural models do not reveal the 3D structure of the C-S-H [113, 114, 3, 115]. To bypass this problem, a different approach may be to include the C-S-H as an effective medium with effective transport properties as will be shown in section 5.2.

Finally, all the simulations shown above and in [9, 12] do not take into account the degree of water saturation of the samples. This parameter was proven to be critical in experimental measurements of the gas permeability of cementitious materials [31, 33, 32] and will be further discussed in section 5.2.

5.2 Unsaturated permeability of cement paste[†]

5.2.1 Cement paste model microstructures

New cement paste model microstructures $(100\text{ }\mu\text{m})^3$ in size were created using the vector model μic [45, 106]. The structures had an initial water-to-cement ratio of 0.4 and were generated as a function of the degree of hydration. Except when stated otherwise, the smallest and largest anhydrous particle sizes were set to 0.5 and 20 μm respectively, the former corresponding to the microstructural resolution and the latter to 20% of the structure size.

The phase composition of the model cement clinker was 51.9% alite, 23.1% belite, 8.1% ferrite, 9.8% aluminates, and 7.1% gypsum by solid mass. The reaction kinetics were defined according to the hydration model of Parrot and Killoh [116]. The densities of the reactants and hydrates were set to standard literature values [108] as previously shown in table 5.1. It is worth noting that the density of the C-S-H, previously calculated in order to match the capillary porosity of the Powers-Brownyard's model [109], do match the recent findings of Muller *et al.* [3] as measured using ^1H nuclear magnetic resonance (NMR) relaxation analysis. The phase

[†]The following results were published by the author in: M. Zalzalé, P.J. McDonald, and K.L. Scrivener, A 3D lattice Boltzmann effective media study: understanding the role of C-S-H and water saturation on the permeability of cement paste, *Modelling and Simulation in Materials Science and Engineering*, vol. 21, no. 8, p. 085016, 2013.

composition of the hydrated microstructure was verified and found to be in good agreement with thermodynamic calculations determined using the Gibbs Energy Minimization Software for Geochemical Modeling [117].

Muller *et al.* [3] recently measured the total capillary porosity of a 28 days old white cement paste with a water-to-cement of 0.4 using a combination of ^1H NMR relaxation analysis and chemical shrinkage experiments. They reported a total capillary porosity of 9.2%, consistent with the capillary porosity predicted by Powers and used in section 5.1. Accordingly, the model microstructures with 9.2% total capillary porosity, corresponding to a degree of hydration of 89%, were selected for further analysis and subsequent permeability simulations.

First, these resolution-free microstructures were discretized onto cubic grids of 200^3 voxels with a microstructural resolution of $0.5\ \mu\text{m}$ by taking the phase present at each voxel centre as representative of that voxel. Second, as shall be seen below, the model structures were *adapted* in order to have reduced degrees of water saturation. Third, the penetrating fluid (liquid water or gas) was chosen and the permeability of the C-S-H was set accordingly. Finally, the lattice Boltzmann model described in chapter 3 section 3.2 was used to simulate the flow through the partially-saturated cement paste model microstructures that contained capillary pores, weakly-permeable or impermeable C-S-H, and solid inclusions.

5.2.2 Model microstructures at reduced degrees of water saturation

The capillary porosity of mature cement pastes can be largely devoid of liquid water. For example, Muller *et al.* [3] recently showed by ^1H NMR relaxation analysis that for a sealed-cured 28 days old white cement paste with a water-to-cement ratio of 0.4, out of the 9.2% total porosity, only 1.4% is water-filled. The remaining 7.8% are *empty* chemical shrinkage voids. They further showed that it is difficult to subsequently refill these voids [35].

The modelling platform *μic* generates the microstructure of the solid phases. It is usually assumed that the remaining space is filled with water. This is equivalent to an *ideal* underwater curing. To model permeability as a function of capillary water saturation, water was removed progressively from the model microstructures, starting from the largest pores according to the Kelvin-Laplace law, as illustrated in figure 5.9. The largest pores were determined using a porosimetry algorithm developed by Do *et al.* [110]. To avoid systematic bias due to the pore-emptying algorithm, multiple repeats of the algorithm were run, in which the order that pores of any given size were emptied was randomly chosen. This process yielded multiple partially saturated structures with the same saturated pore size distribution originating from a given saturated parent structure. The process was repeated for different parent structures all with the same overall capillary porosity (9.2%).

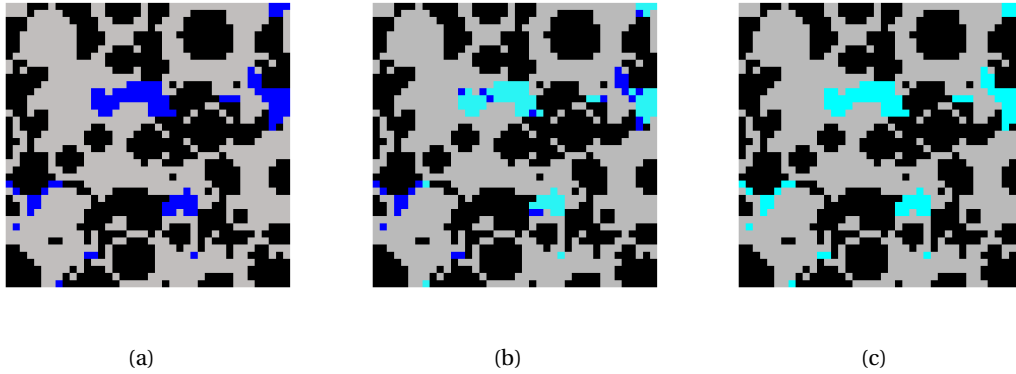


Figure 5.9: A 40^2 pixels slice of a 200^3 voxels μm model cement paste microstructure at different degrees of water saturation. Solid impermeable phases are shown in black, C-S-H in grey, emptied capillary pores in cyan and water-filled capillary pores in blue. In (a) the capillary porosity is fully saturated with water; in (b) it is partially saturated and in (c) it is empty of water and fully saturated with gas.

5.2.3 Permeating fluid: accessible pore network and permeability of the C-S-H

For the simulation of permeability with water as the penetrating fluid, the solid phases and *emptied* pores were considered impermeable to liquid water, so that the degree of water saturation remains constant during the flow simulations. Powers gave the coefficient of water permeability of the C-S-H gel as $7 \times 10^{-23} \text{ m}^2$ [118]. This permeability was assigned to all the C-S-H nodes by considering them as grey nodes, as defined in chapter 3 section 3.2, and through application of equation 3.32 so that the effective media parameter is $\sigma_{C-S-H} = 1 - 3.36 \times 10^{-9}$ when the microstructural resolution and the LB lattice unit Δx are equal to $0.5 \mu\text{m}$. As this is the only value that could be found in literature, the dependency of the bulk permeability on the C-S-H permeability was investigated by increasing and decreasing the latter by a factor of 10. For the simulation of permeability with gas as the penetrating fluid, the solid phases and liquid water were considered impermeable to gas. Additionally, the C-S-H was considered *wet* and hence impermeable to gas. Table 5.3 summarizes the setup of the simulations.

Table 5.3: Permeability to water and gas of the different cement paste phases.

Permeating fluid	Solid phases	Water-filled capillary pores	Empty capillary pores	C-S-H
Water	Impermeable	Calculate with LB	Impermeable	70, 7 and $0.7 (\times 10^{-23} \text{ m}^2)$
Gas	Impermeable	Impermeable	Calculate with LB	Impermeable

5.2.4 Apparent permeability of cement paste model microstructures

Figure 5.10(a) shows the cement paste *apparent* intrinsic permeability with water as the permeating fluid as a function of the degree of water saturation of the capillary porosity for $\kappa_{C-S-H} = 7 \times 10^{-23} \text{ m}^2$. The graph also shows the gas permeability for the structures in which the fluid-accessible pore space comprises the larger emptied capillary pores and the C-S-H is impermeable, mimicking a gas permeability experiment. Figure 5.10(b) shows selected experimental cement paste permeabilities taken from table 2.1 and the references therein.

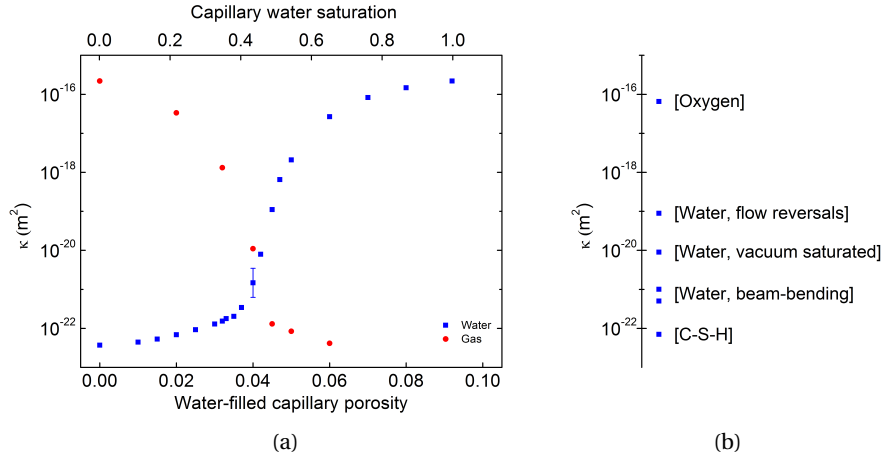


Figure 5.10: (a) Simulated *apparent* intrinsic permeability κ vs. the degree of water saturation. The penetrating fluid is water or gas. The model cement paste water-to-cement ratio is 0.4 and the capillary porosity corresponding to full saturation is 9.2%. An exemplar error bar (mean \pm standard deviation) is shown close to the depercolation threshold. Away from the depercolation threshold, water-filled porosity less than 0.035 or greater than 0.05, the error bar is smaller than the symbol size. (b) Experimental cement paste permeabilities from table 2.1, from top to bottom: Wong *et al.* [4], Banthia & Mindess [21], Ye [22], Vichit-Vadakan & Scherer [25, 26], Vichit-Vadakan & Scherer [25, 26] and Powers [118].

Close to 50% water saturation, the convergence criterion, as defined in chapter 3 section 3.2.4, was not always reached. In these cases, the simulations were stopped after one million time steps and the relative change in permeability per 1000 time steps was typically 10^{-4} . The standard deviation of the water permeability was calculated from multiple runs of the simulation. It comprises two parts: the first is variability in the parent structure (initial anhydrous cement particles positions) and the second is variability in the water distribution within a given structure. The variation is negligible when the structures are highly saturated with a fluid and highest near the depercolation threshold. An exemplar standard deviation is shown on figure 5.10(a) near the depercolation threshold for a confidence interval of 68.2% (mean \pm standard deviation). The distribution width of the simulated water permeability of nominally similar samples is comparable to what is observed experimentally (table 2.1).

To test the effect of microstructural resolution on permeability, further structures were gener-

ated with a smaller minimum anhydrous cement particle size and a microstructural resolution and lattice spacing of $0.25 \mu\text{m}$. As discussed in section 5.1.4, the structural complexity increases when the minimum particle size decreases. At full water saturation, the water permeability decreases by circa 3.5 times in agreement with previous observations [10, 9]. However, compared to the six orders of magnitude spanned by the data, this now seems a small factor. Moreover, the water permeability is insensitive to resolution for structures with no water-filled capillary porosity.

To test the effect of the C-S-H permeability on the water permeability of the paste, simulations were re-run using $\kappa_{C-S-H} = 7 \times 10^{-22} \text{ m}^2$ and $\kappa_{C-S-H} = 7 \times 10^{-24} \text{ m}^2$. The results are shown in figure 5.11. As expected, changing the C-S-H permeability has no effect on the water permeability for structures with high water saturation since the water-filled capillary porosity is percolated and $\kappa_{C-S-H} \ll \kappa_{paste}$. The effect of the C-S-H permeability on the water permeability of the paste amplifies with decreasing water saturation. At 1.5% water-filled capillary porosity, increasing the C-S-H permeability by a factor of 10 increases the water permeability by a factor ~ 7 , while decreasing the C-S-H permeability by 10 decreases the water permeability by ~ 3 times only. At zero water-saturation, the effect of the C-S-H permeability on the paste permeability becomes linear so that the modelled water permeabilities are 3.7×10^{-22} , 3.7×10^{-23} and $3.7 \times 10^{-24} \text{ m}^2$ for structures with C-S-H permeabilities of 7×10^{-22} , 3.7×10^{-22} and $3.7 \times 10^{-23} \text{ m}^2$ respectively. These values are consistent with the idea that the C-S-H occupies approximately half of the volume of the cement paste and could have been calculated by assuming a parallel flow in a medium composed of 50% C-S-H and 50% solids as shown in chapter 3 section 3.2.5.

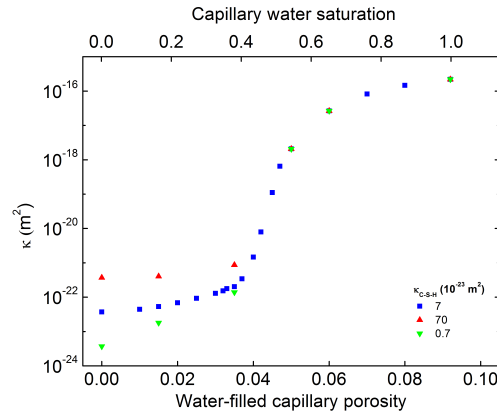


Figure 5.11: Simulated *apparent* intrinsic permeability κ *vs.* the degree of capillary water saturation for different values of the C-S-H permeability. The penetrating fluid is water.

5.2.5 Discussion

The intrinsic permeability of the structure fully saturated with water is conceptually[‡] the same as the intrinsic permeability of a completely dried cement paste saturated with gas in an ideal gas permeability experiment. It is therefore not surprising that, at high degrees of water saturation, the water permeability is comparable to the oxygen permeability results of Wong *et al.* [4]. Practically, a better comparison is with the simulation of the sister structure saturated with gas (zero water saturation) since, in most laboratory gas experiments, the C-S-H is not fully dried and is therefore impermeable to gas. In both cases, when the capillary porosity is highly saturated with a fluid, the role of water within the C-S-H in determining permeability is minimal as the flow is mainly controlled by the percolated fluid-filled capillary pores.

By gradually reducing the water saturation, the water permeability decreases. Initially the decrease is slow. Below 60% capillary water saturation, the water permeability decreases more rapidly as the water-filled capillary porosity starts to depercolate. A very sharp drop in water permeability is observed between 50 and 40% water saturation regardless of the C-S-H permeability. This is in agreement with the findings of Elam *et al.* [119] who reported depercolation of the void regions between mono-sized overlapping spheres at around 3.2% void. When the water-filled capillary porosity is depercolated, the influence of flow through the weakly-permeable C-S-H is amplified because the flow is then mainly controlled by the weakly-permeable C-S-H. The water permeability ranges from approximately 10^{-19} to 10^{-22} m². This agrees well with the range of experimental water permeability measurements as shown in table 2.1. It is therefore interesting to consider the likely degree of water saturation of the samples in those experiments.

In the case of Ye [22], paste samples were sealed cured for 28 days and then vacuum saturated with water for 4 to 8 hours before the water permeability measurement. Muller [35] reports that for a 28 day sealed cured sample that was subsequently vacuum saturated for 24 hours, the water-filled capillary porosity rose from 1.4 to 5.5% as measured by NMR. Since Ye's samples were vacuum saturated for a shorter time, a slightly smaller water-filled fraction should be expected. In agreement with this expectation, the water permeability measurement of Ye, 9.0×10^{-21} m², is matched by a water permeability simulation with approximately 4.3% water-filled capillary porosity for Powers measured value $\kappa_{C-S-H} = 7 \times 10^{-23}$ m².

Vichit-Vadakan and Scherer [25] used the beam-bending method to measure water permeability in a range of samples of different sizes that were cured sealed for 48 hours and then further cured underwater. Permeability is derived from the rate of relief of pressure required to bend a water saturated sample. To verify that the samples were fully saturated, they compared the permeability before and after pressurization underwater at 2 MPa for 24 hours. The authors concluded that small samples were fully saturated prior to pressurization on the basis of constancy of the permeability but that this was not the case for larger samples. However, a careful examination of their figure 4 reveals that permeability decreased after pressurization by about

[‡]The intrinsic permeability is independent of the permeating fluid.

20% for the smallest samples (5.7 mm) and by about 60% for slightly larger samples (7.7 mm). As they suggest, one possible interpretation for higher permeability values before pressure saturation is the relief of internal pressure by water flow into nearby air voids. We suggest that even the small samples may not have been fully saturated before pressurization. Moreover, those few samples that were subjected to pressurization may not have been fully saturated either. Using the experimentally measured permeability and a pressure of 2 MPa, Darcy's law suggests that several days are required to fill the void spaces created during the preliminary 48 hours of sealed curing, rather than the single day allowed, even for the small samples. In the LB simulations, the water permeability matches the experimental measurements of Vichit-Vadakan and Scherer 5×10^{-22} to 10^{-21} m² between 4 and 4.2% water-filled capillary porosity again for $\kappa_{C-S-H} = 7 \times 10^{-23}$ m².

Overall, the effect of the C-S-H on the simulated permeability is partially seen in the detail of the asymmetry of the *liquid* and *gas* curves in figure 5.10(a). This is because the C-S-H is considered permeable in the former case, and impermeable in the latter. However, it is not the full story, since the asymmetry is also due to the fact that at water saturation S_w , the liquid occupies a different pore network (predominantly small pores) compared to the gas (large pores) at saturation $(1 - S_w)$. The role of the C-S-H amplifies as the capillary porosity starts to depercolate. This is unequivocally seen by comparing the current results with previous LB water permeability simulations that treated the C-S-H as impermeable solid as seen in section 5.1 and in [10, 9, 12]. In those calculations, as the porosity decreased by increasing the degree of hydration, the permeability decreased monotonically and catastrophically close the percolation threshold, below which it could not be calculated accurately and was mainly a result of diagonal leaks. Now, however, the asymptotic approach towards a plateau permeability dictated by the C-S-H is clearly seen.

5.2.6 Conclusions

This chapter addressed the shortcomings of the standard lattice Boltzmann methods as discussed in the conclusions of section 5.1. This chapter also allowed insights to be gained on the possible reasons behind the large scatter in experimental measurements of the permeability of cement paste.

First, the effective media lattice Boltzmann approach proved to be well suited to numerical calculation of permeability within complex multi-scale 3D cement paste microstructures including capillary pore regions of defined geometry, calcium silicate hydrate regions of defined permeability, and impermeable solid inclusions. This is an advance over previous numerical simulations of permeability in cement paste where only the capillary pore network was considered, and further this was fully saturated.

The simulation of *apparent* intrinsic permeability at different degrees of water saturation provides a very plausible explanation for the enormous range of experimental results. The results also explain the apparently large values of water permeability reported in previous

simulations without invoking earlier arguments of limited spatial resolution either in the microstructure or in the lattice Boltzmann solver. It is now clear that the large permeability is a direct consequence of the percolation of the capillary pore network at full water saturation. The suggestion is that most experimental measurements with water are not conducted on fully saturated samples. The presence of air voids in nominally water saturated samples could lower dramatically their *apparent* intrinsic permeability. It is further concluded that the role of the weakly-permeable C-S-H, omitted in earlier modelling studies, is critical and has a non-linear effect on the permeability of cement paste.

Finally, while both liquid water and gas permeabilities were calculated, a multi-phase fluid with an equation of state that links liquid water and vapour is yet to be incorporated in the lattice Boltzmann model. This modification would remove the necessity for the assumption that the degree of water saturation remains constant during the flow simulations. A multi-phase model was introduced in chapter 4 and is the subject of the following chapter where the objective is to study the adsorption and desorption of water and vapour in model cement pastes.

6 Water Isotherms of Cement Paste

Contents

6.1 Water isotherms of cement paste	89
6.2 Model water isotherms of the capillary pores	90
6.2.1 Previous work	90
6.2.2 Reproduction of previous work	91
6.3 Model water isotherms of the capillary and C-S-H gel pores	93
6.4 Discussion: Kelvin's equation, a critical limitation in the model isotherms	98
6.5 Conclusions	99

6.1 Water isotherms of cement paste

The water isotherms are obtained by plotting the water content in the material *vs.* the relative humidity (RH) at equilibrium and constant temperature. For cement paste, the time to reach each equilibrium step depends on many factors including the specimen thickness and the RH gradient and ranges to well over a year [120] even for thin sub-centimetre samples. Figure 6.1 shows the desorption and adsorption isotherms of a white cement paste with a w/c ratio of 0.4 as obtained using ^1H NMR analysis. The isotherms of cement paste display considerable hysteresis between desorption (drying) and adsorption (wetting). The hysteresis is often attributed to the capillary condensation and the ink-bottle effect (see chapter 4 section 4.1.6 for a discussion on the ink-bottle effect).

Recently, Muller *et al.* [121] used ^1H NMR relaxation analysis to split the desorption isotherm into several pore-type resolved isotherms. In summary, the capillary pores empty in the RH range 100 – 85%. The C-S-H gel pores follow over a wider range of RH such that by about 30% RH, cement paste is considered to be dry, save for some residual water adsorbed on the surfaces of the C-S-H. This too is removed at still lower RH. From an engineering perspective, it is the transport and condensation occurring over the middle and upper ranges of RH conditions that are important because they correspond to many temperate parts of the world.

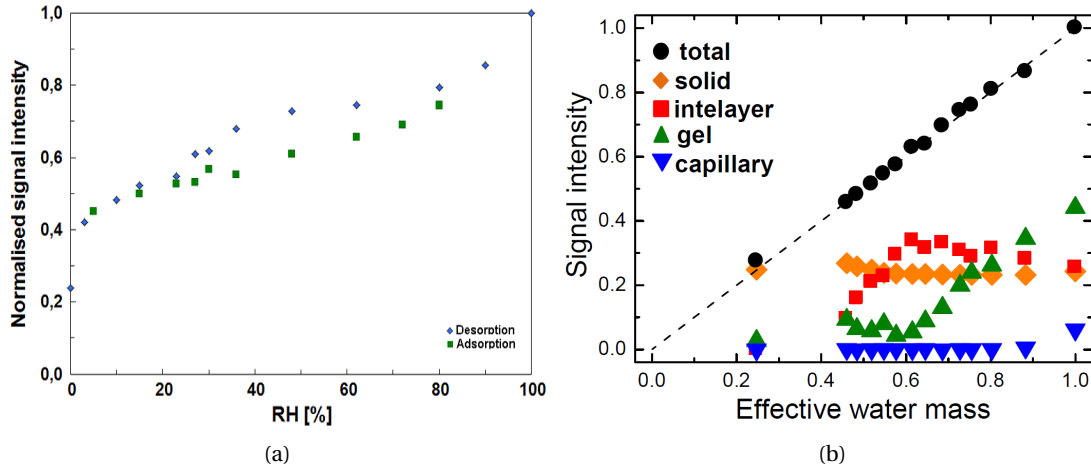


Figure 6.1: (a) Water desorption and adsorption isotherms and (b) pore-resolved desorption isotherm for a cement paste with a w/c ratio of 0.4 as obtained using ^1H NMR analysis. Data from Agata Gajewicz.

6.2 Model water isotherms of the capillary pores

6.2.1 Previous work

A standard free energy lattice Boltzmann algorithm, similar to the one described in chapter 4 section 4.1, was previously used in [10]* to study the desorption and adsorption of water and vapour in three-dimensional model cement pastes generated with the platform μic . The model cement paste had a water-to-cement ratio of 0.4 and the same chemical composition and parameters as those used in chapter 5 section 5.1. The test microstructures were $16 \times 7.5 \times 7.5 \mu\text{m}^3$ in size, had a microstructural resolution of $0.5 \mu\text{m}$, a lattice magnification of two, and a capillary porosity of 22%. The reduced temperature was $\theta/\theta_c = 0.96$ leading to a liquid density of $\rho_{\text{liquid}} = 1.41$ and a gas density of $\rho_{\text{gas}} = 0.62$. The liquid – vapour interfaces had a width of $\varpi = 1$ and the liquid – solid interfaces were characterized with a contact angle of $\Theta = 45^\circ$. The desorption and adsorption isotherms are shown in figure 6.2 where the shaded region shows the variation (standard error in the mean) in simulations carried out on different test microstructures.

The isotherms show considerable hysteresis indicating the occurrence of capillary condensation [10]. There are a number of steps at which pores of a specific size empty. Small pore throats retain liquid water down to $\sim 87\%$ RH at which point they dry out and the liquid water in larger pores behind rapidly follows. On the adsorption path branch, these pores do not refill until circa 96% RH. The simulations show that there are a handful of isolated pores which do not empty.

*[10] was a collaborative study where the present author was primarily responsible for the permeability simulations and Peter McDonald was primarily responsible for the desorption simulations.

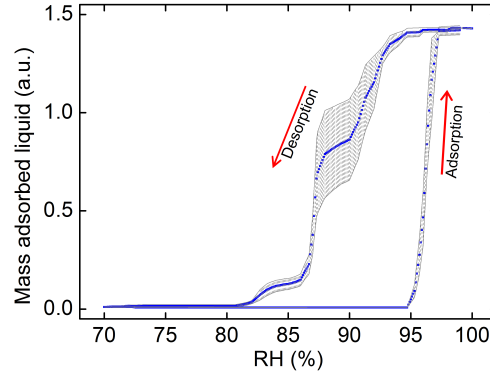


Figure 6.2: Simulated desorption and adsorption isotherm for a model cement paste generated with μic with a microstructural resolution of $0.5 \mu m$. The shaded region shows the variation (standard error in the mean) in simulations carried on different test microstructures.

It was confirmed in [10] that there are several issues that need to be addressed in order to quantitatively match the experimental measurements. Most importantly, the width of the pore size distribution must be increased in order to avoid the dramatic desorption step at around 90%. Also, the C-S-H gel porosity needs to be resolved within the microstructural model in order to avoid the false conclusion that the sample is devoid of liquid water by circa 80% RH [10]. Hence, it was concluded that although the model can *qualitatively* reproduce the early part of the water isotherms related to the capillary porosity as reported in literature [122, 120, 114], considerable work is required to parameterize it in order to *quantitatively* match the experiments.

6.2.2 Reproduction of previous work

In this section, the cement paste water isotherms calculated in [10] are compared with those calculated in this work by the present author. Hence, the free energy model described in chapter 4 section 4.1.4 was used to calculate the water isotherms of model cement pastes. The cement paste and LB parameters were described in [10] and in section 6.2.1. Figure 6.3 shows the isotherms calculated in this work and in [10]. The two isotherms are not identical and there are several reasons for that.

First, the isotherms in [10] were calculated on test structures that were *randomly* selected from one larger microstructure. Hence, in this work, the isotherms were calculated on similar, but not strictly the same, microstructures.

Second, figure 6.3 shows a substantial difference in the mass of adsorbed fluid. This is because the mass of adsorbed fluid was calculated in [10] as the total liquid mass divided by the volume of pores. This is slightly different to the method used in this work, as explained in chapter 4 section 4.1.5, where the mass of adsorbed fluid is calculated as the average density in the

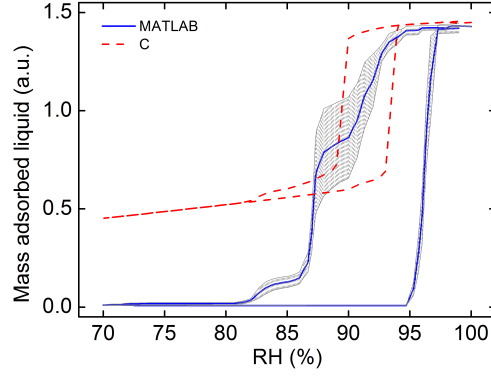


Figure 6.3: Comparison of the water isotherms as calculated in [10] (MATLAB) and with the version implemented by the author and used in this work (C).

fluid nodes. It is believed that the approach used in this work is more appropriate for later comparisons with experimental data where the measurable quantity is the total mass of the system.

Third, figure 6.3 shows a difference in the relative humidity at which the main drying and wetting steps take place. The difference in the drying step is within the scatter but the difference in the wetting step is not. This is because in [10], the term describing the liquid – vapour interfaces, χ , was erroneously divided by two. Figure 6.4 shows that re-running the simulations with $\chi' = \chi/2$ leads to an isotherm with the main wetting step occurring at higher relative humidities. However, it is uncertain why the change in χ affects only the adsorption branch of the curve. It seems very likely that in such a complex structure, the desorption is highly perturbed and mostly controlled by the ink-bottle effect.

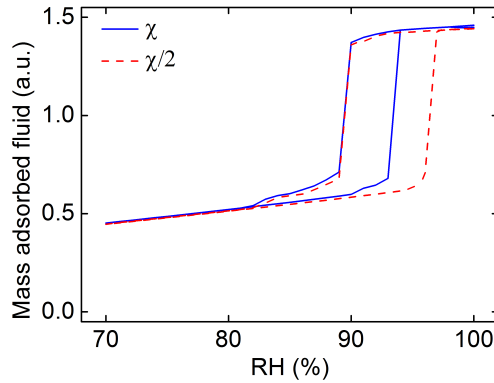


Figure 6.4: Effect of χ on the simulated water isotherms

Finally, because of major performance improvements, the isotherms calculated in this work have a better (lower) convergence criterion. This results in a more step-like curve when compared to [10].

6.3 Model water isotherms of the capillary and C-S-H gel pores

The water isotherms calculated in [10] and shown in figure 6.2 are, to the best knowledge of the authors, the first numerical isotherms calculated for an *explicitly-resolved* microstructure of cement paste. However, these simulations were limited to the capillary pores. The aim of this section is to extend the previous simulations to include the C-S-H gel pores. This is done by using the lattice Boltzmann free energy effective media approach developed in chapter 4 section 4.2. The novel contribution of this section is the treatment of the C-S-H as a *grey* material with effective transport and wetting properties.

Three-dimensional model cement pastes, as previously described in chapter 5 section 5.2, were used. The test microstructures were $30 \times 30 \times 15 \mu\text{m}^3$ in size, had a microstructural resolution of $0.5 \mu\text{m}$, a lattice magnification of two, and a capillary porosity of 9.2%. The test structures were 15 times bigger than those investigated in [10] following major performance improvements of the code. Figure 6.5 shows a 2D slice of the 3D μic microstructure described above. The reduced temperature was $\theta/\theta_c = 0.96$ leading to a liquid density of $\rho_{liquid} = 1.41$ and a gas density of $\rho_{gas} = 0.62$. The liquid – vapour interfaces had a width of $\varpi = 1$. The pressure scaling factor was set to $\xi = 0.3$ in order to improve numerical stability. To accelerate the convergence of the simulations, the samples were surrounded with sources of RH in the three spatial dimensions.

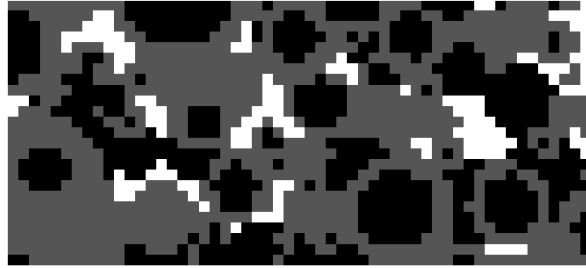


Figure 6.5: Two-dimensional slice of a 3D μic microstructure. The capillary pores are shown in white, the C-S-H in grey and the solids in black.

Each C-S-H node was considered a grey node with an effective media parameter of $\sigma_{C-S-H} = 0.01^\dagger$ and an internal wetting potential $\phi_{C-S-H} = 0.27$. The fluid – solid wetting potential was set to $\phi_{fluid/solid} = 0.23$ in order to return a liquid – solid contact angle of $\Theta = 30^\circ$. This is believed to be the upper limit for the contact angle which is usually assumed to be between 0 and 30° [123]. The additional interface wetting potentials were set to $\phi_{fluid/C-S-H} = 0.23$ and $\phi_{C-S-H/solid} = 0.27$ in order to return contact angles of $\Theta_{fluid/C-S-H} = 30^\circ$ and $\Theta_{C-S-H/solid} = 0^\circ$, respectively.

[†]It was previously shown in chapter 4 section 4.2.5 that the effective media parameter (and hence the permeability) of the grey nodes has no effect on the simulated isotherms as long as the nodes are permeable.

Figure 6.6 shows the calculated desorption and adsorption isotherms where the mass of adsorbed fluid is normalized by the pore volume. The figure also shows the contribution of each of the two pore networks separately (capillary pores and C-S-H nodes).

The isotherms have two main steps as it can also be seen from the equilibrium fluid distributions shown in figures 6.9 and 6.10. The capillary pores start emptying at 100% but the most considerable step happens between 90 and 75% RH. The C-S-H gel pores empty between 80 and 70% RH and the isotherms are remarkably similar to the intrinsic isotherms of grey nodes characterized with the same internal wetting potential as previously shown in chapter 4 figure 4.22. This suggests that the degree of internal wetting ϕ_{C-S-H} can indeed characterize the C-S-H with a *relatively intrinsic* isotherm that is, as it should be, only very slightly affected by the presence of neighbouring solid and fluid nodes.

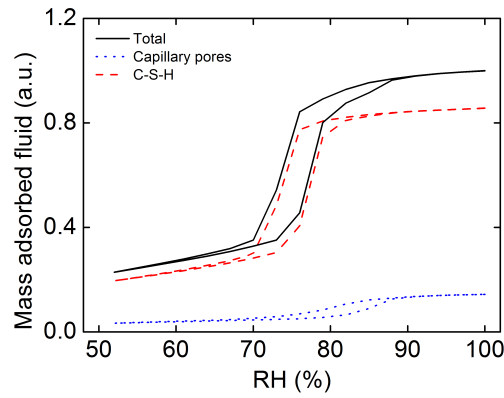


Figure 6.6: Model water isotherms of the capillary and gel pores of cement paste. The mass of adsorbed fluid is normalized the pore volume (capillary pores and C-S-H nodes). The internal wetting potential of the C-S-H is $\phi_{C-S-H} = 0.27$.

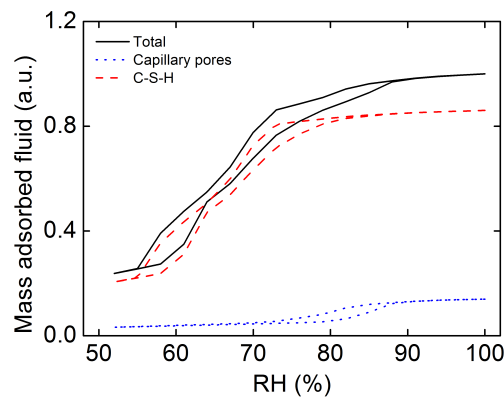


Figure 6.7: Model water isotherms of the capillary and gel pores of cement paste. The mass of adsorbed fluid is normalized the pore volume (capillary pores and C-S-H nodes). The internal wetting potential of the C-S-H is $\phi_{C-S-H} = 0.54$.

6.3. Model water isotherms of the capillary and C-S-H gel pores

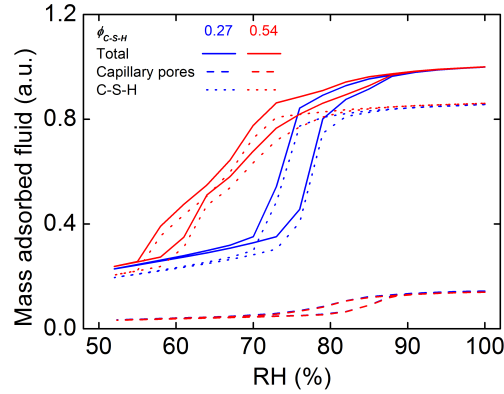


Figure 6.8: Effect of the internal wetting of the C-S-H on the model isotherms of cement paste. Data from figures 6.6 and 6.7.

Figure 6.7 shows the water isotherms for the system described above but with an increased C-S-H wetting potential from $\phi_{C-S-H} = 0.27$ to $\phi_{C-S-H} = 0.54$. Figure 6.8 shows the effect of the internal wetting potential of the C-S-H on the water isotherms by comparing figures 6.6 and 6.7. When the internal wetting potential of the C-S-H is increased, the RH's of desorption and adsorption of the C-S-H decrease. This is because, as previously discussed in chapter 4 section 4.2.5, the C-S-H with the highest wetting potential retains the liquid fluid for longer when the surrounding RH is decreased and starts adsorbing the liquid fluid earlier when the surrounding RH is increased. However, the internal wetting of the C-S-H has a negligible effect on the isotherms of the capillary pores. This is because at 9.2% capillary porosity, save for very few isolated pores, most of the capillary pores are percolated.

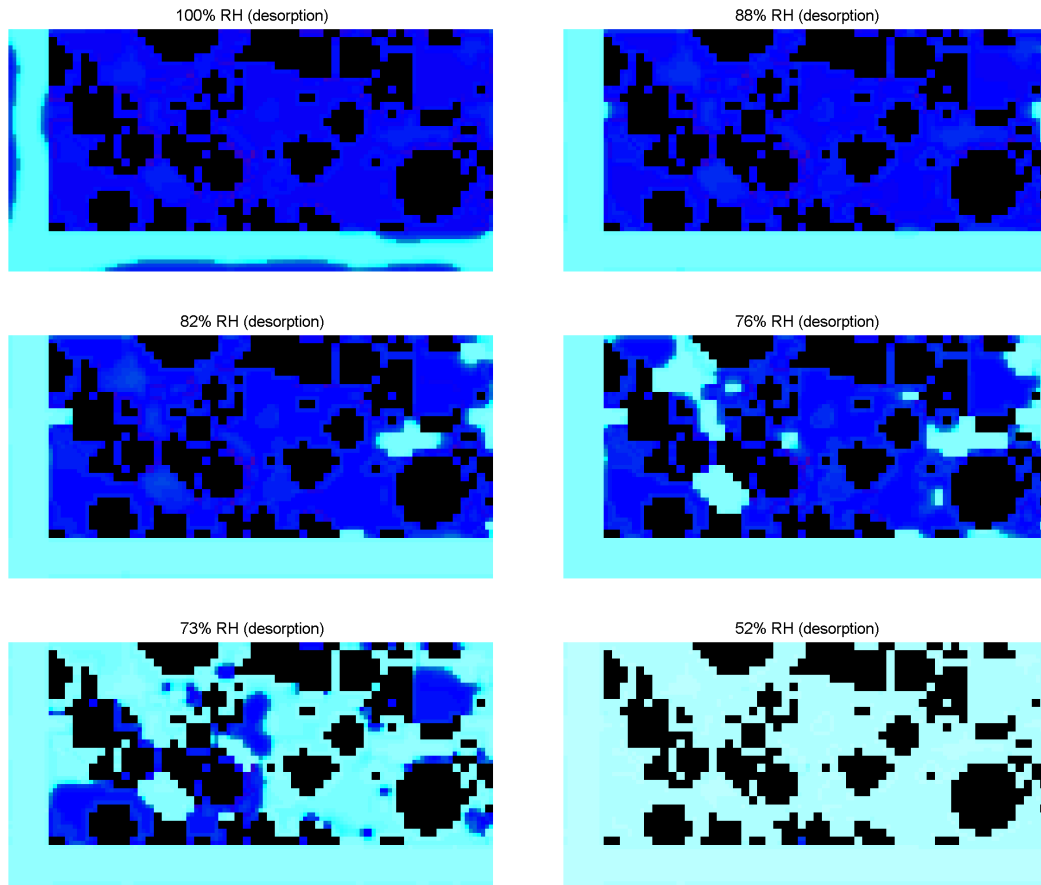


Figure 6.9: Two-dimensional slices showing the equilibrium fluid distribution during desorption in a 3D μm microstructure at critical values of the RH. The microstructure was previously shown in figure 6.5. The system is connected to a vapour source in the three spatial directions. The internal wetting potential of the C-S-H is $\phi_{C-S-H} = 0.27$. Liquid is shown in blue, vapour in cyan and solids in black.

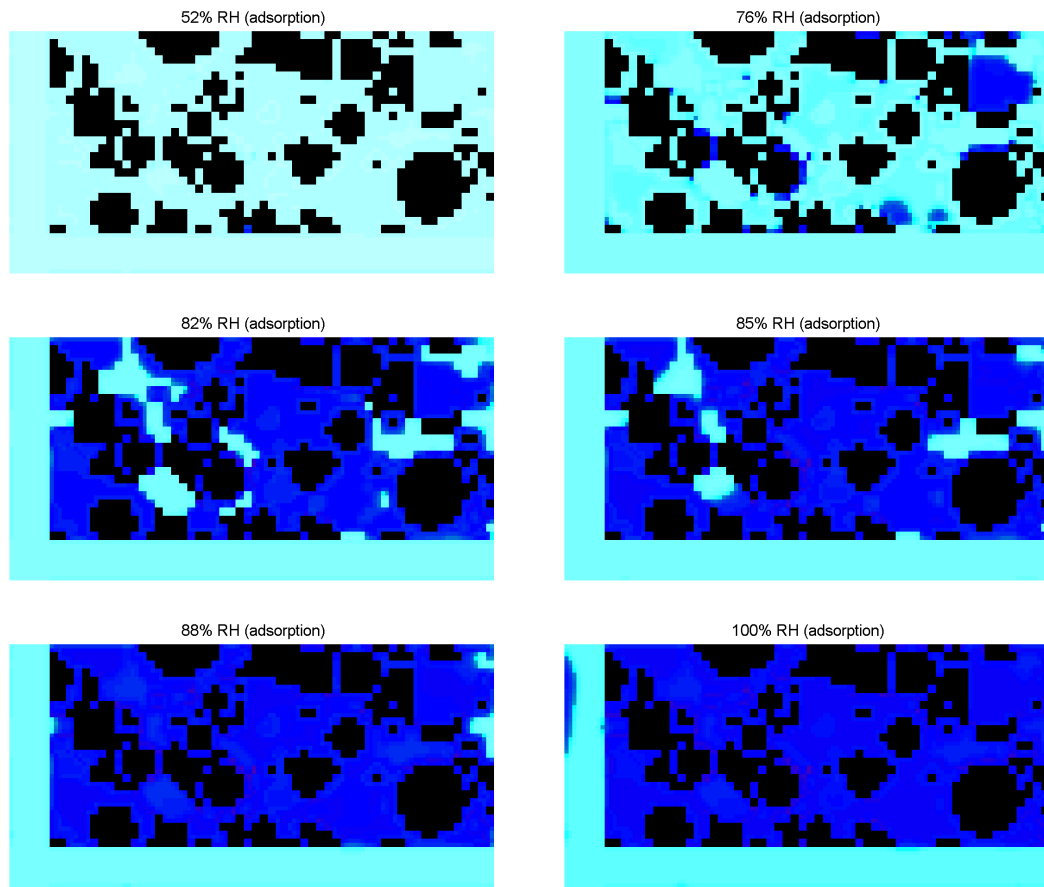


Figure 6.10: Two-dimensional slices showing the equilibrium fluid distribution during adsorption in a 3D μm microstructure at critical values of the RH. The microstructure was previously shown in figure 6.5. The system is connected to a vapour source in the three spatial directions. The internal wetting potential of the C-S-H is $\phi_{C-S-H} = 0.27$. Liquid is shown in blue, vapour in cyan and solids in black.

6.4 Discussion: Kelvin's equation, a critical limitation in the model isotherms

The water isotherms calculated in section 6.3 addressed the limitations that were previously exposed in [10]. Specifically, the test structures were bigger, had a wider pore size distribution, and the C-S-H was taken into account via the novel lattice Boltzmann free energy effective media method. However, there is a further *critical* problem related to the parametrization of the LB model with regards to the Kelvin equation (see chapter 4 section 4.1.6 for a discussion on the Kelvin equation). Taking data from figure 4.14 in section 4.1.6, it is found that in the LB simulations, a 3D spherical pore with a radius of six lattice units empties at 90.4% RH. The microstructural resolution of the model cement pastes is $\sim 0.5 \mu\text{m}$ and the lattice magnification is 2. Therefore, in the cement paste microstructures, a pore with a radius of six lattice units would have a physical radius of $1.5 \mu\text{m}$. However, using the Kelvin equation (equation 4.18) and the following standard experimental parameters:

$$\begin{aligned}\gamma &= 0.073 \text{ N.m}^{-1} \\ \Theta &= 30^\circ \\ R &= 8.314 \text{ J.mol}^{-1}\text{K}^{-1} \\ T &= 300 \text{ K} \\ T_c &= 647 \text{ K} \\ M^* &= 0.018 \text{ m}^3.\text{mol}^{-1} \\ \rho &= 1003 \text{ Kg.m}^{-3}\end{aligned}$$

it is found that a spherical pore that empties from liquid water at 90.4% RH should have a *physical* radius of $\sim 9 \text{ nm}$. This means that the six lattice units of the LB simulations represent $\sim 9 \text{ nm}$ in terms of physical units and not $0.25 \mu\text{m}$ as imposed by the resolution and magnification of the microstructure. One could think that the discrepancy may arise from the fact that water at room temperature has a reduced temperature of $\theta/\theta_c = 300/647 \simeq 0.47$ whereas the fluid in the LB model was characterized with a reduced temperature of $\theta/\theta_c = 0.96$. However, further tests revealed that decreasing the simulation temperature does decrease, not increase, the RH at which the pore emptied (table 6.1).

Table 6.1: RH at which a pore of radius six lattice units empties from liquid water for different values of the reduced simulation temperature.

θ/θ_c	ρ_{liquid}/ρ_{gas}	RH(% $\pm 0.5\%$)
0.99	1.5	96.5
0.96	2.27	90.5
0.92	3.3	80.5

To the best of the author's knowledge, the practical problem of linking the spatial dimension

of the structure to the RH of desorption has not been discussed nor solved. At present, it is unclear how to *parameterize* the free energy lattice Boltzmann algorithm in order to adjust the physical size of the lattice unit[‡]. There are several governing parameters (e.g. contact angle, interface width) but none of them is sufficient to link the spatial dimension to the RH of desorption without affecting the physics or the stability of the simulation. Hence, at present, the only *quick-fix* consists of magnifying the structure. For the reduced temperature $\theta/\theta_c = 0.96$, the magnification that is needed in order to adjust the physical resolution is ~ 28 times. Unfortunately, this is *hopeless* from a computational point of view.

6.5 Conclusions

In this chapter, a novel lattice Boltzmann algorithm was used to model the desorption and adsorption of water in cement paste. The novelties of the numerical model were previously described in chapter 4 section 4.2.7. From the cement paste perspective, this chapter presented, to the best knowledge of the author, the first numerical isotherms of cement paste that is based on an explicitly-resolved microstructure and includes the contribution of both capillary and C-S-H gel pores.

At present, the lattice spacing in the simulations is on the order of few nanometres and cannot be matched to the characteristic dimensions of the cement paste model microstructures. Hence, the algorithm was used to study qualitatively the effect of the inclusion of the gel pores on the calculated isotherms of cement paste. The algorithm was also used to test hypotheses like the ink-bottle effect. Thus, unlike chapter 5, this chapter does not end with a quantitative comparison of the model with experiments. However, the model is only one step away from such comparisons.

[‡]This was not the case for the permeability simulations shown in chapter 5 where the simulation and physical units were fully controlled.

7 Conclusions

Contents

7.1 Main findings	101
7.2 Outlook	102
7.2.1 Water isotherms of cement paste	103
7.2.2 Experimental validation	103
7.2.3 Microstructural resolution	104
7.2.4 Downscaling	104
7.2.5 Upscaling	104

7.1 Main findings

The objective of this thesis was to develop a model that can predict the permeability of cement paste based on an explicit microstructure. To achieve this, three-dimensional model microstructures were generated using the platform μic which allows the simulation of resolution-free structures based on, amongst others, input laws for reactions, kinetics and nucleation. The lattice Boltzmann (LB) method was selected for solving the equations of flow because of its ability to handle solid boundaries in complex porous media like cement paste.

Two main lattice Boltzmann permeability models were developed. The first model was motivated by the general consensus that the permeability is governed by the flow through the fully saturated capillary pores. Hence, a relatively standard LB model was developed and used to compute the flow in fully saturated microstructures where the calcium silicate hydrate (C-S-H) was treated as an impermeable solid. In this study, the main parameters were the water-to-cement ratio, the degree of hydration and the capillary porosity. The calculated permeabilities were several orders of magnitude larger than most experimental measurements. At first, this discrepancy was associated with the limited spatial resolution in the microstructures and diagonal leaks in the LB method. However, during the comparison of the results with experimental data, a large *unexplained* scatter in literature was discovered.

A careful study of the available experimental data suggested that the reason behind this scatter might be the variation in the degree of water saturation of the samples caused by different conditioning procedures. Consequently, a second LB model was developed where, in addition to the improved resolution, the capillary pores were not fully saturated. However, the problem that arose was that at middle to low degrees of water saturation, the water-filled capillary pores would depercolate and the permeability would become zero. Hence, the gel pores of the C-S-H had to be considered in the flow simulation. The issue is that the porous nature of the C-S-H is uncertain and is not revealed by microstructural models. Thus, it was decided to consider the C-S-H as an effective medium and to characterize it with an effective permeability. In this study, the main parameters were the degree of water saturation of the capillary porosity and the intrinsic permeability of the C-S-H.

The simulation of *apparent* permeability at different degrees of water saturation provided a very plausible explanation for the enormous range of experimental results ($10^{-16} - 10^{-22} \text{ m}^2$). It was found that when the capillary porosity was completely saturated with a fluid (either water or gas), the calculated intrinsic permeability was in good agreement with measurements of gas permeability on dried samples ($10^{-16} - 10^{-17} \text{ m}^2$). However, as the water saturation was reduced, the calculated apparent water permeability decreased and span the full range of experimentally measured values ($10^{-16} - 10^{-22} \text{ m}^2$). It was concluded that the degree of capillary water saturation is very likely to be the cause for variation in experimental permeability measurements. Based on the modelling results and the analysis of the available experimental data, it was suggested that most experimental measurements with water are not conducted on fully saturated samples. In such experiments, the presence of air voids in nominally water-saturated samples dramatically lowers their *apparent* permeability.

It was further concluded that the role of the weakly-permeable C-S-H, omitted in earlier modelling studies, is critical for determining the water permeability at low capillary saturation or porosity. The role of the C-S-H becomes more important as the saturated capillary porosity starts to depercolate. This is seen by comparing the results with previous LB permeability simulations that treated the C-S-H as an impermeable solid. In those calculations, as the capillary porosity decreased by increasing the degree of hydration, the permeability decreased monotonically and catastrophically close the percolation threshold, below which it could not be calculated accurately. In the effective media model, however, an asymptotic approach towards a plateau permeability dictated by the C-S-H is seen.

7.2 Outlook

This thesis provided *insights* on the link between the microstructure and the permeability of cement paste. There are several possible ways to continue and improve on this work.

7.2.1 Water isotherms of cement paste

A multi-phase model of non-ideal fluids is required to simulate the desorption and adsorption of liquid water and vapour in partially-saturated samples. The development of a multi-phase LB model was already started in chapter 4. Preliminary results were shown in chapter 6 section 6.2 where the model was used to calculate the water isotherms of the capillary pores of model cement paste. The calculated isotherms were narrow, as expected from the pore size distribution. Hence, it was decided to include the smaller C-S-H gel pores with a *novel* effective media approach, similar to the one used in the permeability simulations in chapter 5 section 5.2. To do so, the effective media approach was extended to include, in addition to the transport properties, the wetting properties of the C-S-H. This model was applied to simulate the water isotherms of the capillary and C-S-H gel pores of cement paste in chapter 6 section 6.3. In agreement with experiments, the calculated isotherms have two main steps, the first corresponding to the capillary pores and the second to the smaller gel pores.

However, at present, the model still has one major limitation. The lattice spacing in the simulations is on the order of few nanometers and it is unclear how to scale it up to match the characteristic size of the capillary pores. Hence, the model can be used to simulate phenomena that are either on the nanometre scale (characteristic pore radii of ~ 1 to 20 nm), or that are scale independent (*e.g.* phase separation, contact angle). Unfortunately, at present, the model cannot be used to predict in a quantitative manner phenomena that are scale dependent and have characteristic size larger than few nanometres, like the desorption in cement paste. However, the developed model is only one parametrization step away from such simulations. Afterwards, the calculated water isotherms can be compared quantitatively with experimental data.

7.2.2 Experimental validation

The main result of the thesis is a hypothesis that links the permeability to the degree of capillary saturation of cement paste. The comparison between the modelling results and experimental data was done on the basis of matching the degree of saturation in the model microstructures with the probable degree of saturation in the experiments. The latter was estimated from the conditioning procedure of the samples. A well-thought-out experiment would be very valuable to validate the hypothesis regarding saturation in a more definitive manner. The problem is that it is very hard to ensure full water saturation throughout the curing of the sample and the permeability experiment. A promising approach may consist of using the beam bending method on very thin samples that are cured underwater immediately after mixing. The dilemma in this case is that the effective water-to-cement ratio of the paste will increase as the water is drawn into the forming air voids during underwater curing. In this case, nuclear magnetic resonance relaxation analysis could be used to check if the additional water is uniformly distributed throughout the sample.

7.2.3 Microstructural resolution

The dependency of the permeability on the microstructural resolution was a major issue in chapter 5 section 5.1. This is because treating the C-S-H as an impermeable solid makes the percolation of the pore network, and thus the permeability, critically dependent on the resolution of the model microstructures. This issue was largely addressed in chapter 5 section 5.2 where in addition to a slightly improved resolution, the C-S-H was treated as a weakly-permeable material. These improvements decreased the dependency of the percolation of the pore network on the microstructural resolution. Hence, the dependency of the permeability on the microstructural resolution was also decreased. However, it would be interesting to improve the performance of the code to take full advantage of the resolution-free nature of the hydration model μic . Moreover, an increased computing power can be used to run the simulations with a higher lattice magnification and guarantee a better numerical accuracy.

7.2.4 Downscaling

The C-S-H gel pores have to be taken into account to accurately predict the transport properties of cement paste. In this work, this was done with an effective media approach where the C-S-H was assigned intrinsic transport and wetting properties. The primary motivation for this choice was the unavailability of a three-dimensional C-S-H structure. However, there is a lack of readily available data for the C-S-H transport properties as well. In the permeability simulations, the C-S-H was characterized with an intrinsic permeability of $\kappa_{C-S-H} = 7 \times 10^{-23} \text{ m}^2$. This is the only value that was found in literature and it is extracted from the work of Powers [118] where he says that "*measurements show that the coefficient of permeability of the gel itself is about 7×10^{-11} darcys*". However, it is unclear how these measurements were made. Hence, in chapter 5 section 5.2.4, the permeability of the C-S-H was increased and decreased by a factor 10. It was found that the permeability of the C-S-H has a non-linear effect on the permeability of cement paste. In future work, it may be possible to decide the intrinsic transport and wetting properties of the C-S-H based on newly available experimental data or atomistic simulations.

7.2.5 Upscaling

The simulations in this work were carried out on a cement paste representative elementary volume (REV) of $(100 \text{ } \mu\text{m})^3$. This relatively small size is a good starting point to understand the link between the microstructure and transport properties. However, as important as it may be to understand the fundamentals at the nano- and micro-scales, the ultimate goal is to improve the properties at the macroscopic scale of concrete structures where the REV is on the order of cubic centimetres. Fortunately, the developed lattice Boltzmann models are very appropriate for such upscaling. In particular, the simulation of the flow is easier and less prone to errors in concrete structures because their permeability is several orders of magnitude larger than that of cement paste. Moreover, the LB models that incorporate effective media are appealing

to use in a hierarchical manner. In this thesis, the effective media lattice Boltzmann model was used to simulate the flow in the capillary pores while treating the C-S-H as an effective medium of known permeability. In future work, the model could be used to calculate the permeability of concrete where the flow is solved in the micro-cracks and interfacial transition zones while treating the bulk cement paste as an effective medium of known permeability, as calculated in this work.

A MRT Collision Operator

The multi-relaxation-time collision operator is implemented in the hydraulic modes of the problem instead of the space of discrete velocities. The first term of the RHS of equation 3.2 becomes [63]:

$$\sum_{j=1}^Q S_{ij} \left(f_j(\mathbf{r}, t) - f_j^{eq}(\mathbf{r}, t) \right) = -\mathbf{M}^{-1} \cdot \mathbf{S} \cdot (\mathbf{m}(\mathbf{r}, t) - \mathbf{m}^{eq}(\mathbf{r}, t)) \quad (\text{A.1})$$

where \mathbf{M} is a 19×19 transformation matrix and \mathbf{S} is the corresponding diagonal relaxation matrix. The distributions functions are linked with the hydraulic modes via the transformation matrix \mathbf{M} with:

$$\mathbf{m} = \mathbf{M} \cdot \mathbf{f} \quad (\text{A.2})$$

$$\mathbf{f} = \mathbf{M}^{-1} \cdot \mathbf{m} \quad (\text{A.3})$$

The diagonal relaxation matrix is:

$$\mathbf{S} = \text{diag}(0, s_2, s_3, 0, s_5, 0, s_5, 0, s_5, s_{10}, s_{11}, s_{10}, s_{11}, s_{14}, s_{14}, s_{14}, s_{17}, s_{17}, s_{17}) \quad (\text{A.4})$$

and the kinematic viscosity is calculated with:

$$v = c_s^2 \left(s_{10} - \frac{\Delta t}{2} \right) \quad (\text{A.5})$$

$$= c_s^2 \left(s_{14} - \frac{\Delta t}{2} \right) \quad (\text{A.6})$$

Appendix A. MRT Collision Operator

The transformation matrix is [63]:

$$\mathbf{M} = \begin{pmatrix} 1 & 1 & 1 & 1 & 1 & 1 & 1 & 1 & 1 & 1 & 1 & 1 & 1 & 1 & 1 & 1 & 1 & 1 \\ -30 & -11 & -11 & -11 & -11 & -11 & -11 & 8 & 8 & 8 & 8 & 8 & 8 & 8 & 8 & 8 & 8 & 8 \\ 12 & -4 & -4 & -4 & -4 & -4 & -4 & 1 & 1 & 1 & 1 & 1 & 1 & 1 & 1 & 1 & 1 & 1 \\ 0 & 1 & -1 & 0 & 0 & 0 & 0 & 1 & -1 & 1 & -1 & 1 & -1 & 1 & -1 & 0 & 0 & 0 \\ 0 & -4 & 4 & 0 & 0 & 0 & 0 & 1 & -1 & 1 & -1 & 1 & -1 & 1 & -1 & 0 & 0 & 0 \\ 0 & 0 & 0 & 1 & -1 & 0 & 0 & 1 & 1 & -1 & -1 & 0 & 0 & 0 & 0 & 1 & -1 & 1 & -1 \\ 0 & 0 & 0 & -4 & 4 & 0 & 0 & 1 & 1 & -1 & -1 & 0 & 0 & 0 & 0 & 1 & -1 & 1 & -1 \\ 0 & 0 & 0 & 0 & 0 & 1 & -1 & 0 & 0 & 0 & 0 & 1 & 1 & -1 & -1 & 1 & 1 & -1 & -1 \\ 0 & 0 & 0 & 0 & 0 & -4 & 4 & 0 & 0 & 0 & 0 & 1 & 1 & -1 & -1 & 1 & 1 & -1 & -1 \\ 0 & 2 & 2 & -1 & -1 & -1 & -1 & 1 & 1 & 1 & 1 & 1 & 1 & 1 & 1 & -2 & -2 & -2 & -2 \\ 0 & -4 & -4 & 2 & 2 & 2 & 2 & 1 & 1 & 1 & 1 & 1 & 1 & 1 & 1 & 1 & -2 & -2 & -2 & -2 \\ 0 & 0 & 0 & 1 & 1 & -1 & -1 & 1 & 1 & 1 & 1 & -1 & -1 & -1 & -1 & 0 & 0 & 0 & 0 \\ 0 & 0 & 0 & -2 & -2 & 2 & 2 & 1 & 1 & 1 & 1 & -1 & -1 & -1 & -1 & 0 & 0 & 0 & 0 \\ 0 & 0 & 0 & 0 & 0 & 0 & 0 & 1 & -1 & -1 & 1 & 0 & 0 & 0 & 0 & 0 & 0 & 0 & 0 \\ 0 & 0 & 0 & 0 & 0 & 0 & 0 & 0 & 0 & 0 & 0 & 0 & 0 & 0 & 0 & 0 & 1 & -1 & -1 & 1 \\ 0 & 0 & 0 & 0 & 0 & 0 & 0 & 0 & 0 & 0 & 0 & 1 & -1 & -1 & 1 & 0 & 0 & 0 & 0 \\ 0 & 0 & 0 & 0 & 0 & 0 & 0 & 1 & -1 & 1 & -1 & -1 & 1 & -1 & 1 & 0 & 0 & 0 & 0 \\ 0 & 0 & 0 & 0 & 0 & 0 & 0 & -1 & -1 & 1 & 1 & 0 & 0 & 0 & 0 & 1 & -1 & 1 & -1 \\ 0 & 0 & 0 & 0 & 0 & 0 & 0 & 0 & 0 & 0 & 0 & 1 & 1 & -1 & -1 & -1 & 1 & 1 \end{pmatrix} \quad (\text{A.7})$$

and the moments are:

$$\mathbf{m} = (\rho, e, \varepsilon, j_x, q_x, j_y, q_y, j_z, q_z, 3p_{xx}, 3\pi_{xx}, p_{ww}, \pi_{ww}, p_{xy}, p_{yz}, p_{xz}, m_x, m_y, m_z)^T \quad (\text{A.8})$$

where T denotes the transverse operator. Finally, in the notation of the reference, the equilibrium moments are:

$$\rho^{eq} = \sum_{i=1}^Q f_i \quad (\text{A.9})$$

$$\mathbf{j}^{eq} = \sum_{i=1}^Q f_i \mathbf{e}_i \quad (\text{A.10})$$

$$e^{eq} = -11\rho + 19\mathbf{j} \cdot \mathbf{j} \quad (\text{A.11})$$

$$\varepsilon^{eq} = 3\rho - \frac{11}{2}\mathbf{j} \cdot \mathbf{j} \quad (\text{A.12})$$

$$q_x^{eq} = -\frac{2}{3}j_x \quad (\text{A.13})$$

$$q_y^{eq} = -\frac{2}{3}j_y \quad (\text{A.14})$$

$$q_z^{eq} = -\frac{2}{3}j_z \quad (\text{A.15})$$

$$p_{xx}^{eq} = \frac{1}{3} \left[2j_x^2 - (j_y^2 + j_z^2) \right] \quad (\text{A.16})$$

$$\pi_{xx}^{eq} = -\frac{1}{2} p_{xx}^{eq} \quad (\text{A.17})$$

$$p_{ww}^{eq} = j_y^2 - j_z^2 \quad (\text{A.18})$$

$$\pi_{ww}^{eq} = -\frac{1}{2} p_{ww}^{eq} \quad (\text{A.19})$$

$$p_{xy}^{eq} = j_x j_y \quad (\text{A.20})$$

$$p_{yz}^{eq} = j_y j_z \quad (\text{A.21})$$

$$p_{xz}^{eq} = j_x j_z \quad (\text{A.22})$$

$$\mathbf{m}^{eq} = 0 \quad (\text{A.23})$$

B Pressure Boundary Conditions

As discussed in chapter 3 section 3.1.3, pressure boundary conditions can be set in isothermal lattice Boltzmann simulations by taking advantage of the equation of state that links the pressure P to the density ρ with $P = c_s^2 \rho$.

For the following $D3Q19$ vector base:

$$\begin{bmatrix} i \\ e_{ix} \\ e_{iy} \\ e_{iz} \end{bmatrix} = \begin{bmatrix} 1 & 2 & 3 & 4 & 5 & 6 & 7 & 8 & 9 & 10 & 11 & 12 & 13 & 14 & 15 & 16 & 17 & 18 & 19 \\ 0 & 1 & -1 & 0 & 0 & 0 & 1 & 1 & 1 & 1 & -1 & -1 & -1 & -1 & 0 & 0 & 0 & 0 \\ 0 & 0 & 0 & 1 & -1 & 0 & 0 & 1 & -1 & 0 & 0 & 1 & -1 & 0 & 0 & 1 & 1 & -1 & -1 \\ 0 & 0 & 0 & 0 & 0 & 1 & -1 & 0 & 0 & 1 & -1 & 0 & 0 & 1 & -1 & 1 & -1 & 1 & -1 \end{bmatrix} \quad (\text{B.1})$$

the density and momentum equations (equations 3.3 and 3.4) are:

$$\rho = f_1 + f_2 + f_3 + f_4 + f_5 + f_6 + f_7 + f_8 + f_9 + f_{10} \quad (\text{B.2})$$

$$+ f_{11} + f_{12} + f_{13} + f_{14} + f_{15} + f_{16} + f_{17} + f_{18} + f_{19}$$

$$\rho u_x = f_2 + f_8 + f_9 + f_{10} + f_{11} - (f_3 + f_{12} + f_{13} + f_{14} + f_{15}) \quad (\text{B.3})$$

$$\rho u_y = f_4 + f_8 + f_{12} + f_{16} + f_{17} - (f_5 + f_9 + f_{14} + f_{18} + f_{19}) \quad (\text{B.4})$$

$$\rho u_z = f_6 + f_{10} + f_{14} + f_{16} + f_{18} - (f_7 + f_{11} + f_{15} + f_{16} + f_{18}) \quad (\text{B.5})$$

As discussed in section 3.1.3, it is possible to fix only three of the four macroscopic variables. If the density is set to $\rho = \rho_{inlet}$ and the velocities to $u_y = u_z = 0$, the set of equations become:

$$f_2 + f_8 + f_9 + f_{10} + f_{11} = \rho_{inlet} \quad (\text{B.6})$$

$$- (f_1 + f_3 + f_4 + f_5 + f_6 + f_7 + f_{12} + f_{13} + f_{14} + f_{15} + f_{16} + f_{17} + f_{18} + f_{19})$$

$$f_2 + f_8 + f_9 + f_{10} + f_{11} = \rho_{inlet} u_x \quad (\text{B.7})$$

$$- (f_3 + f_{12} + f_{13} + f_{14} + f_{15})$$

In order to obtain the five unknown components $\{f_2, f_8, f_9, f_{10}, f_{11}\}$, three additional equations are needed. These equations can be obtained by assuming that the half-way bounce-back

Appendix B. Pressure Boundary Conditions

is valid for the non-equilibrium part of three of the unknown distribution functions [66] so that $f_i - f_i^{eq} = f_{\tilde{i}} - f_{\tilde{i}}^{eq}$ where \tilde{i} is the direction opposite to i and the equilibrium distribution functions f_i^{eq} and $f_{\tilde{i}}^{eq}$ are calculated with equation 3.11. However, to keep the symmetry of the problem, this condition must be assumed for all of the five unknown components $\{f_2, f_8, f_9, f_{10}, f_{11}\}$. By doing so, the system becomes over-determined with two variables. In order to close the system, two variables, termed transverse momentum corrections, were introduced by Hecht and Harting [71]. Finally, the following equations are obtained for the inlet:

$$u_x = 1 - \frac{1}{\rho_{inlet}} [f_1 + f_4 + f_5 + f_6 + f_7 + f_{16} + f_{17} + f_{18} + f_{19} + 2(f_3 + f_{12} + f_{13} + f_{14} + f_{15})] \quad (B.8)$$

$$f_2 = f_3 + \frac{1}{3}\rho_{inlet}u_x \quad (B.9)$$

$$f_8 = f_{13} + \frac{1}{6}\rho_{inlet}u_x - N_y^x \quad (B.10)$$

$$f_9 = f_{12} + \frac{1}{6}\rho_{inlet}u_x + N_y^x \quad (B.11)$$

$$f_{10} = f_{15} + \frac{1}{6}\rho_{inlet}u_x - N_z^x \quad (B.12)$$

$$f_{11} = f_{14} + \frac{1}{6}\rho_{inlet}u_x + N_z^x \quad (B.13)$$

where N_y^x and N_z^x are the transverse momentum corrections as introduced in [71]:

$$N_y^x = \frac{1}{2} [f_4 + f_{16} + f_{17} - (f_5 + f_{18} + f_{19})] \quad (B.14)$$

$$N_z^x = \frac{1}{2} [f_6 + f_{12} + f_{16} - (f_7 + f_{17} + f_{19})] \quad (B.15)$$

Similarly, for at the outlet:

$$u_x = -1 + \frac{1}{\rho_{outlet}} [f_1 + f_4 + f_5 + f_6 + f_7 + f_{16} + f_{17} + f_{18} + f_{19} + 2(f_2 + f_8 + f_9 + f_{10} + f_{11})] \quad (B.16)$$

$$f_3 = f_2 - \frac{1}{3}\rho_{outlet}u_x \quad (B.17)$$

$$f_{12} = f_9 - \frac{1}{6}\rho_{outlet}u_x - N_y^x \quad (B.18)$$

$$f_{13} = f_8 - \frac{1}{6}\rho_{outlet}u_x + N_y^x \quad (B.19)$$

$$f_{14} = f_{11} - \frac{1}{6}\rho_{outlet}u_x - N_z^x \quad (B.20)$$

$$f_{15} = f_{10} - \frac{1}{6}\rho_{outlet}u_x + N_z^x \quad (B.21)$$

C Effective permeability

In this appendix, the analytical expression given in equation 3.32 that relates the effective media parameter to the intrinsic permeability of a grey node is derived*. To do so, the three-dimensional lattice is projected onto a one-dimensional lattice with three velocities: a stationary velocity e_0 , a velocity in the positive direction e_+ , and a velocity in the negative direction e_- . The equations governing the equilibrium fluid densities become:

$$f_0^{eq} = \rho \left(\frac{2}{3} - u^2 \right) \quad (C.1)$$

$$f_+^{eq} = \frac{1}{6} \rho (1 + 3u + 3u^2) \quad (C.2)$$

$$f_-^{eq} = \frac{1}{6} \rho (1 - 3u + 3u^2) \quad (C.3)$$

The stationary fluid packed density is constant under steady-state conditions. Consequently:

$$f_0 = \rho \left(\frac{2}{3} - u^2 \right) \quad (C.4)$$

$$f_{+2} = (1 - \sigma) f_{+1} + \sigma f_{-1} \quad (C.5)$$

$$f_{-1} = (1 - \sigma) f_{-2} + \sigma f_{+2} \quad (C.6)$$

where the additional subscripts refer to the fluid packets for two neighbouring nodes 1 and 2. By introducing the following variables:

$$p = f_+ + f_- = \rho - f_0 \quad (C.7)$$

$$m = f_+ - f_- = \rho u \quad (C.8)$$

We obtain:

$$p_2 + m_2 = p_1 + (1 - 2\sigma) m_1 \quad (C.9)$$

$$p_1 - m_1 = p_2 - (1 - 2\sigma) m_2 \quad (C.10)$$

*The derivation is largely inspired by the work of Walsh *et al.* [91].

Appendix C. Effective permeability

Combining equations C.1, C.9 and C.10 yeilds an expression for the change in p across a one-dimensional lattice comprising $N + 1$ nodes numbered from 0 to N :

$$\begin{aligned}\Delta p &= \rho_0 \left(\frac{1}{3} + u_0^2 \right) - \rho_N \left(\frac{1}{3} + u_N^2 \right) \\ &= 2\sigma \rho_0 u_0 N\end{aligned}\tag{C.11}$$

Equation C.11 can be written under the form:

$$u_0^2 + \frac{2\sigma \rho_N N}{\rho_0 - \rho_N} u_0 - \frac{\rho_N}{3\rho_0} = 0\tag{C.12}$$

Thus,

$$\begin{aligned}u_0 &= -\frac{\sigma \rho_N N}{\rho_0 - \rho_N} + \sqrt{\left(\frac{\sigma \rho_N N}{\rho_0 - \rho_N} \right)^2 + \frac{\rho_N}{3\rho_0}} \\ &\simeq \frac{\Delta \rho}{6\sigma \rho_0 N}\end{aligned}\tag{C.13}$$

where the change in density, $\Delta \rho = \rho_0 - \rho_N$, is related to the pressure drop ΔP across the lattice by:

$$\Delta P = \frac{1}{3} \Delta \rho\tag{C.14}$$

Finally, the permeability κ of a grey node of effective media parameter σ can be obtained from equations 3.29, 2.1, C.13 and C.14:

$$\kappa = \frac{(1 - \sigma) v}{2\sigma}\tag{C.15}$$

D Mathematical Operators

The gradient and Laplacian stencils can be calculated with:

$$\partial_x = \left[\begin{pmatrix} 0 & 0 & 0 \\ -B & 0 & B \\ 0 & 0 & 0 \end{pmatrix}, \begin{pmatrix} -B & 0 & B \\ -A & 0 & A \\ -B & 0 & B \end{pmatrix}, \begin{pmatrix} 0 & 0 & 0 \\ -B & 0 & B \\ 0 & 0 & 0 \end{pmatrix} \right] \quad (\text{D.1})$$

and

$$\nabla^2 = \left[\begin{pmatrix} 0 & D & 0 \\ D & C & D \\ 0 & D & 0 \end{pmatrix}, \begin{pmatrix} D & C & D \\ C & E & C \\ D & C & D \end{pmatrix}, \begin{pmatrix} 0 & D & 0 \\ D & C & D \\ 0 & D & 0 \end{pmatrix} \right] \quad (\text{D.2})$$

where $E = -6C - 12D$, $2A + 8B = 1$ and $C + 4D = 1$ [101]. The left, middle, and right matrices show slices of the stencils for $\mathbf{e}_i = (0, 0, -1)$, $\mathbf{e}_i = (0, 0, 0)$ and $\mathbf{e}_i = (0, 0, 1)$, respectively. The coefficients A, B, C and D can be tuned to reduce the spurious velocities at equilibrium. Their values are chosen following the work of Pooley and Furtado [101] so that: $A = \frac{1}{6}$, $B = \frac{1}{12}$, $C = \frac{1}{3}$, $D = \frac{1}{6}$ and $E = -4$. The parameters $\omega_i^{p,t,\alpha\alpha,\alpha\beta}$ can be adjusted to reduce the spurious velocities as well and their values can be found in [101].

In the numerical algorithm, the following expressions were used for the bulk nodes:

$$\begin{aligned} \partial_x \rho_{(x,y,z)} = & \frac{\rho_{(x+1,y,z)} - \rho_{(x-1,y,z)}}{6} \\ & + \frac{\rho_{(x+1,y-1,z)} + \rho_{(x+1,y+1,z)} + \rho_{(x+1,y,z-1)} + \rho_{(x+1,y,z+1)}}{12} \\ & - \frac{\rho_{(x-1,y-1,z)} + \rho_{(x-1,y+1,z)} + \rho_{(x-1,y,z-1)} + \rho_{(x-1,y,z+1)}}{12} \end{aligned} \quad (\text{D.3})$$

Appendix D. Mathematical Operators

$$\begin{aligned}\partial_y \rho_{(x,y,z)} &= \frac{\rho_{(x,y+1,z)} - \rho_{(x,y-1,z)}}{6} \\ &+ \frac{\rho_{(x+1,y+1,z)} + \rho_{(x-1,y+1,z)} + \rho_{(x,y+1,z-1)} + \rho_{(x,y+1,z+1)}}{12} \\ &- \frac{\rho_{(x+1,y-1,z)} + \rho_{(x-1,y-1,z)} + \rho_{(x,y-1,z-1)} + \rho_{(x,y-1,z+1)}}{12}\end{aligned}\quad (D.4)$$

$$\begin{aligned}\partial_z \rho_{(x,y,z)} &= \frac{\rho_{(x,y,z+1)} - \rho_{(x,y,z-1)}}{6} \\ &+ \frac{\rho_{(x+1,y,z+1)} + \rho_{(x-1,y,z+1)} + \rho_{(x,y+1,z+1)} + \rho_{(x,y-1,z+1)}}{12} \\ &- \frac{\rho_{(x+1,y,z-1)} + \rho_{(x-1,y,z-1)} + \rho_{(x,y+1,z-1)} + \rho_{(x,y-1,z-1)}}{12}\end{aligned}\quad (D.5)$$

and

$$\begin{aligned}\nabla^2 \rho_{(x,y,z)} &= \frac{\rho_{(x+1,y,z)} + \rho_{(x-1,y,z)} + \rho_{(x,y+1,z)} + \rho_{(x,y-1,z)} + \rho_{(x,y,z+1)} + \rho_{(x,y,z-1)}}{3} \\ &+ \frac{\rho_{(x+1,y-1,z)} + \rho_{(x-1,y-1,z)} + \rho_{(x+1,y+1,z)} + \rho_{(x-1,y+1,z)} + \rho_{(x+1,y,z-1)} + \rho_{(x-1,y,z-1)}}{6} \\ &+ \frac{\rho_{(x+1,y,z+1)} + \rho_{(x-1,y,z+1)} + \rho_{(x,y+1,z-1)} + \rho_{(x,y-1,z-1)} + \rho_{(x,y+1,z+1)} + \rho_{(x,y-1,z+1)}}{6} \\ &- 4\rho_{(x,y,z)}\end{aligned}\quad (D.6)$$

On surface nodes near the solid boundaries, the following expressions were used:

$$\begin{aligned}\partial_x \rho_{(x,y,z)} &= \frac{1}{2} \left[\rho' \sigma_{(x+1,y,z)} + \rho_{(x+1,y,z)} [1 - \sigma_{(x+1,y,z)}] \right. \\ &\quad \left. - \rho' \sigma_{(x-1,y,z)} - \rho_{(x-1,y,z)} [1 - \sigma_{(x-1,y,z)}] \right]\end{aligned}\quad (D.7)$$

$$\begin{aligned}\partial_y \rho_{(x,y,z)} &= \frac{1}{2} \left[\rho' \sigma_{(x,y+1,z)} + \rho_{(x,y+1,z)} [1 - \sigma_{(x,y+1,z)}] \right. \\ &\quad \left. - \rho' \sigma_{(x,y-1,z)} - \rho_{(x,y-1,z)} [1 - \sigma_{(x,y-1,z)}] \right]\end{aligned}\quad (D.8)$$

$$\begin{aligned}\partial_z \rho_{(x,y,z)} &= \frac{1}{2} \left[\rho' \sigma_{(x,y,z+1)} + \rho_{(x,y,z+1)} [1 - \sigma_{(x,y,z+1)}] \right. \\ &\quad \left. - \rho' \sigma_{(x,y,z-1)} - \rho_{(x,y,z-1)} [1 - \sigma_{(x,y,z-1)}] \right]\end{aligned}\quad (D.9)$$

and

$$\begin{aligned}
\nabla^2 \rho_{(x,y,z)} = & \rho' \left[\sigma_{(x+1,y,z)} + \sigma_{(x-1,y,z)} + \sigma_{(x,y+1,z)} + \sigma_{(x,y-1,z)} + \sigma_{(x,y,z+1)} + \sigma_{(x,y,z-1)} \right] \\
& + \rho_{(x+1,y,z)} [1 - \sigma_{(x+1,y,z)}] + \rho_{(x-1,y,z)} [1 - \sigma_{(x-1,y,z)}] \\
& + \rho_{(x,y+1,z)} [1 - \sigma_{(x,y+1,z)}] + \rho_{(x,y-1,z)} [1 - \sigma_{(x,y-1,z)}] \\
& + \rho_{(x,y,z+1)} [1 - \sigma_{(x,y,z+1)}] + \rho_{(x,y,z-1)} [1 - \sigma_{(x,y,z-1)}] \\
& - 6\rho_{(x,y,z)} [1 - \sigma_{(x,y,z)}]
\end{aligned} \tag{D.10}$$

where

$$\sigma_{(x,y,z)} = \begin{cases} 0 & \text{if (x,y,z) is a fluid node} \\ 1 & \text{if (x,y,z) is a solid node} \end{cases} \tag{D.11}$$

$$\rho' = \rho_{(x,y,z)} [1 - \sigma_{(x,y,z)}] + \phi \tag{D.12}$$

and ϕ is the wetting potential.

Bibliography

- [1] <http://www.wbcdcement.org>.
- [2] K. L. Scrivener, A. K. Crumbie, P. Laugesen, The interfacial transition zone (itz) between cement paste and aggregate in concrete, *Interface Science* 12 (2004) 411–421.
- [3] A. C. A. Muller, K. L. Scrivener, A. M. Gajewicz, P. J. McDonald, Densification of c-s-h measured by ^1H nmr relaxometry, *Journal of Physical Chemistry C* 117 (2013) 403–412.
- [4] H. Wong, M. Zobel, N. Buenfeld, R. Zimmerman, Influence of the interfacial transition zone and microcracking on the diffusivity, permeability and sorptivity of cement-based materials after drying, *Magazine of Concrete Research* 61 (2009) 571 –589.
- [5] H. Darcy, *Les Fontaines Publiques de la Ville de Dijon*, Dalmont, Paris, 1856.
- [6] B. Ferreol, D. H. Rothman, Lattice-boltzmann simulations of flow through fontainebleau sandstone, *Transport in Porous Media* 20 (1995) 3–20.
- [7] Q. Kang, D. Zhang, S. Chen, X. He, Lattice boltzmann simulation of chemical dissolution in porous media, *Physical Review E* 65 (2002) 036318.
- [8] M. A. Van Doormaal, J. G. Pharoah, Determination of permeability in fibrous porous media using the lattice boltzmann method with application to pem fuel cells, *International journal for numerical methods in fluids* 59 (2009) 75–89.
- [9] E. J. Garboczi, D. P. Bentz, The effect of statistical fluctuation, finite size error, and digital resolution on the phase percolation and transport properties of the nist cement hydration model, *Cement and Concrete Research* 31 (2001) 1501–1514.
- [10] M. Zalzale, P. J. McDonald, Lattice boltzmann simulations of the permeability and capillary adsorption of cement model microstructures, *Cement and Concrete Research* 42 (2012) 1601–1610.
- [11] M. Zhang, G. Ye, K. van Breugel, Modeling of ionic diffusivity in non-saturated cement-based materials using lattice boltzmann method, *Cement and Concrete Research* 42 (2012) 1524 – 1533.

Bibliography

- [12] M. Zhang, G. Ye, K. v. Breugel, Microstructure-based modeling of permeability of cementitious materials using multiple-relaxation-time lattice boltzmann method, *Computational Materials Science* 68 (2013) 142–151.
- [13] M. Zalzale, P. J. McDonald, K. L. Scrivener, A 3d lattice boltzmann effective media study: understanding the role of c-s-h and water saturation on the permeability of cement paste, *Modelling and Simulation in Materials Science and Engineering* 21 (2013) 085016.
- [14] R. J.-M. Pellenq, A. Kushima, R. Shahsavari, K. J. Van Vliet, M. J. Buehler, S. Yip, F.-J. Ulm, A realistic molecular model of cement hydrates, *Proceedings of the National Academy of Sciences* 106 (2009) 16102–16107.
- [15] S. Galmarini, A. Aimable, N. Ruffray, P. Bowen, Changes in portlandite morphology with solvent composition: Atomistic simulations and experiment, *Cement and Concrete Research* 41 (2011) 1330 – 1338, *conferences Special: Cement Hydration Kinetics and Modeling*, Quebec City, 2009; CONMOD10, Lausanne, 2010.
- [16] C. Pignat, P. Navi, K. L. Scrivener, Simulation of cement paste microstructure hydration, pore space characterization and permeability determination, *Materials and Structures* 38 (2005) 459–466.
- [17] M. Koster, J. Hannawald, W. Brameshuber, Simulation of water permeability and water vapor diffusion through hardened cement paste, *Computational Mechanics* 37 (2006) 163–172.
- [18] G. Ye, P. Lura, K. van Breugel, Modelling of water permeability in cementitious materials, *Materials and Structures* 39 (2006) 877–885.
- [19] T. C. Powers, L. E. Copeland, J. C. Hayes, H. M. Mann, *Permeability of portland cement paste* (1955).
- [20] B. K. Nyame, J. M. Illston, Relationships between permeability and pore structure of hardened cement paste, *Magazine of Concrete Research* 33 (1981) 139–146.
- [21] N. Banthia, S. Mindess, Water permeability of cement paste, *Cement and Concrete Research* 19 (1989) 727–736.
- [22] G. Ye, Percolation of capillary pores in hardening cement pastes, *Cement and Concrete Research* 35 (2005) 167–176.
- [23] W. Vichit-Vadakan, G. W. Scherer, Measuring permeability and stress relaxation of young cement paste by beam bending, *Cement and Concrete Research* 33 (2003) 1925–1932.
- [24] H. Ai, J. F. Young, G. W. Scherer, Thermal expansion kinetics: Method to measure permeability of cementitious materials: Ii, application to hardened cement pastes, *Journal of the American Ceramic Society* 84 (2001) 385–91.

- [25] W. Vichit-Vadakan, G. Scherer, Measuring permeability of rigid materials by a beam-bending method: Iii, cement paste, *Journal of the American Ceramic Society* 85 (2002) 1537–1544.
- [26] Z. Grasley, G. Scherer, D. Lange, J. Valenza, Dynamic pressurization method for measuring permeability and modulus: Ii. cementitious materials, *Materials and Structures* 40 (2007) 711–721.
- [27] P. B. Bamforth, The relationship between permeability coefficients for concrete obtained using liquid and gas, *Magazine of Concrete Research* 39 (1987) 3–11.
- [28] H. Loosveldt, Z. Lafhaj, F. Skoczylas, Experimental study of gas and liquid permeability of a mortar, *Cement and Concrete Research* 32 (2002) 1357–1363.
- [29] R. K. Dhir, P. C. Hewlett, Y. N. Chan, Near surface characteristics of concrete: intrinsic permeability, *Magazine of Concrete Research* 41 (1989) 87–97.
- [30] N. Hearn, R. J. Detwiler, C. Sframeli, Water permeability and microstructure of three old concretes, *Cement and Concrete Research* 24 (1994) 633–640.
- [31] A. Abbas, M. Carcasses, J. P. Ollivier, Gas permeability of concrete in relation to its degree of saturation, *Materials and Structures* 32 (1999) 3–8.
- [32] V. Baroghel-Bouny, M. Thiéry, X. Wang, Modelling of isothermal coupled moisture–ion transport in cementitious materials, *Cement and Concrete Research* 41 (2011) 828–841.
- [33] H. Wong, N. Buenfeld, J. Hill, A. Harris, Mass transport properties of mature wasteform grouts, *Advances in Cement Research* 19 (2007) 35–46.
- [34] S. Zamani, R. Kowalczyk, P. McDonald, The relative humidity dependence of the permeability of cement paste measured using garfield nmr profiling, *Cement and Concrete Research* 57 (2014) 88 – 94.
- [35] A. C. A. Muller, Personal communication: Vacuum saturation of the air voids inside sealed cured cement samples: a 1h nuclear magnetic resonance relaxation analysis (2012).
- [36] A. J. Katz, A. H. Thompson, Quantitative prediction of permeability in porous rock, *Physical Review B* 34 (1986) 8179–8181.
- [37] A. J. Katz, A. H. Thompson, Prediction of rock electrical conductivity from mercury injection measurements, *Journal of Geophysical Research* 92 (1987) 599–607.
- [38] A. S. El-Dieb, R. D. Hooton, Evaluation of the katz-thompson model for estimating the water permeability of cement-based materials from mercury intrusion porosimetry data, *Cement and Concrete Research* 24 (1994) 443–455.

Bibliography

- [39] B. J. Christensen, T. O. Mason, H. M. Jennings, Comparison of measured and calculated permeabilities for hardened cement pastes, *Cement and Concrete Research* 26 (1996) 1325–1334.
- [40] G. W. Scherer, J. J. Valenza Ii, G. Simmons, New methods to measure liquid permeability in porous materials, *Cement and Concrete Research* 37 (2007) 386–397.
- [41] L. Cui, J. H. Cahyadi, Permeability and pore structure of opc paste, *Cement and Concrete Research* 31 (2001) 277–282.
- [42] D. S. McLachlan, M. Blaszkiewicz, R. E. Newnham, Electrical resistivity of composites, *Journal of the American Ceramic Society* 73 (1990) 2187–2203.
- [43] K. van Breugel, Numerical simulation of hydration and microstructural development in hardening cement-based materials (i) theory, *Cement and Concrete Research* 25 (1995) 319–331.
- [44] D. P. Bentz, Three-dimensional computer simulation of portland cement hydration and microstructure development, *Journal of the American Ceramic Society* 80 (1997) 3–21.
- [45] S. Bishnoi, Vector modeling of hydrating cement microstructure and kinetics, Ph.D. thesis, Ecole Polytechnique Fédérale de Lausanne (2008).
- [46] O. Švec, J. Skoček, H. Stang, J. F. Olesen, P. N. Poulsen, Flow simulation of fiber reinforced self-compacting concrete using lattice boltzmann method, in: *International Congress on the Chemistry of Cement* 2011.
- [47] U. Frisch, D. d’Humieres, B. Hasslacher, P. Lallemand, Y. Pomeau, J.-P. Rivet, Lattice gas hydrodynamics in two and three dimensions, *Complex systems* 1 (1987) 649–707.
- [48] G. R. McNamara, G. Zanetti, Use of the boltzmann equation to simulate lattice-gas automata, *Physical Review Letters* 61 (1988) 2332–2335.
- [49] F. J. Higuera, J. Jiménez, Boltzmann approach to lattice gas simulations, *Europhysics Letters* 9 (1989) 663–668.
- [50] S. Succi, E. Foti, F. Higuera, Three-dimensional flows in complex geometries with the lattice boltzmann method, *Europhysics Letters* 10 (1989) 433.
- [51] H. Chen, S. Chen, W. H. Matthaeus, Recovery of the navier-stokes equations using a lattice-gas boltzmann method, *Physical Review A* 45 (1992) 5339–5342.
- [52] S. Chen, G. D. Doolen, Lattice boltzmann method for fluid flows, *Annual Review of Fluid Mechanics* 30 (1998) 329–364.
- [53] S. Succi, *The lattice Boltzmann equation for fluid dynamics and beyond*, Clarendon Press, Oxford, 2001.

-
- [54] C. K. Aidun, J. R. Clausen, Lattice-boltzmann method for complex flows, *Annual Review of Fluid Mechanics* 42 (2010) 439–472.
- [55] X. Shan, H. Chen, Lattice boltzmann model for simulating flows with multiple phases and components, *Physical Review E* 47 (1993) 1815–1819.
- [56] M. R. Swift, E. Orlandini, W. R. Osborn, J. M. Yeomans, Lattice boltzmann simulations of liquid-gas and binary fluid systems, *Physical Review E* 54 (1996) 5041–5052.
- [57] R. Benzi, S. Succi, Two-dimensional turbulence with the lattice boltzmann equation, *Journal of Physics A: Mathematical and General* 23 (1990) L1.
- [58] S. Chen, H. Chen, D. Martnez, W. Matthaeus, Lattice boltzmann model for simulation of magnetohydrodynamics, *Physical Review Letters* 67 (1991) 3776.
- [59] M. Mendoza, B. Boghosian, H. Herrmann, S. Succi, Fast lattice boltzmann solver for relativistic hydrodynamics, *Physical Review Letters* 105 (2010) 014502.
- [60] J. Wang, M. Wang, Z. Li, A lattice boltzmann algorithm for fluid–solid conjugate heat transfer, *International Journal of Thermal Sciences* 46 (2007) 228–234.
- [61] C. Körner, M. Thies, T. Hofmann, N. Thürey, U. Rüde, Lattice boltzmann model for free surface flow for modeling foaming, *Journal of Statistical Physics* 121 (2005) 179–196.
- [62] X. He, L.-S. Luo, Theory of the lattice boltzmann method: From the boltzmann equation to the lattice boltzmann equation, *Physical Review E* 56 (1997) 6811–6817.
- [63] D. D’Humières, I. Ginzburg, M. Krafczyk, P. Lallemand, L.-S. Luo, Multiple-relaxation-time lattice boltzmann models in three dimensions, *Philosophical Transactions of the Royal Society of London. Series A: Mathematical, Physical and Engineering Sciences* 360 (2002) 437–451.
- [64] C. Pan, L.-S. Luo, C. T. Miller, An evaluation of lattice boltzmann schemes for porous medium flow simulation, *Computers and Fluids* 35 (2006) 898–909.
- [65] D. D’Humières, I. Ginzburg, Viscosity independent numerical errors for lattice boltzmann models: From recurrence equations to "magic" collision numbers, *Computers and Mathematics with Applications* 58 (2009) 823–840.
- [66] X. He, Q. Zou, L.-S. Luo, M. Dembo, Analytic solutions of simple flows and analysis of nonslip boundary conditions for the lattice boltzmann bgk model, *Journal of Statistical Physics* 87 (1997) 115–136.
- [67] Z. Guo, C. Zheng, B. Shi, Discrete lattice effects on the forcing term in the lattice boltzmann method, *Physical Review E* 65 (2002) 046308.
- [68] Q. Zou, X. He, On pressure and velocity boundary conditions for the lattice boltzmann bgk model, *Physics of Fluids* 9 (1997) 1591–1598.

Bibliography

- [69] A. Narváez, T. Zauner, F. Raischel, R. Hilfer, J. Harting, Quantitative analysis of numerical estimates for the permeability of porous media from lattice-boltzmann simulations, *Journal of Statistical Mechanics: Theory and Experiment* 11 (2010) P11026.
- [70] M. E. Kutay, A. H. Aydilek, E. Masad, Laboratory validation of lattice boltzmann method for modeling pore-scale flow in granular materials, *Computers and Geotechnics* 33 (2006) 381–395.
- [71] M. Hecht, J. Harting, Implementation of on-site velocity boundary conditions for d3q19 lattice boltzmann simulations, *Journal of Statistical Mechanics: Theory and Experiment* 2010 (2010) P01018.
- [72] <http://www.accelereyes.com>.
- [73] A. Narváez, J. Harting, Evaluation of pressure boundary conditions for permeability calculations using the lattice-boltzmann method, *Advances in Applied Mathematics and Mechanics* 2 (2010) 685–700.
- [74] T. W. Patzek, D. B. Silin, Shape factor and hydraulic conductance in noncircular capillaries: I. one-phase creeping flow, *Journal of Colloid and Interface Science* 236 (2001) 295–304.
- [75] R. E. Larson, J. J. L. Higdon, A periodic grain consolidation model of porous media, *Physics of Fluids A* 1 (1989) 38–46.
- [76] C. Manwart, U. Aaltosalmi, A. Koponen, R. Hilfer, J. Timonen, Lattice-boltzmann and finite-difference simulations for the permeability for three-dimensional porous media, *Physical Review E* 66 (2002) 016702.
- [77] H. C. Brinkman, A calculation of the viscous force exerted by a flowing fluid on a dense swarm of particles, *Applied Scientific Research* 1 (1949) 27–34.
- [78] M. A. A. Spaid, J. F. R. Phelan, Lattice boltzmann methods for modeling microscale flow in fibrous porous media, *Physics of Fluids* 9 (1997) 2468–2474.
- [79] D. M. Freed, Lattice-boltzmann method for macroscopic porous media modeling, *International Journal of Modern Physics C* 09 (1998) 1491–1503.
- [80] N. S. Martys, Improved approximation of the brinkman equation using a lattice boltzmann method, *Physics of Fluids* 13 (2001) 1807–1810.
- [81] N. Martys, J. Hagedorn, Multiscale modeling of fluid transport in heterogeneous materials using discrete boltzmann methods, *Materials and Structures* 35 (2002) 650–658.
- [82] K. Balasubramanian, F. Hayot, W. F. Saam, Darcy's law from lattice-gas hydrodynamics, *Physical Review A* 36 (1987) 2248–2253.

-
- [83] Y. Gao, M. M. Sharma, A lga model for fluid flow in heterogeneous porous media, *Transport in Porous Media* 17 (1994) 1–17.
- [84] O. Dardis, J. McCloskey, Lattice boltzmann scheme with real numbered solid density for the simulation of flow in porous media, *Physical Review E* 57 (1998) 4834–4837.
- [85] O. Dardis, J. McCloskey, Permeability porosity relationships from numerical simulations of fluid flow, *Geophysical Research Letters* 25 (1998) 1471–1474.
- [86] J. Kozeny, Ueber kapillare leitung des wassers im boden, *Wien, Akad. Wiss* 136 (1927) 271.
- [87] P. Carman, Fluid flow through granular beds, *Transactions-Institution of Chemical Engineeres* 15 (1937) 150–166.
- [88] D. Thorne, M. Sukop, Lattice boltzmann model for the elder problem, in: *XVth International Conference on Computational Methods in Water Resources (CMWR XV)*, Elsevier, 2004, pp. 1549–1557.
- [89] M. Sukop, D. Thorne, *Lattice Boltzmann Modeling: An Introduction for Geoscientists and Engineers*, Springer, 2006.
- [90] Y. Chen, K. Zhu, A study of the upper limit of solid scatters density for gray lattice boltzmann method, *Acta Mechanica Sinica* 24 (2008) 515–522.
- [91] S. D. C. Walsh, H. Burwinkle, M. O. Saar, A new partial-bounceback lattice-boltzmann method for fluid flow through heterogeneous media, *Computers and Geosciences* 35 (2009) 1186–1193.
- [92] J. Zhu, J. Ma, An improved gray lattice boltzmann model for simulating fluid flow in multi-scale porous media, *Advances in Water Resources* 56 (2013) 61–76.
- [93] S. D. C. Walsh, M. O. Saar, Macroscale lattice-boltzmann methods for low peclet number solute and heat transport in heterogeneous porous media, *Water Resources Research* 46 (2010) W07517.
- [94] A. K. Gunstensen, D. H. Rothman, S. Zaleski, G. Zanetti, Lattice boltzmann model of immiscible fluids, *Physical Review A* 43 (1991) 4320.
- [95] A. K. Gunstensen, D. H. Rothman, Microscopic modeling of immiscible fluids in three dimensions by a lattice boltzmann method, *Europhysics Letters* 18 (1992) 157.
- [96] M. Sbragaglia, R. Benzi, L. Biferale, S. Succi, K. Sugiyama, F. Toschi, Generalized lattice boltzmann method with multirange pseudopotential, *Phys. Rev. E* 75 (2007) 026702.
- [97] C. M. Pooley, H. Kusumaatmaja, J. M. Yeomans, Contact line dynamics in binary lattice boltzmann simulations, *Physical Review E* 78 (2008) 056709.

Bibliography

- [98] A. J. Briant, P. Papatzacos, J. M. Yeomans, Lattice boltzmann simulations of contact line motion in a liquid-gas system, *Philosophical Transactions of the Royal Society of London. Series A: Mathematical, Physical and Engineering Sciences* 360 (2002) 485–495.
- [99] A. Briant, A. Wagner, J. Yeomans, Lattice boltzmann simulations of contact line motion. i. liquid-gas systems, *Physical Review E* 69 (2004) 031602.
- [100] A. J. Wagner, C. M. Pooley, Interface width and bulk stability: Requirements for the simulation of deeply quenched liquid-gas systems, *Physical Review E* 76 (2007) 045702.
- [101] C. M. Pooley, K. Furtado, Eliminating spurious velocities in the free-energy lattice boltzmann method, *Physical Review E* 77 (2008) 046702.
- [102] D. Holdych, D. Rovas, J. Georgiadis, R. Buckius, An improved hydrodynamics formulation for multiphase flow lattice-boltzmann models, *International Journal of Modern Physics C* 9 (1998) 1393–1404.
- [103] T. Young, An essay on the cohesion of fluids, *Philosophical Transactions of the Royal Society of London* (1805) 65–87.
- [104] J. W. Cahn, Critical point wetting, *The Journal of Chemical Physics* 66 (1977) 3667–3672.
- [105] J. Yeomans, Mesoscale simulations: Lattice boltzmann and particle algorithms, *Physica A: Statistical Mechanics and its Applications* 369 (2006) 159–184.
- [106] S. Bishnoi, K. L. Scrivener, μic : A new platform for modelling the hydration of cements, *Cement and Concrete Research* 39 (2009) 266–274.
- [107] V. Kocaba, Development and evaluation of methods to follow microstructural development of cementitious systems including slags, Ph.D. thesis, Ecole Polytechnique Fédérale de Lausanne (2009).
- [108] H. Taylor, *Cement chemistry*, 2nd Edition, Thomas Telford, London, 1997.
- [109] T. C. Powers, T. Brownyard, *Studies of the physical properties of hardened portland cement paste* (1948).
- [110] Q. H. Do, S. Bishnoi, K. L. Scrivener, Numerical simulation of porosity in cements, *Transport in Porous Media* 99 (2013) 101–117.
- [111] Q. H. Do, Personal communication: Depercolation of the porosity in μic microstructures (2013).
- [112] <http://ciks.cbt.nist.gov/bentz/phpct/database/images>.
- [113] R. Feldman, P. Sereda, A new model for hydrated portland cement and its practical implications, *Engineering Journal* 53 (1970) 53–59.

- [114] H. M. Jennings, Refinements to colloid model of c-s-h in cement: Cm-ii, *Cement and Concrete Research* 38 (2008) 275–289.
- [115] M. A. Etzold, P. J. McDonald, A. F. Routh, Growth of sheets in 3d confinements—a model for the c–s–h meso structure, *Cement and Concrete Research* 63 (2014) 137–142.
- [116] L. J. Parrot, D. C. Kiloh, Prediction of cement hydration, *Proc. Br. Ceram. Soc.* 35 (1984) 41–53.
- [117] <http://gems.web.psi.ch/>.
- [118] T. C. Powers, Structure and physical properties of hardened portland cement paste, *Journal of the American Ceramic Society* 41 (1958) 1–6.
- [119] W. T. Elam, A. R. Kerstein, J. J. Rehr, Critical properties of the void percolation problem for spheres, *Physical Review Letters* 52 (1984) 1516–1519.
- [120] V. Baroghel-Bouny, Water vapour sorption experiments on hardened cementitious materials: Part i: essential tool for analysis of hygral behaviour and its relation to pore structure, *Cement and Concrete Research* 37 (2007) 414–437.
- [121] A. C. A. Muller, K. L. Scrivener, A. M. Gajewicz, P. J. McDonald, Use of bench-top nmr to measure the density, composition and desorption isotherm of c–s–h in cement paste, *Microporous and Mesoporous Materials* 178 (2013) 99–103.
- [122] R. Feldman, Helium flow characteristics of rewetted specimens of dried hydrated portland cement paste, *Cement and Concrete Research* 3 (1973) 777–790.
- [123] H. Chen, M. Wyrzykowski, K. Scrivener, P. Lura, Prediction of self-desiccation in low water-to-cement ratio pastes based on pore structure evolution, *Cement and Concrete Research* 49 (2013) 38–47.

List of Publications

Peer-reviewed journal publications

1. **M. Zalzale** & P.J. McDonald, Lattice Boltzmann simulations of the permeability and capillary adsorption of cement model microstructures, *Cement and Concrete Research* 42 (2012) 1601–1610
2. **M. Zalzale**, P.J. McDonald & K.L. Scrivener, A 3D lattice Boltzmann effective media study: understanding the role of C-S-H and water saturation on the permeability of cement paste, *Modelling and Simulations in Materials Science and Engineering* 21 (2013) 085016

Conference and non-peer-reviewed publications

1. K.L. Scrivener, A.C.A. Muller, **M. Zalzale**, Q.H. Do & P.J. McDonald, New insights on the mechanisms controlling kinetics and implications for pore structure, Understanding the fundamental properties of concrete, Trondheim, Norway, 25 – 26 April 2013
2. **M. Zalzale**, P.J. McDonald & K.L. Scrivener, A Three-dimensional partial bounce-back method applied to cementitious materials, 22nd International Conference on the Discrete Simulation of Fluid Dynamics (DSFD2013), Yerevan, Armenia, 15 – 19 July 2013
3. **M. Zalzale**, P.J. McDonald & K.L. Scrivener, TRANSCENDING the pore structure of a cement paste: a 3D effective media lattice Boltzmann approach, Proceedings of the 7th International Conference on Concrete under Severe Conditions – Environment and Loading (CONSEC13), Nanjing, China, 23 – 25 September 2013
4. **M. Zalzale**, P.J. McDonald & K.L. Scrivener, TRANSCENDING the pore structure of cement paste with the lattice Boltzmann method, Water transport in cementitious materials, Guildford, United Kingdom, 3 – 6 November 2013
5. **M. Zalzale**, P.J. McDonald & K.L. Scrivener, Numerical modelling of water isotherms of cement paste: bridging the gap between the capillary and C-S-H gel pores, Concrete Modelling 2014 (CONMOD14), Beijing, China, 12 – 14 October 2014 (abstract accepted)

Mohamad Zalzale

Ph.D.

Lebanese
01/05/1987

Contact

Rue Valentin 22
1004 Lausanne
Switzerland

+41 (0)78 615 70 02
m.zalzale@gmail.com

Languages

English: fluent
French: fluent
Arabic: mother tongue

Programming

C, MATLAB, L^AT_EX

Work Experience

- 2014 – **FEI** Trondheim, Norway
Digital Rock Technology
Research & development engineer
- 2011 – 2014 **École Polytechnique Fédérale de Lausanne** Lausanne, Switzerland
Laboratory of Construction Materials
Assistant researcher in materials science
- Research on water dynamics in cement paste
 - Taught construction materials practicals for materials science and civil engineering students
 - Organized multiple outreach activities

Education & Internships

- 2011 – 2014 **Ph.D. in Materials Science** École Polytechnique Fédérale de Lausanne, Switzerland
Water dynamics in cement paste: insights from lattice Boltzmann modelling
- 2013 **Project Management** École Polytechnique Fédérale de Lausanne, Switzerland
Course given by CRPM Lausanne (4 days)
- 2010 **Cisco Certified Network Associate** New Horizons, Lebanon
- 2008 – 2010 **M.Sc. in Computational Physics** University of Montpellier II, France
- 2010 **Research Internship** Air Liquide, France
Development of a lung ventilation model (6 months)
- 2009 **Research Internship** Institut d'Electronique du Sud, France
Simulation of quantum heterostructures (2 months)
- 2005 – 2008 **B.Sc. in Fundamental Physics** University of Montpellier II, France
- 2005 **French Baccalauréat specialized in Mathematics** College Elite, Lebanon

Skills & Abilities

Versatile, project manager, analytical, results-driven, self-starter, team-oriented

Interests

Outdoor activities, travelling, football, watch and automotive industries

